

Recent Trends in Charged Particle Optics and Surface Physics Instrumentation

Proceedings

of the 11th International Seminar,
held in Skalský dvůr near Brno, Czech Republic,
from July 14 to 18, 2008,
organized by
the Institute of Scientific Instruments AS CR, v.v.i.,

Edited by Filip Mika

Published and distributed by the Institute of Scientific Instruments AS CR, v.v.i.,
technical editing by Miroslav Janáček, printed by MJ servis spol. s.r.o.

Copyright © 2008 by the Institute of Scientific Instruments AS CR, v.v.i. and individual contributors. All rights reserved. No part of this publication may be reproduced, stored in a retrieval system or transmitted in any form or by any means, electronic, mechanical, photocopying, recording or otherwise, without the written permission of the publisher, except as stated below. Single photocopies or single articles may be made for private study or research. Illustrations and short extracts from the text of individual contributions may be copied provided that the source is acknowledged, the permission of the authors is obtained and ISI AS CR, v.v.i. is notified.

The publishers have made every effort to reproduce the papers at their optimum contrast and with optimum resolution from materials provided by the authors. The publishers accept no liability for the loss of image quality resulting from supply of poor original material or improperly prepared digital records.

ISBN 978-80-254-0905-3

PREFACE

When writing the preface to the Skalský dvůr proceedings two years ago, I finished with an expression of my doubts about the future of the meeting, about the usefulness of its surviving and about its viability. The final sentence was: Do we want to continue again in two years? Probably a feeling of fatigue of a many times repeated event was responsible for these doubts, in particular by the founders of the tradition. Luckily the changing of generations was just around the corner.

Well, two years are over and the next turn of the meeting is here. The generations have indeed changed – the main organizer of this event was at the last meeting a PhD student, helping then with audio-video-computer facilities. This time he managed to complete all tasks of organizing the meeting alone, just with few consultations he sought at his predecessors, which does not belittle his merit. Just an opposite – to make something for the first time, without personal experience from previous times, and still avoid the beginner's mistakes by asking in proper moments the proper persons, is not only a piece of good work but also a good promise for the future. So by and large I can present you at the moment the best possible message.

However, when again asked to write the preface once more, I would like to use the opportunity and deal briefly with an idea hiding in a corner of my mind – an idea of leaving. It is surely bad if a senior person is not prepared for an end of his/her career, not having his/her successor educated and ready to take over. It is even worse if such a person is not willing to vacate the position in the right time, wanting to extend his/her activity irrespectively of diminishing energy, fading ideas, growing tiredness. Of course, it is recommended to hand on the torch at least a little while before starting to be unable to carry it properly. But this is just the most difficult aspect. In younger years one can quietly leave anyone and anything – the time to return seems unlimited. Later, leavings look more and more irreversible and one does not know what is more desirable: to see the successors doing the things worse or even endangering them and hence reminding the community of the past good work of the predecessor? Or to see them doing the things better, letting in this way the predecessor to fall into oblivion? Only seemingly is the question easy to answer. Why not to continue a bit further, being still capable of this, and to postpone the decision?

Well, the decision for a change has been made and we will experience the Skalský dvůr meeting in a new form that has grown on the basis of previous tradition but that has been modified by fresh stimuli. I am looking forward to this.

Luděk Frank

CONTENTS

ASPECTS OF LATERAL RESOLUTION USING ENERGY FILTERED CORE LEVEL PHOTOELECTRON EMISSION MICROSCOPY N. Barrett, A. Bailly, O. Renault, D. Mariolle, T. Desrues, L. F. Zagonel, M. Escher and M. Senoner	7
MODERN ELECTRON BEAM WELDING TECHNOLOGY J. Bártle	9
SURFACE IMAGING WITH ELECTROSTATIC CATHODE LENSES: SIMULATIONS AND EXPERIMENTS FOR SEVERAL PRACTICAL CONDITIONS M. Bernheim and T. D. Wu	13
DESIGN AND APPLICATIONS OF NOVEL CHARGED PARTICLE ENERGY ANALYSERS D. Cubric, A. De Fanis, N. Kholine and I. Konishi	17
COMPENSATION FOR DRIFT AND VIBRATIONS IN SEM P. Čižmár, A. E. Vladár, and M. Oral	21
CAN LOW VOLTAGE TEM REPLACE 200-400 kV TEMS IN BIOLOGICAL RESEARCH? A. Delong	23
ELECTRON BEAM WELDING: PRINCIPLES AND APPLICATIONS L. Dupák	27
HOW TO PREVENT HYDROCARBON CONTAMINATION IN SEM M. Dvořáková and F. Mika	29
MODULAR MONTE CARLO SIMULATION INCLUDING SECONDARY ELECTRON RAYTRACING D. Gnieser, C.G. Frase, H. Bosse, I. Konvalina and I. Müllerová	31
ADVANCE IN THREE-DIMENSIONAL BOUNDARY ELEMENTS METHOD: SURFACE CHARGE SINGULARITIES IN THE PRESENCE OF DIELECTRICS AND MAGNETIC MATERIALS D. Greenfield	33
PERTURBATION METHODS OF ELECTRIC AND MAGNETIC FIELD MODELLING IN CHARGED PARTICLE OPTICS D. Greenfield and M. Monastyrskiy	37
COULOMB DYNAMICS OF FEMTOSECOND ELECTRON BUNCHES IN TIME-DEPENDING ELECTRIC FIELDS D. Greenfield and M. Monastyrskiy	39

A CONVERSION ELECTRON MÖSSBAUER SPECTROMETER FOR THE ANALYSIS OF MARS-ANALOGUE SAMPLES M. Hahn and G. Klingelhöfer	43
EXPERIMENTAL RESULTS FROM A MAGNETIC BEAM SEPARATOR SPECTROMETER IN THE SEM H. Q. Hoang, M. Osterberg and A. Khursheed	45
WIEN FILTER ELECTRON OPTICAL CHARACTERISTICS DETERMINING USING SHADOW PROJECTION METHOD M. Horáček, I. Vlček, and M. Zobač	47
SCANNING LOW ENERGY ELECTRON MICROSCOPY OF DOPED SILICON AT UNITS OF EV M. Hovorka, Š. Mikmeková, and L. Frank	49
NUMERICAL SIMULATIONS OF THERMIONIC ELECTRON GUNS P. Jánský, B. Lencová and J. Zlámal	51
SETTING UP A PICOSECOND ELECTRON SOURCE BY COMPRESSING PULSES OF A PHOTO EMISSION CATHODE R. Janzen and G. Schönhense	53
A SECOND-ORDER FOCUSING TOROIDAL SPECTROMETER A. Khursheed	57
VARIABLE MAGNETIC SECTOR FIELD ELECTRON SPECTROMETERS FOR PARALLEL ENERGY ACQUISITION A. Khursheed, H. Q. Hoang and S. K. Musuwathi	59
SIGNAL COLLECTION WITH SECONDARY ELECTRON DETECTORS IN SEM I. Konvalina, M. Hovorka, M. Dvořáková and I. Müllerová	61
SOLVING COMPLEX ELECTRON OPTICAL PROBLEWS WITH EOD B. Lencová	65
TIME-OF-FLIGHT- AND SPIN-FILTERING IN LOW-ENERGY ELECTRON MICROSCOPY P. Lushchyk, M. Hahn, G. Schönhense, A. Oelsner, D. Panzer, A. Krasnyuk and J. Kirschner	69
LOW ENERGY ELECTRON MICROSCOPY FOR SEMICONDUCTOR APPLICATIONS M. Maňkoš, V. Spasov, L. Han, S. Kojima, X. Jiang, S. Harb, L. Grella and C. Czarnik	71
HARD X-RAY PHOTOELECTRON SPECTROSCOPY UP TO 15 KEV: RECENT DEVELOPMENTS AND RESULTS WITH A NOVEL INSTRUMENT M.Merkel, M.Escher, N.Weber, J.R.Rubio-Zuazo and G.R.Castro	75

UNIFIED ABERRATION THEORY OF NARROW AND WIDE BEAMS: TENSOR VERSION OF THE TAU-VARIATION APPROACH M. Monastyrskiy	77
DESIGN OF ABERRATION CORRECTORS USING THE DIFFERENTIAL ALGEBRAIC METHOD E. Munro, J. Rouse, H. Liu and L. Wang	81
LOW ENERGY ELECTRON MICROSCOPY IN MATERIALS SCIENCE I. Müllerová, K. Matsuda and L. Frank	85
SIGNAL TRANSPORT IN SCINTILLATION DETECTORS OF SECONDARY ELECTRONS IN SEM L. Novák	87
A CHROMATIC AND SPHERICAL ABERRATION CORRECTED PEEM M. Osterberg and A. Khursheed	89
MODERN APPLICATIONS OF THE ANCIENT WIEN FILTER E. Plies	91
HIGH-ORDER FIELD DERIVATIVES FOR COMPUTATION OF ABERRATIONS T. Radlička	95
A MINIATURIZED ELECTRON OPTICAL COLUMN WITH AN ELECTROSTATIC-PERMANENT MAGNETIC OBJECTIVE LENS C. Rochow, T. Ohnweiler and E. Plies	97
THE ROUTE TOWARDS SUB-Å LOW-VOLTAGE ELECTRON MICROSCOPY H. Rose	99
AN ADVANCED ION GUIDE FOR A DEDICATED SIMS B. Schröppel, A. Brekenfeld and E. Plies	101
SIMULATIONS OF SPACE-CHARGE PHENOMENA IN ION TRAPS AND TOF MASS SPECTROMETERS WITH THE USE OF FMM M. Sudakov	103
RESULTS FROM A NEW HIGH SPATIAL RESOLUTION SAM/SEM ELECTROSTATIC COLUMN A.R. Walker and M. Rignall	105
PEEM WITH TWO COMPLEMENTARY ELECTRON ENERGY FILTERS: TOF AND RETARDING FIELD ANALYSER N.B. Weber, M. Escher, M. Merkel, J. Lin and U. Kleineberg	107
ELECTRON BEAM WELDING IN ISI BRNO: PAST&PRESENT M. Zobač and I. Vlček	109

ASPECTS OF LATERAL RESOLUTION USING ENERGY FILTERED CORE LEVEL PHOTOELECTRON EMISSION MICROSCOPY

N. Barrett¹, A. Bailly², O. Renault², D. Mariolle², T. Desrues², L. F. Zagonel¹, M. Escher³, M. Senoner⁴

¹CEA-Saclay, DSM/IRAMIS/SPCSI, 91191 Gif-sur-Yvette cedex, France.

²CEA-LETI, Minatec, 17 rue des Martyrs, 38054 Grenoble cedex 9, France.

³FOCUS GmbH, Neukirchner Str. 2, D-65510 Hünstetten-Kesselbach, Germany.

⁴Federal Institute for Materials Research and Testing (BAM) Unter den Eichen 44-46, 12203 Berlin, Germany.

nick.barrett@cea.fr

Lateral resolution is a major issue in photoelectron emission microscopy. For a perfect lens system, the ultimate limit is given by the diffraction disk of the electrons which for threshold and shallow core level electrons excited using soft X-ray radiation is ~ 1 nm. More important are the chromatic and spherical aberrations of the extractor field, giving theoretical limits in the 10-20 nm range. Attaining these figures requires near perfect alignment and stability of the electron optics. Sample roughness can significantly degrade the measured width of features and hence the resolution which may be deduced [1]. Finally, the counting statistics, determined by the photon flux, the photoionization cross-section for electron emission and the microscope transmission, limit the best observable lateral resolution.

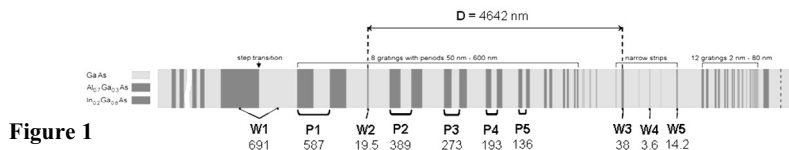
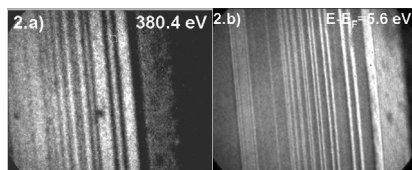


Figure 1

We have carried out X-ray photoelectron emission microscopy using an energy filtered analyser [2] and synchrotron radiation in order to investigate in a practical experiment the role played by these different factors in the measured instrumental resolution. The BAM-L200 sample is an embedded cross-section of epitaxially grown layers of $\text{Al}_{0.7}\text{Ga}_{0.3}\text{As}$ and GaAs on a GaAs substrate [3]. The mounting of the cross-section aligns the surface normal with the optical axis, at 1.8 mm from the first lens. The cross-section is a pattern with strip widths ranging from 0.3 to 700 nm, see Fig. 1.

The ideal profile of the sample surface was constructed from the calibrated distances. The experimental profile determined over the whole field of view and averaged over 200 lines is considered to be the convolution of the ideal flat sample surface concentration profile and a Gaussian whose fwhm represents the instrument resolution.



Core level imaging was done using 400 eV photons at the maximum of the Ga 3d peak (kinetic energy 380.4 eV). To improve the statistics, a set of 29 images of 15 minutes each was necessary. The 150 μm beamline slits gave a

photon band pass of 0.49 eV; the spectromicroscope pass energy was 100 eV. Thus, the overall energy resolution was 0.94 eV. At threshold ΔE was 0.48 eV (beamline slits of 80 μm , pass energy of 50 eV). The contrast aperture was 70 μm in both cases, whilst the extractor voltages were 12 and 15 kV for core and threshold imaging, respectively

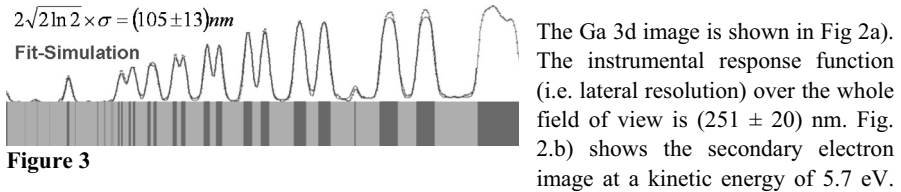


Figure 3

Fig.3 gives the average experimental and simulated intensity profile. A spatial resolution of (105 ± 13) nm is obtained.

The spherical and chromatic aberrations in the electrostatic PEEM column are approximately the sum of those due to the accelerating field and the focussing of the first lens [4]:

$$dr_s \approx \frac{1}{4} \left(l \frac{E_o}{E_a} + C_{s,lens} \left(\frac{E_o}{E_a} \right)^{3/2} \right) \alpha_o^3 \quad dr_c \approx \left(l \frac{E_o}{E_a} + C_{c,lens} \left(\frac{E_o}{E_a} \right)^{3/2} \right) \frac{\Delta E}{E_o} \alpha_o$$

Using the experimental settings this leads to aberrations of 19 and 32 nm for the threshold and core level images. To clean the sample, 1 keV argon ion sputtering was necessary. This induced 5-8 nm steps between the GaAs and GaAlAs layers, as measured by atomic force microscopy. Following Nepijko *et al.* equation for an ideal step [1] leads to a deterioration in the lateral resolution of 40 nm. However, there is still a factor two between the theoretical aberration limited resolution and the experimentally measured values.

Both count-rate and instrumental stability may play important roles in the observed difference between theoretical and observed lateral resolution. The incident flux was 9.5×10^{12} phs $^{-1}$ mm $^{-2}$ (0.1% BW) $^{-1}$, the 3d cross-section at 380 eV is 0.8 Mbarns and the microscope transmission is $\sim 4 \times 10^{-4}$ [5]. A combination of optimal focussing (beam fwhm \sim 2-3 times the field of view), brilliance and photoionisation cross-section could gain of two orders of magnitude. This would also reduce data acquisition time, minimizing the risk of mechanical drift, and allowing more precise electron optical settings to be obtained. Thus, tailored synchrotron sources and high mechanical precision seem to be crucial in improving lateral resolution.

[1] S.A. Nepijko, N.N. Sedov, G. Schönhense, M. Escher, X. Bao, W. Hing *Ann. Phys.* **9** 441-451 (2000).

[2] M. Escher, N. Weber, M. Merkel, C. Ziethen, P. Bernhard, G. Schönhense, S. Schmidt, F. Forster, F. Reinert, B. Krömker, D. Funneman *J. Phys.: Condensed Matter* **17** S1329 - S1338 (2005).

[3] M. Senoner, T. Wirth, W. E. S. Unger W. Osterle, I. Kaiander, R.L. Sellin, D. Bimberg *J. Surf. Anal.* **12** 78-82 (2005).

[4] R.N. Watts, S. Liang, Z.H. Levine, T.B. Lucatorto, F. Polack, M.R. Scheinfein *Rev. Sci. Instrum.* **68** 3464-3476 (1997).

[5] M. Escher private communication

MODERN ELECTRON BEAM WELDING TECHNOLOGY

J. Bärtle

pro beam AG & Co. KGaA, Behringstr. 6, 82152 Planegg, Germany

jan.baertle@pro-beam.de

Introduction

Since the commercial use of the electron beam (e-beam) for material treatment purposes, especially welding tasks have become a well known field of application [1] allowing joining a large variety of materials. Due to the precisely defined lateral energy input into the work piece, very narrow and - if required - very deep weld seams are obtained. The application of e-beam welding imposes a certain overhead due to the required vacuum^{*}. Nevertheless, e-beam welding is a cost effective welding method and is present in many manufacturing processes, enabling higher quality at lower prices for a broad range of materials.

To further improve the present abilities and intelligence of nowadays state-of-the-art e-beam welding machines, modern development pursues the following goals: a) further reduction of non-productive times, b) application of image processing to increase the machine intelligence and c) application of multi-beam techniques for high-speed beam manipulation and generation of high power density beams to additionally enhance the productivity.

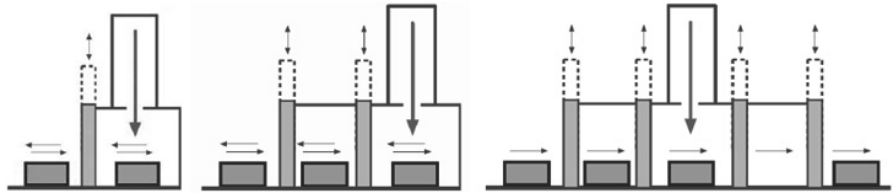


Fig.1: Different strategies to reduce non-productive times. The single chamber-machine is shown on the left. During pallet change, the e-beam has to be switched off until pump-down is completed. The middle and right figures show different types of load-lock shuttle and transfer machines; their advantages are that the productive e-beam time does not depend on the pump-down time during pallet change. Depending on the manufacturing demands, the appropriate machine type has to be selected individually.

Improvement of the productivity

The reduction of non-productive times is mainly a design task for the machine construction. Nowadays e-beam welding machines can be equipped with load-lock shuttle systems and therefore substantially increase the productivity (Fig. 1). Especially in optimised cycle machines for e.g. the automotive industry, pump-down times in the range of seconds are achieved. Hence, a dedicated machine set-up is available for nearly all applications, making the required vacuum no longer an obstacle for economic production.

^{*} Non-vacuum e-beam welding is possible, but is only relevant in some special applications like high-speed welding of tailored blanks.

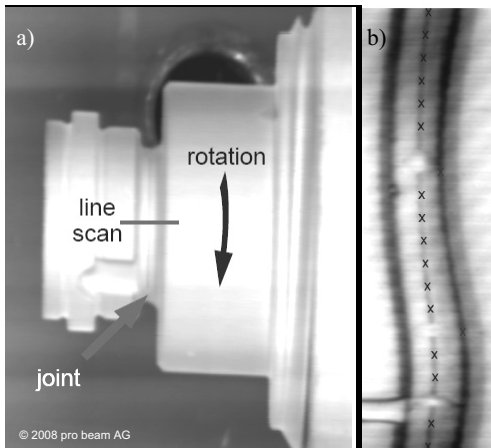


Fig.2: Modern image acquisition preceding the welding. In case of a mechanical offset of the work piece, the side-by-side run-out may be detected by acquiring the image b) as an ongoing line-scan by rotating the work piece as indicated in a). The processed image then supplies the beam control with the necessary information required to guide the beam exactly along the joint seam. The calculated seam track is indicated in b) with "x".

Application of image processing techniques

The part handling capabilities (pallet and part movement) are prerequisites for autonomous welding. Exact positioning by means of a high precision work piece table is cost-intensive and its movement is slow (especially when handling heavy parts). On the other hand, the beam deflection is very fast and accurate. As a consequence, the intelligence of modern e-beam welding machines is employed to circumvent mechanical inaccuracies. In the first step the pallet is placed under the e-beam. Then an electron optical image is acquired operating the machine like a scanning electron microscope. The image acquired from backscattered electrons is then processed; the result yields the exact position and orientation of the part with respect to the coordinate system of the beam. This information is transferred to the beam control, which compensates the mechanical offset by means of an adequate beam shift. The next step is to automatically check the position of the weld seam. Due to mechanical or magnetic disturbances, the real weld seam often differs from the ideal one. With the same image processing technology, the parameters for the beam guidance during welding are calculated (see Fig. 2 as an example of a radial weld) and supplied to the beam control*.

* Of course, these preparation steps preceding the welding have to be performed as quick as possible as they are non-productive times, they are described as online seam-tracking.



Fig.3: Multi-beam welding during the assembly of a particle filter. By means of high-speed e-beam deflection, the e-beam is shared between the different welding locations, 60 in number, as shown left. This provides a reduction of material distortion due to symmetric heat input and strongly reduced welding times by parallel processing. However, the power density of the beam must be sufficiently high to provide enough energy in every single weld pool. Furthermore, the beam must hit precisely the individual welding pools.

Multi-beam technology

Fig. 3 shows a typical multi-beam process. Since the beam deflection is controlled by a digital waveform generator, a nearly unlimited lateral manipulation of the e-beam position is possible. Nowadays, the waveform generator drives a high-speed amplifier-coil-arrangement with tendency on low-inductance coils allowing arbitrary beam movement up to some ten kHz. This degree of freedom is typically used to enhance the productivity by welding in parallel but can be also used for online seam tracking during welding in dedicated applications [2]. These features require slew rates of more than $1 \text{ A} / \mu\text{s}$ and amplifiers with a peak performance in the range of several hundreds of W. The benefit of the simultaneous welding is, however, only available if the focussed e-beam provides enough power, e.g. in a five-beam arrangement, the beam needs to have 5 times more current. This is a challenge especially when small weld seams are required. Neither the cross-over of the beam in the electron gun nor the divergence of the beam should substantially exceed the beam values of the single-beam process. Fortunately, the gun system of modern e-beam welding machines provides power densities of up to $1 \text{ MW} / \text{cm}^2$, and so the multi beam concept is usually not limited by the gun properties.

Outlook

Since software is getting more and more dominant in extending the functionality (intelligence) of e-beam welding machines, the implementation of novel techniques (pattern recognition for more autonomous and reliable production, automatic error detection and quality control purposes) will play an important role in the next years, besides of further tuning of electron gun, deflectors and lenses. In the near future, electron beam welding machines targeting the MST area (micro system technology) will be commercially available, requiring a new column and machine concept [3, 4] as well as a new process management.

References

- [1] Schiller S., Heisig U., Panzer S.: *Elektronenstrahltechnologie*, Verlag Technik, Berlin, 1995.
- [2] von Dobeneck D.: *Economizing Electron Beam Welding – Recent Developments and Future Trends*. Proceedings of the IIW International Conference, Prague, 2005.

- [3] Bärtle J., Löwer, T., von Dobeneck, D.: *Electron beam welding beyond the ordinary scale*. Proceedings of EBT2006, Varna, 2006.
- [4] Böhm S., Tanasie G., Reinhart G., Reiter A., Franzkowiak M., Löwer T., Bärtle J., Fricke S., Müller G., Friedberger A.: *Elektronenstrahlbasierte Fertigung von Mikroprodukten*, wt-online 11/12-2007, S. 868-872.
[http://www.technikwissen.de/wt/article.php?data\[article_id\]=38786](http://www.technikwissen.de/wt/article.php?data[article_id]=38786).

SURFACE IMAGING WITH ELECTROSTATIC CATHODE LENSES: SIMULATIONS AND EXPERIMENTS FOR SEVERAL PRACTICAL CONDITIONS

Marc Bernheim* and Ting-Di Wu#

* Physique des Solides Bât. 510, CNRS, Univ. Paris Sud, F 91405 Orsay, France.

Institut Curie Recherche, Bât. 112, Univ. Paris Sud, F 91405 Orsay, France.

bernheim@lps.u-psud.fr

ting-di.wu@curie.u-psud.fr

General

Following various primary excitations, secondary electrons or ions may leave solid surfaces directly providing means for local and analytical characterizations with really high spatial resolutions and sensitivities¹. These various setups include a charged particle collection completed with specific spectrometers used for particle identification (energy and mass dispersion eventually).

Direct microscopy or probe scanning

Most usual conditions gather large excitation beams directed onto the surface. The surface images are recorded in the output of the spectrometer directly with spatial resolution fixed by the collection optics in association to the mass spectrometer and projection optics. In other circumstances, primary probes are focussed and scanned over the sample surface; the images are reconstructed sequentially in the spectrometer output with a resolution mainly controlled by the primary spot size: the collection of secondary particle escape many optical constraints. Such conditions really improve both the accessible sensitivity and the spatial resolution during SIMS analyses notably.

This contribution focuses on the properties of immersion objective lenses in various experimental contexts. After the initial acceleration, the charged particles are focussed either by magnetic or by electrostatic optical systems. Here, the last configuration escapes additional rotation in azimuth which may perturb acquisition involving beams dispersed in energy.

Depending on the polarity $U < 0$ or $U > 0$ applied to the objective focussing electrode with respect to the surface bias, the beam experiences either a transient deceleration or acceleration followed by variation in focussing properties.

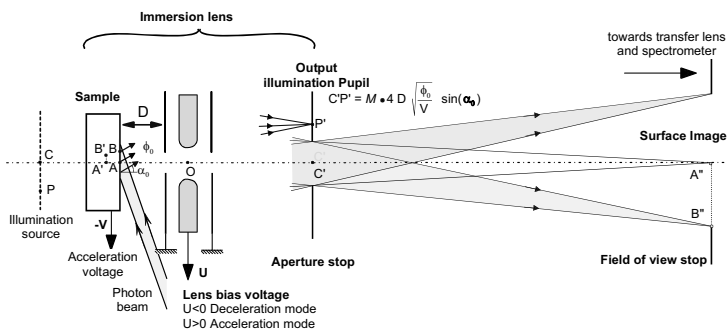


Fig. 1 Electrostatic Immersion objective lens.

¹ Despite of much higher spatial resolutions, investigations by TEM (transmission electron microscopy) imply heavy sample preparation procedures including a contrast averaged over all the sample thickness.

Both previous configurations influence the achievable spatial resolution which is mainly controlled by aperture aberrations of the objective. Obviously an aperture stop is really compulsory, independently of any further correction system. Moreover, it can easily shown that the Gauss surface image is shifted significantly along the system axis as varies the initial energy of ejected particles. Therefore, chromatic aberration should be considered in relation with the beam energy band pass selected by the spectrometer:

- LEEM-PEEM experiments imply electrons of energies below ten electron-volt [1].
- Spectro-microscopy characterisation by ESCA needs selection of a narrow energy window centred at a variable energy up to 150 eV [2].

Practical disturbance in the acceleration space

Local changes in the sample work function or mechanical defects of the sample setting cause inclination effects in the initial acceleration space followed by low energy cut-off effects in the transmitted beam intensity. As a thick lens system, the objective lens may apply a rotation around the nodal points N and N'. The shorter are the acceleration space and the applied voltage the higher are the rotation angle. Moderate electrostatic fields and voltage better convene in spite of a loss in collection efficiency.

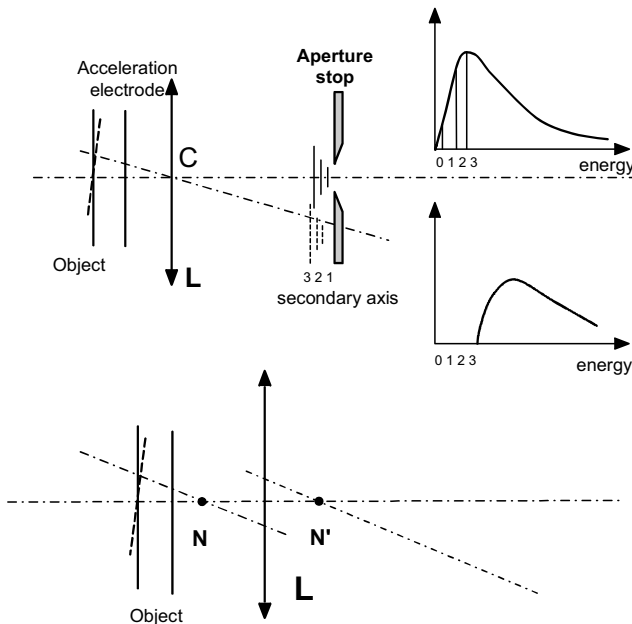


Fig. 2 Inclination effects

Several beams transmission in a coaxial mode

- Electron beam applied in mirror like conditions to control the surface potential of insulating samples during SIMS analyses with negative ions.

- Electron stimulated desorption experiments imply an electron beam of variable final energy and constant density to record a resonant desorption of negative ions build from elements chemisorbed on solid surfaces [3].
- Focussing of a positive primary ion probe associated with a high efficiency collection of negative secondary ions coupled to a high mass resolution and a multi detection system in the NanoSims configuration [4].

Surface preparation by a low energy Cs⁺ probe in for Nanosims studies

In usual conditions the primary Cs⁺ beam impinge the surface with a very high energy of 16 keV. To increase the surface cesium content and to consequently benefit of very high yields in negative secondary ions we suggest to apply a transient surface implantation with cesium ions of very low energy. The set-up control was guided by simulations performed within Simion 8. Indeed the bias of electrodes E0P and E0S should be adjusted concurrently with the sample voltage to keep a beam of energy as low as 20 eV over a diameter about 10 μm .

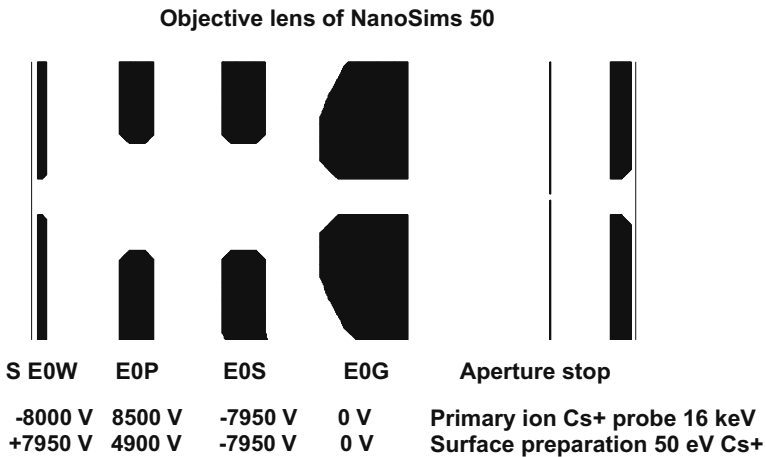


Fig 3 NanoSims objective lens reported by Simion 8 including conditions for focussing a 50 eV Cesium beam onto the sample surface S.

After recovering the usual electrode bias voltages, the NanoSims characterizations can be performed with an increased sensitivity directly on samples with caesium enriched surface [5]. Such conditions suit for biological investigations especially or to study semiconductor surfaces build by shallow implantations since the high sensitivity in obtain from the beginning of the sample erosion.

Additional remarks about electron emission microscopy

Several additional aspects related to photoelectron microscopy will be discussed in this contribution. For example, the accessible spatial resolution will be compared in various experimental configurations. In any case the used aperture stop stays much too large to cause diffraction effects limiting the image resolution at variance with published data [6-7].

Let us add that the acquisition of energy filtered images either in ESCA or in PEEM and LEEM requires an electrostatic prism system. Most set-ups use hemispherical electrostatic deflectors in which the chromatic focus is reported in infinity. A 90° spherical deflector is much more convenient since an achromatic image is reported in the intersection of entry and out put axes. Therefore, even with a wide energy band pass, the surface image keeps a high quality in spite of the wide energy band pass. In the SIMS context such elements serve for filtering images in IMS (n)F CAMECA spectrometers.

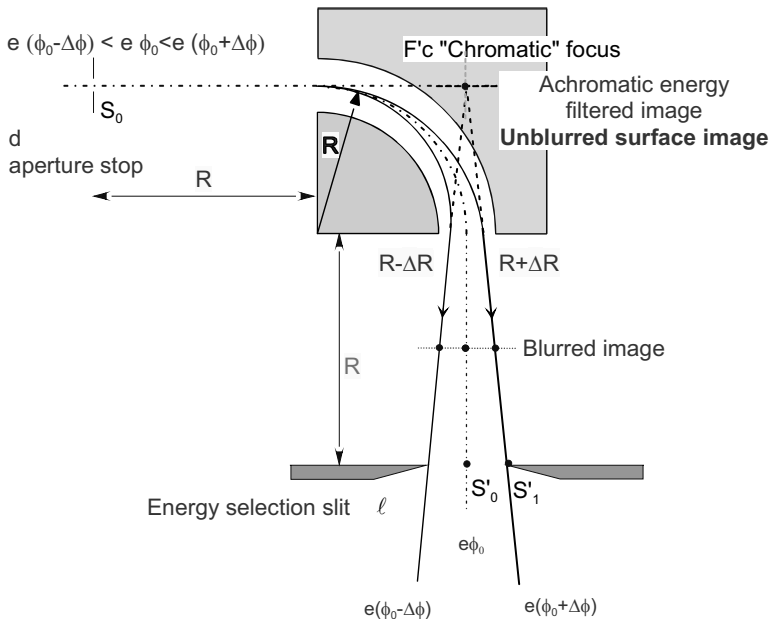


Fig 4 Electrostatic prism working as an image energy filter.

References

- [1] M. Bernheim, Ultramicroscopy ,106, (2006), 398-412
- [2] M. Bernheim, Eur. Phys. J. Appl. Phys., **36**, 193-24 (2006)
- [3] M Bernheim, Surf. Science, **494** (2001), 145-157 and 566-568 (2004), 1222-1228
- [4] G Slodzian *et al.*, Bio. Cell, (1992), **74**, 43-50
- [5] M. Bernheim and Ting Di Wu, Eur.Phys. J. Appl. Phys. DOI: 10.1051/epjap:2008062.
- [6] G. F. Rempfer and O. H. Griffith Ultramicroscopy 27 (1989), 273-300.
- [7] Th. Schmidt *et al.* Surface Review and Letters 9, 1 (2002) 223-232

DESIGN AND APPLICATIONS OF NOVEL CHARGED PARTICLE ENERGY ANALYSERS

D. Cubric^{a,*}, A. De Fanis^a, N. Kholine^b and I. Konishi^a

^a Shimadzu Research Laboratory (Europe), Trafford Wharf Road, Manchester M17 1GP, UK

^b Institute for Analytical Instrumentation, Russian Academy of Sciences, St Petersburg, Russia

* dane.cubric@srlab.co.uk

Introduction

This paper describes two novel families of charged particle energy analysers. It was tempting to focus this presentation only on one specific analyser type and results. However in anticipation of the welcome feedback from the conference participants, both will be presented.

The two analyser types whose properties we present are parallel electron analyser types and the spheroid electron energy analyser.

Parallel electron energy analysers

Several prototype analysers were designed and built in SRL based on hyperbolic electric field focusing properties and others studied by means of simulation. A similar analyser type was first mentioned in [1], and at that time constructed as compact wide aperture energy per charge analyser for ion detection. The usefulness of the hyperbolic field energy dispersion properties was then rediscovered by [2] and demonstrated in the context of an electron energy analyser for Auger electron spectroscopy for surface elemental analysis. This was soon followed by SRL who consequently developed several prototypes and tested the analysers in fast Auger electron spectroscopy and demonstrated measurements of fast dynamic charging phenomena as well as benefits of using two analysers simultaneously for elemental and topographical examination of the specimens [3].

The particular advantage of the hyperbolic electric field type analyser is in the quadratic dependency of the electron landing energy on the landing distance and focusing of a very wide energy range onto a straight focusing plane or line. This in turn enables a multi-channel position-sensitive detector to be employed in the focusing plane detecting a very wide energy window all at once. Typically we employed 50 mm long detectors with 1024 or 2048 channels and detected a range of energies from maximum (E_{max}) to minimum (E_{min}) as $E_{max}/E_{min}=24$. Though the electric field in those analysers provides practically only first order focusing, it turned out that the combination of the electric field properties and the detector capability provides about 0.5% relative energy resolution, well applicable for surface Auger electron analysis. Moreover, the full spectrum acquisition is very fast, within a second or so, potentially enabling this type of analysers to be used in the high throughput semiconductor inspection industry where nanometer scale features have to be analysed for elemental composition. Figure 1 shows a photograph of one of the parallel analysers built in SRL. Figure 2 shows a schematic configuration when two analysers are coupled to provide both elemental and topographical information. Figure 3 shows an example GUI from the

acquisition system that runs two analysers simultaneously containing the SEM image of the specimen as well as intensity profiles received by the two analysers. Figure 4 shows similar field of view but with Auger spectra from different positions at the specimen displayed.

Other types of parallel analysers were also studied in SRL including cylindrically symmetric analyser with linearly varying potential on the outer cylinder [4] as well as a unique magnetic type parallel analyser whose landing energy dependency of the landing distance is cubic enabling an even larger energy range to be detected simultaneously.

However, not everything has been easy sailing with the parallel analyser instruments. A particular difficulty is channel gain variations of any practical multichannel detector that in turn could drastically decrease useful dynamic range of the analyser. This in turn could make a weak spectral features, but however important for elemental identification, to be lost among channel gain variation features, particularly for short acquisition time that is in turn required if the analysers are to be competitive in the fast acquisition time type of instruments. Due to nonlinear dispersion across the detector the spectrum could not be scanned over the detector as standard technique for gain variation requires. We have however made significant progress on this issue and some results will be reported at the conference.

Spheroid energy analysers (SEA)

The SEA analyser family generalizes the concentric hemispherical energy analysers (CHA) and cylindrical mirror analysers (CMA). It has been developed recently through a SRL and Microsan collaboration [5]. Figure 5 shows a cross-section of a possible embodiment of this type of analyser and the photograph at figure 6 shows the first prototype installed in SRL.

Referring to figure 5 and the two sets of radii of the outer (R_1 and R_{01}) and inner (R_2 and R_{02}) spheroid surfaces we describe different analyser geometries via three dimensionless parameters: $K_1=R_1/R_{12}$, $K_2=R_2/R_{12}$ and $K_3=R_{02}/R_{12}$, where $R_{12}=R_{01}-R_{02}$. Using this geometry description the CHA has electrode surfaces for which $K_1=1+K_2$ and $K_2=K_3$, while the CMA, on the other hand, has electrode surfaces for which $K_1=K_2=\infty$. However there is an infinite combination of K_1 , K_2 and K_3 parameters that could be varied independently that in turn result in spheroid geometries with very favorable electron optical properties. The preferred embodiments of the SEA are within $1 < K_1 \leq 10$, $1 < K_2 \leq \infty$ and $0.1 \leq K_3 < 3$ and a particular prototype instrument, whose schematic is shown in figure 5, has been constructed with $K_1=2.756$, $K_2=4.889$ and $K_3=0.944$. The SEA provides transmission of 21% of the half hemisphere and relative energy resolution of 0.05%, both at the same time. This compares very favorably to commercial CMA with typical resolution of 0.5% and somewhat smaller transmission. The fringe field termination in SEA is naturally achieved by proximity of the edges of the inner and outer spheroid, therefore requiring no field correcting electrodes. Linear dispersion of this particular instrument is $LD=(\Delta X * E) * \Delta E = 200\text{mm}$, where E is medium electron energy at landing position, ΔE is energy spread and ΔX is the corresponding axial spread. It is feasible that a position sensitive detector is used at the exit of the analyser further increasing detection efficiency by a factor of 80 and still keeping energy resolution of 0.05%.

Combined with a high resolution column this instrument could make an efficient electron microscope for chemical analysis. The high resolution and transmission opens further unexplored possibilities where not only Auger but also XPS could be done providing that a compatible small spot X-ray source was to be constructed.

Figure 7 shows the ray trace SIMION simulation at the exit focusing plane where three energy bunches are traced with 0.05% energy difference and with initial angular spread from 44° to 60° with respect to the axis of the analyser. The three trajectory bunches appear completely separated indicating theoretical resolution of 0.05% at the base of the spectral lines. Figure 8 shows first experimental results where the FWHM of the 5keV elastic peak was measured resulting in energy resolution of 0.048%. Two additional peaks shown on the figure are from elastic signal at 4980 and 5020 eV that are used for energy scale calibration in this instance.

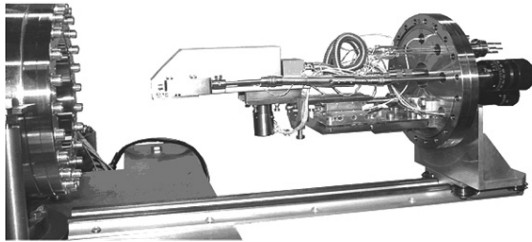


Figure 1. Photograph of the parallel analyser (PA).

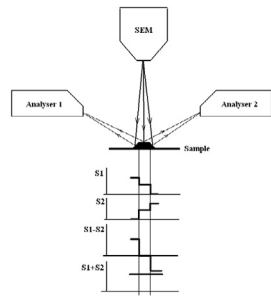


Figure 2. Schematic of the 2PA system for elemental and topography analysis.

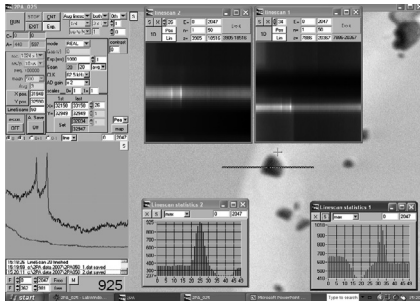


Figure 3. GUI of the data acquisition system with SEM and intensity profiles from the line scan data from the two analysers.

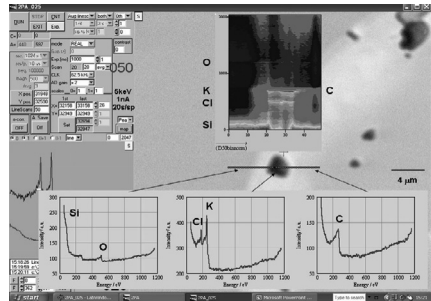


Figure 4. Auger spectra from the same line scan data as on figure 3.

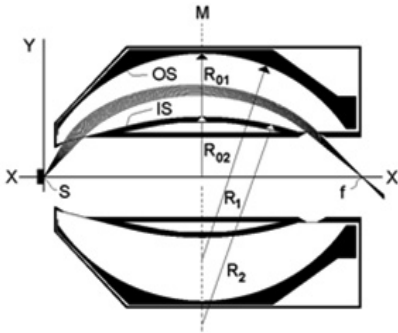


Figure 5. Schematic of the spheroid energy analyser (SEA).

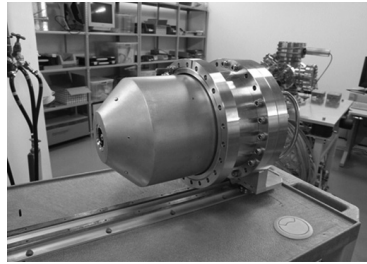


Figure 6. Photograph of the first SEA.

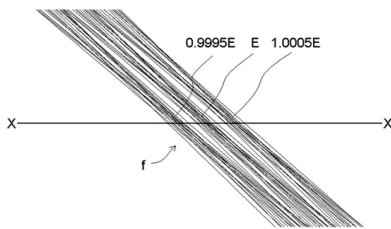


Figure 7. Ray trace simulation of three bunches of electron trajectories at the exit focusing plane of the analyser for entrance angles of 44 to 60 degrees and relative energy difference between adjacent bunches of 0.05%.

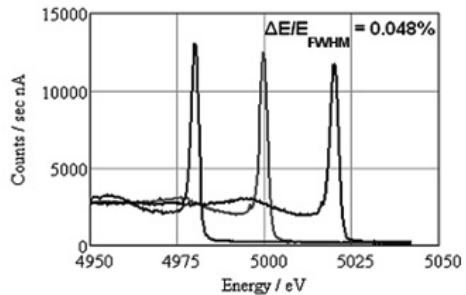


Figure 8. Three elastic electron spectra measured by SEA showing high energy resolution.

References

- [1] C.C. Curtis and K.C. Hsieh, *Rev. Sci. Instrum.* **59** (1988) 2424
- [2] M. Jacka, M. Kirk, M. El Gomati and M. Prutton, *Rev. Sci. Instr.*, **70** (1999)2282.
- [3] D. Cubric, A. De Fanis and F. Barber, "*Proceedings 2. Instrumentation*", ICM16, Sapporo, 2006, p.1153.
- [4] F.H. Read, D. Cubric, S. Kumashiro and A. Walker, *Nucl. Instr. And Meth. A* **519** (2004) 338
- [5] N. Kholine, D. Cubric and I. Konishi, UK patent application No: 0720901.8, October 24th 2007.

COMPENSATION FOR DRIFT AND VIBRATIONS IN SEM

Petr Cizmar, András E. Vladár, and Martin Oral

National Institute of Standards and Technology, 100 Bureau Dr, Gaithersburg, MD 20899, USA*

Scanning electron microscopes (SEMs) acquire images by assigning signal intensity values to pixels that are arranged into a digital image. If the images are taken with long acquisition times, then the image may be blurred and/or distorted. Essentially, all SEM images are taken on moving targets; therefore, unless corrective methods are used, all pixels are affected by information that belongs to other pixels. Unfortunately, in most high-magnification SEMs, motions have wide frequency spectra. The high-frequency motions cause blur or flagging while the low-frequency drifts lead to distortions.

Processed (amplified, digitized, etc.) signal from the detector usually contains considerable amount of noise. To collect images with satisfactory signal-to-noise ratios, two types of image acquisition are used. One is the traditional slow-scan image acquisition with long pixel dwell times. The frame time is typically between 40 s and 300 s. The other method uses a series of images collected at or close to the TV-rate (25 or 30 full frames per second) and the final image is obtained by averaging. The first method often results in severe distortions because the slow drift of the sample relative to the beam shifts the landing position of the beam away from its intended location. Images obtained with this method are not suitable for dimensional measurements or for other applications requiring true-shape imaging at high magnifications. Averaging is much better in preserving the true feature shapes but unfortunately, since the drifts are still in effect, simple averaging may result in a blurry image.

There are two methods to correct the effects of the motions in the SEM. One approach is to directly measure the position of the sample with respect to the electron-optical column. NIST is developing a reference SEM instrument, which is equipped with two laser interferometers. Both of them have differential laser heads enabling relative measurements of the sample-stage motion with respect to the column. The resolution of these interferometers is 38 pm. For every acquired signal contribution, this instrument provides additional information revealing the true position of each landing position of the beam. Such contributions can be in turn assigned to the right pixels which in ideal case eliminates the image derogations caused by motions in the SEM. Unfortunately, it is not possible to attach the reference mirrors of the interferometer directly to the electron beam. Motions within the column, the column bowing, and other error contributors are thus not covered in the measurement. However, this method can significantly improve the quality of the SEM images, especially for metrology applications.

The other approach to reduce the effects of the motions in the SEM is a new imaging method with application of adaptive averaging of super-fast SEM images (images taken at the highest sampling rates). The algorithm finds shift vectors for all individual images and shifts them to their correct location. The shift vectors are calculated with sub-pixel resolution using cross-correlation of the images computed using the Fourier Transform. The method is implemented in C programming language as a fast code that allows for real-time processing of the images.

Figure 1 shows a single image collected in 11 μ s, the results of traditional and adaptive image averaging. The image obtained with the new method is clearly sharper. Details that can hardly be

seen with the traditional method come out. Careful observation of the image acquired by adaptive averaging reveals that the image in narrow sections close to the upper and right sides is noisier than in the center. This happens because due to drift, fewer contributions were collected there. These inconsistencies can be simply eliminated by cropping. An additional benefit of the adaptive averaging method is that it provides the shift vectors that can be used to track drift and vibration of the SEM.

The individual images collected at fast rates are very noisy but as long as they can be shifted to their correct location, this does not constitute a problem. The optimal image collection minimizes effects of drift and higher-speed stage and beam motions. The super-fast image collection and processing presented here can be integrated into future SEM software. This method is especially advantageous for the highest-resolution instruments, where even close to 1 nm motions are unacceptable.

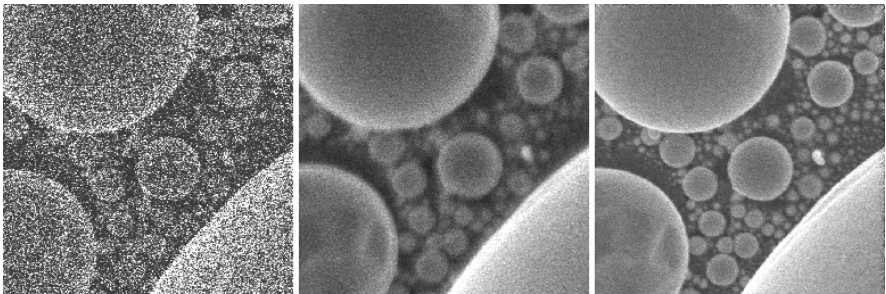


Figure 1. Single image acquired in 11 μs frame time (50 ns pixel dwell time) (left), traditionally averaged 70 images (middle), and the same 70 images averaged with the new, adaptive method (right). The field-of-views are 4617 nm.

*Contribution of the National Institute of Standards and Technology; not subject to copyright. Commercial equipment and materials are identified in order to adequately specify certain procedures. In no case does such identification imply recommendation or endorsement by the National Institute of Standards and Technology, nor does it imply that the materials or equipment identified are necessarily the best available for the purpose.

CAN LOW VOLTAGE TEM REPLACE 200-400 kV TEMS IN BIOLOGICAL RESEARCH?

A. Delong

Delong Instruments a. s., CZ-612 00 Brno, Czech Republic

E-mail: Armin.Delong@dicomps.com

A. Present situation

Transmission electron microscopes presently used to study biological objects work with acceleration voltage 200-400 kV. Such microscopes, especially the latest version called achroplanát, which is TEM with spherical and chromatic aberration correction of the objective lens and assumed resolution better than 0,05 nm (0,5 Å), which promises new findings concerning composition of solids, especially crystals which resist being bombarded with electrons of such high energy.

Such microscope doesn't bring any new possibilities for biological application. But even the present ones are few satisfactory.

Biological objects with specific mass cca 1g/cm^3 , composed of elements with low atomic number, scatter fast electrons very little only. As a consequence the reachable amplitude contrast is insufficient for occurrence of a usable image. The present trend in biological research moves towards studying objects (particles, thin sections), which are very thin (in terms of nanometers to dozens of nanometers). The only possibility to visualize such structure is using phase contrast, which occurs when the image is defocused by a comparably large value which, however, causes loss of resolution. Methods of increasing the contrast by means of selectively placed atoms of heavy metals are unacceptable due to occurrence of artifacts. These methods also constrain the object from staying in its most natural condition. At present time, putting an object into a layer of amorphous ice with thickness close to thickness of the object put into it is considered such a method. However, this method doesn't lead to a significant increase of contrast either. In order to improve the ratio between signal and noise, averaging of large amount of images (thousands to million) is required. Another problem is caused by radiation damage which occurs because of bombarding the electrons with energy, that suffices to take the atoms away from the object. TEM with accelerating potential 200-400 kV is a large, difficult to place machine. It is not affordable for many workplaces.

Elastic scattering significantly increases when energy of the imaging beam is decreased. Objects and structures usually not exceeding thickness 20-30 nm (both particles and thin sections) are presently in the center of interest. This leads to attempts to reach the atomic resolution even in case of biological objects. It was determined that energy 5 keV suffices to make the electrons pass through the aforementioned objects with a large share of electrons with elastic scattering. It enables to reach 5% contrast in structures with difference of thickness 0,5 nm or difference of mass $0,05\text{g/cm}^3$. Experiments confirm that it is possible to completely eliminate contrasting using heavy metals during preparation. We also prepare experiments with imaging objects in a thin layer of ice with thickness cca 10-20 nm, which is

reached by using new detergents. The earlier constatation that when energy of electrons is 5 keV, the radiation damage is exceptionally strong, was made during study of too thick objects. In case of thickness under 30 nm, a significant change in character of imaging occurs: edge sharpness increases and halo, which decreases contrast, disappears. It probably means that the impact of chromatic aberration is decreased due to smaller amount of non-elastically scattered electrons. To some extent, the decrease of non-elastically scattered electrons may be linked to a mean free path [1] and thickness of the object when energy is 5 keV. The mean free path was set to a value of 15 nm. Several examples show possibilities of present time low voltage TEM.

Its handicap is obviously not the sufficient contrast but the resolution capability, which is limited by reachable spherical and chromatic aberration of the objective lens. Therefore an attempt was made to implement a low voltage TEM with correction of spherical and chromatic aberration of the objective lens. Its description is contained within next part of the paper.

The low voltage TEM has several advantages compared to the presently used high voltage TEMs. Its development, especially the correctors, may take some time. It may be a possible candidate for a biological TEM with atomic resolution. Some suppositions will be further elaborated.

B. Technical implementation of low voltage TEM

The desktop implementation of the microscope is not unlike the standard light microscope and the possible modes of functioning are in sharp contrast with present day TEMs, which are large and even require constructional modifications of the workplace.

A current low voltage microscope is made of several functional blocks:

- electron optical system
- pre-vacuum system
- computer with a monitor
- electronic power supplies

Electron optical system of low voltage TEM

Tube of the microscope is composed of independent blocks:

- electron gun
- objective lens and a condenser with permanent magnets, coordinate manipulator with x, y, z and rotation movement using piezo elements
- chromatic and spherical aberration corrector
- five quadrupole projective
- converter of electron image to light image

Electron gun

A source of electrons is cold field emission cathode of new construction.

A pin of tungsten wire thick 0,1 nm is attached to another such wire on whose end an apex is etched. The apex is covered by a thin layer of epoxid and after polymerization the cathode is ready to work. The main advantage is ability to emit under comparably high pressure (10^{-7} mbar). The cathode as a whole appears like a so called "sharp cathode" which works under pressure 10^{-10} mbar only.

Objective and condenser lens with permanent magnets

It is technically simple and has one disadvantage only: impossibility to change focal length for focusing. But it shows that in case of a corrected objective lens, a change of stimulation is not suitable and focusing is realized via changing the object position. For this way of focusing, the piezo movement with a step 1 nm and speed several hundred steps per second in conjunction with CCD camera is exceptionally advantageous. Possible impact of thermal dependence of magnetic field during exposition is not very likely. The whole thermal input to the tubus is minimal, its volume is sufficient so that temperature of magnets during exposition can't change more than acceptable.

Corrector of spherical and chromatic aberration

A solution proposed by Rose [2, 3] almost 20 years ago has several obvious advantages:

- there is a minimal number of multipoles (3 in total)
- both correctors are rotationally symmetrical

The corrector that we implemented is made of three dodecapoles. One dodecapole is electrostatic magnetic, it functions as a non-homogeneous Wien filter for chromatic aberration correction with a possibility to use it alternatively as image filter and spectrometer of energy losses of electrons with exceptionally high sensitivity. Hexapole corrector is made of two electrostatic dodecapoles and four electrostatic lenses. The corrector as a whole measures 45 mm. Let us not expect immediate success. The solution is, however, promising to such an extent, that a continuation is deserved even after initial failure.

Quadrupole projection lens

Projective composed of five octupoles functioning as quadrupoles is very suitable for achieving various goals.

Converter electron image to light image

A thin YAG plate and a standard light microscope objective were replaced by a system of two lenses: a round YAG lens and a commercial achromatic dublet. The lens thus has focalization in the infinite. In conjunction with a CCD camera, it presents a projective with 1000x. Its advantage is four times higher luminosity compared to the system of YAG plate and a light objective and several other advantages (contrast, resolution, antiimplosion etc.)

The short tubus (cca 270 mm) is exceptionally robust and resistant to vibrations and stray

magnetic fields. Thanks to its low mass it is possible to find a place with minimal distracting influences and thus create conditions for gradual improvements towards a machine of high parameters, towards atomic resolution of biological objects.

Low voltage transmission electron microscope is designed as a device to study objects with low mass (cca 1g/cm^3) in biology and polymeric chemistry. Its multifunctional properties could extend the present suite of electron microscopes. The aforementioned low voltage TEM will enable using the following modes of operation:

1. Low voltage TEM (with correction of spherical and chromatic aberration)
2. Low voltage STEM
3. SEM with back scattered electrons
4. SAED selective electron diffraction
5. EELS spectroscopy of electron energy losses, imaging using electrons with selected energy
6. Stereomicroscopy and tomography
7. Cryomicroscopy

References

- [1] L. F. Drummy, J. Yang and D. C. Martin, *Ultramicroscopy* 99 (2004), p. 247
[2, 3] H. Rose, *Optik* 77 (1987), p. 26, *Optik* 84 (1990), p. 91

ELECTRON BEAM WELDING: PRINCIPLES AND APPLICATIONS

L. Dupák

Institute of Scientific Instruments AS CR, Kralovopolská 147, 61264 Brno, Czech Republic
E-mail: ldupak@isibrno.cz

In vacuum technology and especially in UHV we often encounter the necessity of joining parts of various materials in combination with the demand for perfect vacuum tightness, cleanness of joints and minimum deformations. Electron beam welding belongs to the best technologies capable of fulfilling such requirements.

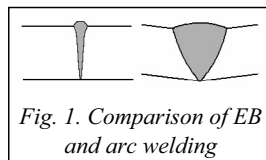


Fig. 1. Comparison of EB and arc welding

The principle of electron beam welding is based on the transfer of the kinetic energy of the incident accelerated electrons to the welded material in the form of heat. Temperature in the spot rises with beam power density. At power densities as high as $10^4 - 10^6 \text{ W/mm}^2$, the melted material at the center of the focal point evaporates. This produces a vapor capillary surrounded by melted material, which allows the beam to penetrate deeper and to melt more material. The speed of the penetration can be much higher than the speed of heat transfer by conduction into the surrounding material. This results in narrow melted area and typical knife-

like profile of the weld (Fig. 1). Such specialties of the heating by electron beam allow welding of metal materials regardless of their melting point.

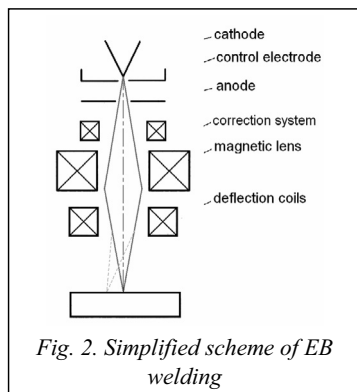


Fig. 2. Simplified scheme of EB welding

The design of the electron beam welder (Fig. 2) is similar to a scanning electron microscope. For welding, the thermionic emission cathodes are used as a source of free electrons. For low powers (several kW), cathodes are directly heated tungsten or tantalum wires or strips. For higher powers, cathodes are in the form of button or rod heated indirectly from auxiliary electron source. The typical maximum power of electron beam welders varies from 0.5 kW to 100 kW with acceleration voltage from 30 kV to 200 kV.

The ability to focus the electron beam, therefore concentrate power to a very small spot, minimizes the heat-affected zone (HAZ) and, therefore, minimizes the thermal distortion of the work-piece (Fig. 1). This allows very precise welds in the order of tenths of millimeter, like when welding foils and membranes (Fig. 3). On the other side, the high power beam can weld 200 mm of stainless steel or even 300 mm of aluminum while the weld stays just few centimeters wide and only minimum distortion occurs.

As the electron beam is easy to control, either by focusing or by deflection, it is possible to guide the beam's energy to a specific spot on the work-piece with ease. Using computer control, the welding can be performed even with very complex trajectory. The beam can also "jump" very quickly among



Fig. 3. Membrane bellow

several points and weld at several places at the same time (multi-beam welding).

By electron beam welding, wide range of materials can be welded, from alloy and stainless steels, copper, aluminum and nickel alloys to reactive metals (e.g. titanium, zirconium or tantalum) and refractory metals (tungsten, molybdenum). It is also possible to weld dissimilar metals even with very different properties. For example, combinations like Al-Cu (Fig.4), Al-Ti, stainless steel-W or Mo and others can be joined, even though other welding methods lead to fragile welds.

However, there are also some disadvantages. In the first place, it is the need for vacuum. This not only imposes limitation on the size of the welded components but also has a substantial influence on the cost of the equipment. In some cases at specific conditions, the welding itself can be done at lower vacuum or even at atmospheric pressure. A differential pumping system must be used then, because vacuum is still needed inside the electron gun, especially in the cathode chamber.

During the welding, a penetrating X-ray radiation is generated and must be shielded. For accelerating voltage up to 60 kV, the walls of vacuum chamber and gun column are usually enough. For higher voltages, additional shielding (like lead sheets) is needed.

The first applications of electron beam welding were connected to nuclear industry, followed by aerospace (Fig.5) and automotive industry. Since then, the electron beam welding has spread to all kinds of industry, from power engineering and machine construction, vacuum (Fig.6) and cryogenic technology (Fig.7) to medical technology and very fine mechanics.

By proper design, electron beam welding can reduce costs of fabrication, e.g. by reducing removed material and/or reducing the complexity of the machining. It even makes possible to create complicated parts, e.g. with curved cavities. Small HAZ allows welding near heat sensitive parts, like sensors, ceramic feed-throughs and various filler materials.

Electron beam welding is also used for repairs, from renovating the turbine blades to very fine sensors, due to fine and precise welds.

- [1] Meleka A. H.: Electron-beam Welding: Principles and Practice. McGRAW-HILL, London 1971.
- [2] Schultz. H. Electron Beam Welding. Abington Publishing, Abington 1994. (Czech translation L. Zobač, ÚPT AV ČR).
- [3] Zobač. L.: Electron beam welding technology. ISI AS CR, Brno 2007, internal material.

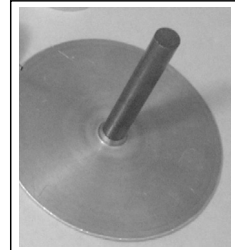


Fig. 4. Dissimilar metals weld (Al-Cu).



Fig. 5. Gear from aircraft industry



Fig. 6. Vacuum feed through



Fig. 7. LN2 cryostat - 8 welds

HOW TO PREVENT HYDROCARBON CONTAMINATION IN SEM

M. Dvořáková and F. Mika

Institute of Scientific Instruments ASCR, Královopolská 147, 612 64 Brno, Czech Republic
dvorakova@isibrno.cz

Electron beam-induced contamination is one of the most undesirable effects encountered in the scanning electron microscopy (SEM). Hydrocarbon molecules (HC) are usually formed in the vacuum of the microscope as a result of the partial pressure of hydrocarbons or silicon oils from the diffusion pump and the grease of vacuum seals and fingerprints. However, hydrocarbons are already deposited on the specimen in the open air so that an ultra-high vacuum alone does not solve the problem [1]. HC contaminants adsorbed on the surface or as surface films interacting with the incident electron beam can distort the final image of the specimen. The distortion may take the form of deposits of polymer in the scanned area, a darkening of the scanned area, a loss of resolution, or other artifacts. Contamination can be reduced by cool-traps, by chemical purging, by using cleaner pumps or by plasma cleaning [2].

Concerning cool-traps, liquid N₂ is used to cool the anti-contamination device (it can be located above the diffusion pump or under the pole piece). After cooling the amount of contamination is partly reduced but the remains are still high. After the use the plasma cleaning the amount of contamination is greatly reduced, the amount deposited is far less than with the liquid nitrogen-cooled anti-contamination device [3]. On the basis of this we used the plasma cleaning to reduce HC contamination.

The plasma cleaning is a method that removes environmental HC and HC from any other source from the inside of electron microscopes by oxidation [2]. Oxidation is performed by oxygen radicals produced by the Oxygen Radical Source (ORS) in plasma from air admitted into the ORS plasma chamber. The oxygen radicals are carried by convention (viscous vacuum flow caused by the pressure differential between the source and pumps) into the rest of the chamber. Here they react when they collide with contaminant molecule vapors or with adsorbed contaminant molecules on surfaces. The O converts HC contamination into volatile short chain ketones, alcohols, H₂O, CO and CO₂ molecules that are then removed by the roughing pump [4].

To prove this method, the contamination was formed on a silicon wafer sample and on a copper specimen during 10 and 5 minutes, respectively, of continuous electron beam irradiation (Fig. 1 and 2 on the left). These specimens were observed in scanning electron microscope Vega TS 5130MM. The accelerating voltage was 5 kV, work distance was about 10 mm and pressure in the chamber was 10⁻³ Pa. The image signal was collected with a standard Everhart-Thornley detector. Then XEI Scientific Evactron De-Contaminator was used. Both the specimens were cleaned after 20 minutes successfully (Fig. 1 and 2 on the right).

[1] Reimer, L. *Scanning Electron Microscopy*, Springer, Berlin (1998)

[2] Vane R., Carlino V. *Microscopy and microanalysis 2005 Honolulu*, Abstract 233

[3] Vladár, A. E. et al. *Proc. SPIE 4344* (2001), p. 835

[4] <http://www.evactron.com/>

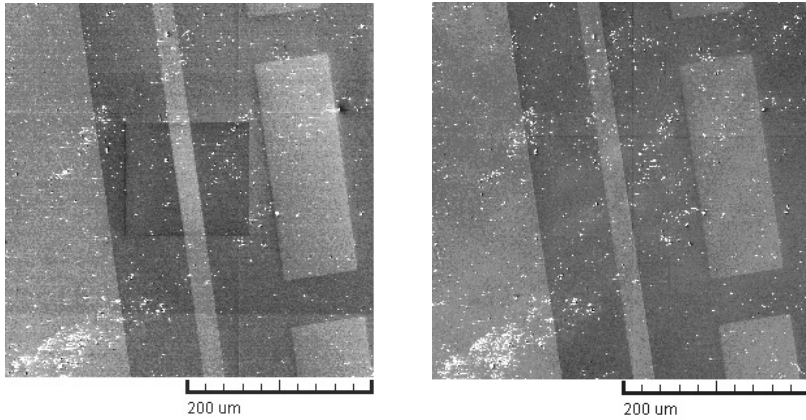


Fig. 1. A p-type doped patterns ($1 \times 10^{19} \text{ cm}^{-3}$ of boron atoms) made on an Si (100) n-type substrate ($1 \times 10^{15} \text{ cm}^{-3}$ of phosphorous atoms), SE image, primary energy 5 keV. Left: after 10 minutes of continuous electron beam irradiation with primary current 68,5 pA. Right: after the use of Evactron (the conditions of plasma cleaning: 0,4 Torr, 14 W, 20 minutes).

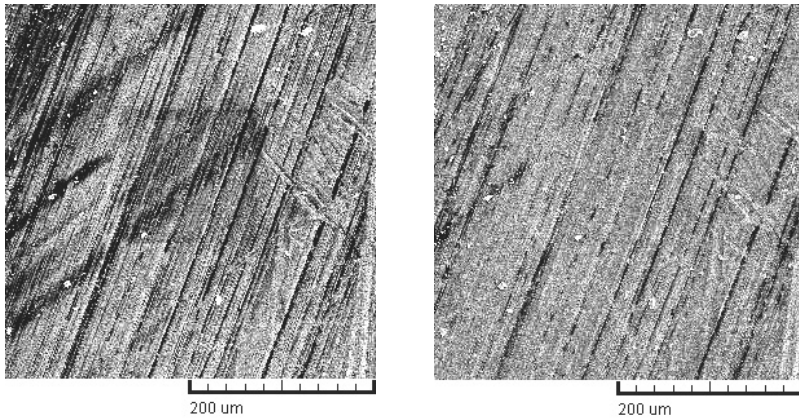


Fig. 2. A copper specimen. Left: after 5 minutes of continuous electron beam irradiation with primary current 4,8 nA. Right: after the use of Evactron (the conditions of plasma cleaning: 0,4 Torr, 14 W, 20 minutes).

MODULAR MONTE CARLO SIMULATION INCLUDING SECONDARY ELECTRON RAYTRACING

D. Gnieser¹, C.G. Frase¹, H. Bosse¹, I. Konvalina² and I. Müllerová²

¹Physikalisch-Technische Bundesanstalt, Bundesallee 100, 38116 Braunschweig, Germany

²Institute of Scientific Instruments, Academy of Sciences of the Czech Republic, v.v.i., Královopolská 147, 612 64 Brno, Czech Republic

A Monte Carlo simulation program for the modeling of image formation in scanning electron microscopy is presented. A key feature of the program is its modular design, so the different aspects of image formation (i.e. forming of the electron probe, specimen topography model, probe-sample-interaction, electron detector model, image processing) are arranged in separate program modules. The modules can easily be replaced or enhanced to adapt the program to new simulation tasks. The program is written in C++ and uses object-oriented programming techniques. Data exchange between the different program modules is performed by defined software interfaces. Thus, third party simulation code can easily be integrated into the program.

For the electron probe, different models can be applied: a point-shaped electron beam, a parallel beam with a Gaussian intensity profile, or a conical beam with a defined focal plane and aperture angle. The point-shaped electron beam can be combined with a subsequent convolution of the resulting SEM image with an arbitrary probe profile.

Various specimen topography modules are available ranging from simple layer structures and 2D line structures to complex 3D structures, offering a flexible system of specimen definition. Complex 3D structures are composed of basic geometric bodies and are defined by a simple script language. The specimen definition scripts can be transformed to VRML (virtual reality modeling language) format for 3D visualization.

The electron-specimen-interaction module simulates the electron diffusion in solid state and the generation and emission of secondary electrons (SE). Elastic scattering is based on tabulated Mott scattering cross sections, calculated by Salvat and Mayol [1], inelastic scattering is modeled by the Bethe formula in the modification of Joy and Luo [2]. SE generation and transport is taken into account by a simple but effective model based on a mean excitation energy and a mean SE free path.

The detector module simulates the detection of backscattered electrons (BSE), transmitted electrons (TE), and secondary electrons. In the SE mode, the detection characteristics of an InLens SE detector are modeled by electron raytracing techniques, based on the work of Konvalina and Müllerová [3]. A three-dimensional model of the objective lens including the annular detector is established and the trajectories of the secondary electrons in the electric and magnetic field are calculated with the program SIMION 7.0 [4] and EOD [5]. However, a Monte Carlo program calculates millions of electron trajectories, so it is far too time-consuming to simulate every single SE individually. Instead, look-up tables were generated for SE with a starting energy of 1 – 50 eV and a starting angle of 0° – 90°, for different sets of SEM parameters (e.g. beam energy and working distance). The Monte Carlo program uses these pre-calculated look-up tables to decide whether an emitted electron hits the detector.

The SE raytracing module was tested in comparison with measurements of the topographic contrast at platinum-coated silicon structures: The silicon topography is composed of trenches with different aspect ratios (i.e. a profile depth of 0.5 μm and a trench width of 0.2 μm – 1.5 μm) resulting in a variation of the topographic contrast. Image formation at the trenches can be regarded as a superposition of different effects: SE1 and SE2 are emitted in an angular cosine distribution, relatively to the surface normal. However, SE emitted from a trench in a low angle are reabsorbed by the sidewalls of the trench. Furthermore, backscattered electrons emitted from trenches can also be reabsorbed by the sidewalls and produce additional secondary electrons (SE3) with a different angular characteristic. So, not only the total amount of SE emitted from a trench differs from a plane surface, but also the angular distribution is different. Therefore, further contrast alteration occurs by the angular-selective SE detector characteristics: high-angle electrons pass the central detector bore and cannot be detected. Low-angle electrons with higher energies hit the pole piece of the objective lens and are not detected too.

The simulated topographic contrasts are in good accordance with the measurement results. Furthermore, it could be observed that the topographic contrast is greatly influenced by the working distance. An increase of working distance from 2 mm to 4 mm resulted in a contrast decrease of about 15 %. Therefore, the detector characteristics are an essential part of signal formation and have to be taken into account for a correct modeling of SEM contrasts.

Further tests of the Monte Carlo program have been performed in various application examples like TE imaging of nanoparticles and SE and BSE imaging of complex 3D semiconductor and metal structures. The testing is performed by comparing the simulation with measurement results and with results of other Monte Carlo simulation programs [6, 7].

- [1] F. Salvat, R. Mayol: "Elastic Scattering of Electrons and Positrons by Atoms. Schrödinger and Dirac Partial Wave Analysis." *Comp. Phys. Comm.* 74, pp.358-374, (1993)
- [2] D.C. Joy, S. Luo, "An Empirical Stopping Power Relationship for Low-Energy Electrons", *SCANNING* 11(4), pp.176-180, (1989)
- [3] I. Konvalina, I. Müllerová: "The Trajectories of Secondary Electrons in the Scanning Electron Microscope", *SCANNING VOL. 28*, pp. 245-256, (2006)
- [4] D.A. Dahl, "SIMION 3D Version 7.0", *Proc 43rd ASMS Conference on Mass Spectrometry and Allied Topics*, Santa Fe, p. 717 (1995), (<http://www.simion.com>)
- [5] B. Lencová, J. Zlámal: "The development of EOD program for the design of electron optical devices", *Microscopy and Microanalysis*, vol. 13, pp. 2-3, (2007)
- [6] L. Reimer, M. Kässens, L. Wiese, "Monte Carlo Program with free Configuration of Specimen Geometry and Detector Signals", *Microchim. Acta* 13, pp.485-492, (1996)
- [7] J.R. Lowney: "MONSEL-II: Monte Carlo Simulation of SEM Signals for Linewidth Metrology", *Microbeam Analysis* 4, pp. 131-136, (1995)

ADVANCE IN THREE-DIMENSIONAL BOUNDARY ELEMENTS METHOD: SURFACE CHARGE SINGULARITIES IN THE PRESENCE OF DIELECTRICS AND MAGNETIC MATERIALS

Dmitry Greenfield

A.M. Prokhorov General Physics Institute, RAS, Photoelectronics Dept.

38, Vavilov St, Moscow 119991, Russia

dm.greenfield@yahoo.ru +7(926)2103189

The boundary elements method (BEM) is known to be the most accurate approach to the Laplace-Dirichlet problem of electrostatic and non-saturated magnetic modeling in computational charged particle optics. As applied to the three-dimensional problems, its efficiency is based on reduction of determining 3D potential distribution to solving a first-kind Fredholm integral equation with respect to 2D charge density distribution upon the surfaces. Nevertheless the mathematical problem of conditionality of the first-kind Fredholm integral equations is not still completely solved. Generally speaking, such equations with regular kernels prove to be ill-defined and therefore the mathematical simulation can be hardly based on their numerical solutions. However Voronin and Tsetsocho showed in 1981 that the logarithmic singularity, typical of the Coulomb-type kernels for the planar electrostatic problems, makes the corresponding first-kind Fredholm integral equation well-conditioned within a rather wide class of functions [1]. The situation is quite similar in the 3D case where the $1/r$ kernel singularity plays the analogous role.

The Voronin-Tsetsocho theorem has been strictly proved for the Laplace-Dirichlet problem in 2D domains with smooth boundaries at which the surface-charge density distribution has to be looked for within the class of finite Hölder functions. The problem becomes more complicated if the boundary is only *piecewise* smooth and contains sharp ribs and corners, such as electrodes (or magnetic pole pieces) have in most practical cases. The surface-charge distribution on a conducting surface with irregular points is singular and may tend to infinity near the ribs and corners. If we know the asymptotic behavior of the surface charge density σ near the singular points of the boundary, we can "pick out" the singularity by representing σ in the multiplicative form $\sigma = \Psi \sigma'$, with beforehand known singular function Ψ and the smooth function σ' . From mathematical viewpoint, such substitution returns the solution into the class of Hölder functions but modifies the kernel of the integral equation. It is of profound importance that the modified kernel still preserves the weak integrable singularity, and therefore, according to the Voronin-Tsetsocho theorem, the transformed first-kind Fredholm equation with respect to σ' proves to be well-conditioned. In practical implementation of BEM, all possible charge singularities may be introduced into the set of shape functions Ψ_i employed for discretization of the integral equation before solving it numerically. Therefore the problem of accurate determination of the surface-charge singularity structure is of profound importance for correct implementation of BEM for both electrostatics and magnetic problems.

In most cases the main part of the singularities may be described by the power-like functions like $\sigma \sim r^{-\gamma}$ where r is the distance to the irregular point and the exponent index γ takes its values in the range $0 < \gamma < 1$. Commonly, the researches use the simple formula

$$\gamma = \frac{\pi - \alpha}{2\pi - \alpha} \quad (1)$$

which springs from the theory of conformal mapping and ties together the singularity index γ with the apex angle α at which two conductive faces meet at a common rib [2]. In this paper we touch the question how the singularity index can be determined from geometrical structure of the boundary electrodes and insulators in more complicated cases, involving dielectric/magnetic materials and the 3D corners.

First let consider the two-faced conductive wedge in the presence of a number of homogeneous insulating wedges with dielectric constants ε_n as shown in Fig. 1. According to Mantič at al. [3] and Birkhoff [4], we write down the 2D Laplace equation in polar coordinates

$$\Delta\varphi = \varepsilon(\theta) \left(\frac{\partial^2\varphi}{\partial r^2} + \frac{1}{r} \frac{\partial\varphi}{\partial r} \right) + \frac{1}{r^2} \frac{\partial}{\partial\theta} \varepsilon(\theta) \frac{\partial\varphi}{\partial\theta} = 0 \tag{2}$$

and construct its solution in the form of the expansion

$$\varphi(r, \theta) = \sum_m R_m(r) Y_m(\theta) \quad , \tag{3}$$

where Y_m are non-trivial solutions to the Sturm-Liouville spectral problem

$$\left(\varepsilon(\theta) Y_m' \right)' + \lambda_m^2 \varepsilon(\theta) Y_m = 0 \tag{4}$$

with zero boundary conditions

$$Y(0) = Y(2\pi - \alpha) = 0 \quad , \tag{5}$$

and the coupling condition

$$\varepsilon_{n+1} Y'(\theta_n + 0) - \varepsilon_n Y'(\theta_n - 0) = 0 \tag{6}$$

to be obeyed at any point θ_n of dielectric constant discontinuity. Since the operator $(\varepsilon Y)'$ is self-conjugated and positively defined on the set of twice piecewise continuously differentiable functions satisfying (5), the eigenvalues of the problem (4-6) are real and positive (this is why they are denoted here as λ_m^2), and we can number them in the increasing order $0 < \lambda_0 < \lambda_1 < \dots$. The finite functions $R_m(r)$ are equal to $C_m r^{\lambda_m}$ where C_m are some constants. The asymptotic behavior of electric potential in the wedge apex vicinity is determined by the term with the smallest power index of the radial coordinate r , so that $\varphi = O(r^{\lambda_0})$ at $r \rightarrow 0$. The surface-charge density, being proportional to the normal derivative of the potential, has the singularity index $\gamma = 1 - \lambda_0$.

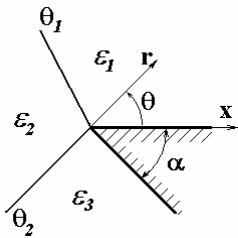


Fig.1. The case of homogeneous dielectrics adjoining a conductive wedge

The transfer-matrix method of solving the spectral problem (4-6), as proposed by Mantič et al. [3], reduces it to solving the transcendental equation $R(\lambda) = 0$ where $R(\lambda)$ is the element of the matrix

$$\mathbf{M}(\lambda) = \begin{vmatrix} P(\lambda) & R(\lambda) \\ Q(\lambda) & S(\lambda) \end{vmatrix} = \mathbf{M}_N(\lambda) \dots \mathbf{M}_2(\lambda) \mathbf{M}_1(\lambda) \tag{7}$$

obtained by multiplication of the matrixes

$$\mathbf{M}_k(\lambda) = \begin{vmatrix} \cos(\lambda \Delta\theta_k) & \varepsilon_k^{-1} \sin(\lambda \Delta\theta_k) \\ -\varepsilon_k \sin(\lambda \Delta\theta_k) & \cos(\lambda \Delta\theta_k) \end{vmatrix}, \quad \Delta\theta_k = \theta_k - \theta_{k-1} \quad (8)$$

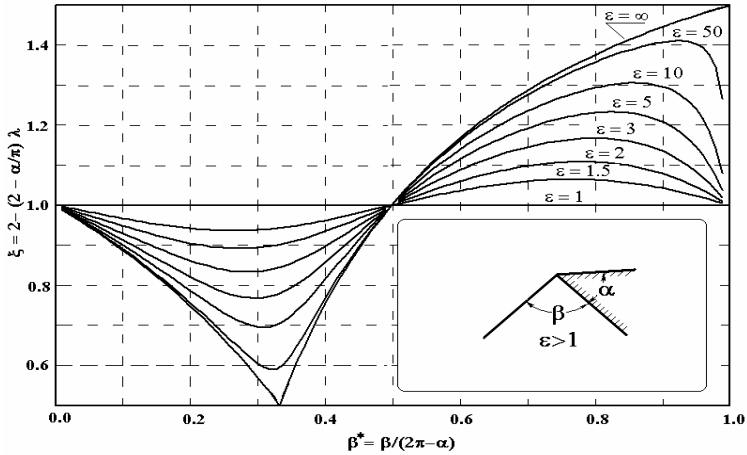


Fig. 2. The graphical representation of the function $\xi(\beta^*, \varepsilon)$ for the case of conductive and dielectric wedges with common apex

Fig. 2 provides some computational results for the practically important case of one dielectric wedge touching a conductive wedge, with the rest volume considered as vacuum with $\varepsilon = 1$. It was convenient to introduce a graphically given function ξ of the dielectric constant and the normalized angle $\beta^* = \beta / (2\pi - \alpha)$. The singularity index appears in the form

$$\gamma = \frac{\pi \xi(\beta^*, \varepsilon) - \alpha}{2\pi - \alpha} \quad (9)$$

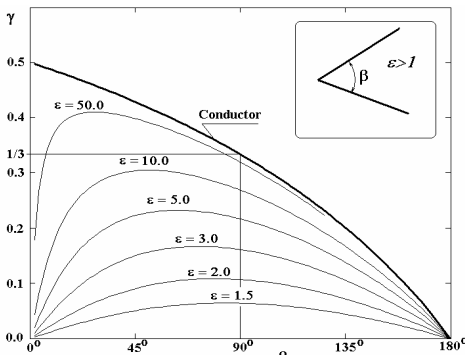


Fig.3. The case of a pure dielectric wedge

which differs from (1) by the correcting coefficient ξ .

The case of a pure dielectric wedge, which is also frequently encountered in practical modeling, may be approached in similar way, but the equation $\det \mathbf{M}(\lambda) = 0$ is to be solved instead. Figure 3 shows numerically calculated values of the singularity index as function of the wedge's apex angle.

The obtained results may be immediately used in the magnetic problems after substitution the magnetic permeability μ for the dielectric constant ε .

A general approach to the three-dimensional surface-charge singularity analysis was proposed by G. Fichera [5]. This problem may be also reduced to the spectral problem $L[Y_m] + \Lambda_m Y_m = 0$ where the eigenfunctions $Y_m(\theta, \phi)$ are defined on the unit-radius spherical segment S^+ , external with respect to the conducting corner as shown in Fig. 4, and vanish on the segments boundary ∂S^+ . The operator

$$L = \frac{1}{\sin \theta} \frac{\partial}{\partial \theta} \sin \theta \frac{\partial}{\partial \theta} + \frac{1}{\sin^2 \theta} \frac{\partial^2}{\partial \phi^2} \quad (10)$$

is the Beltrami-Laplace operator on the unit sphere S . With the minimal eigenvalue Λ_0 found, the singularity index is determined by the formula

$$\gamma = \frac{3 - \sqrt{1 + 4\Lambda_0}}{2} \quad (11)$$

The spectral problem was numerically solved for the prism-type conducting corner constructed of two right angles and one arbitrary angle $\alpha \in [0, \pi]$ as shown in Fig. 5.

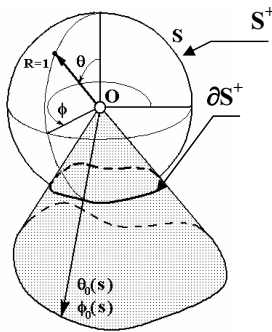


Fig.4. The 3D conducting corner and the auxiliary unit-radius sphere

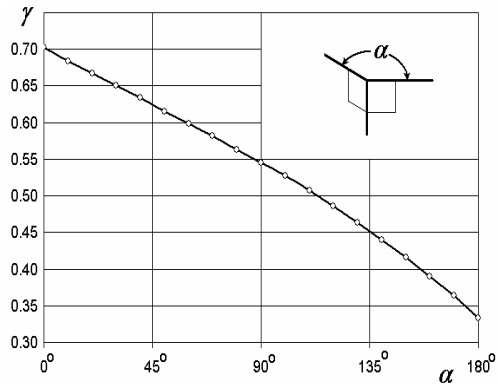


Fig.5. The singularity index for the 'prism' corner as function of the apex angle

- [1] V.V. Voronin and V.A. Tsetsoho. Numerical solution of the first-kind integral equation with logarithmic singularity by means of the method of interpolation and collocation // Journal of computational mathematics and mathematical physics, vol. 21 (1981), no. 1, pp. 40 – 53 (in Russian)
- [2] L.D. Landau and E.M. Lifshitz, Electrodynamics of Continuous Media // Pergamon, NY, 1984
- [3] V. Mantič, F. Paris, J. Berger. Singularities in 2D anisotropic potential problems in multi-material corners. Real variable approach // Int. J. of Solids and Structures, vol. 40 (2003) pp. 5197 – 5218
- [4] G. Birkhoff. Angular singularities of elliptic problems. // J. Approximation Theory, vol. 6 (1972), pp. 215 – 230
- [5] G. Fichera // Russian Mathematical Surveys, vol. 30 (1975), no. 3 (183), pp. 107 – 127

PERTURBATION METHODS OF ELECTRIC AND MAGNETIC FIELD MODELLING IN CHARGED PARTICLE OPTICS

Dmitry Greenfield and Mikhail Monastyrskiy

Photoelectronics Department, A.M. Prokhorov General Physics Institute,
Russian Academy of Sciences

38, Vavilov St, Moscow 119991, Russia dm.greenfield@yahoo.ru +7(926)2103189

In this paper we consider the problem of evaluating electric and magnetic field perturbations resulted from small deviations of the geometry and voltages of the electrodes and magnetic circuits forming the electron-optical system boundary (hereafter the *boundary variations*) from some ideal state which is further called *nominal*. This problem is the starting point and main issue for many charged particle optics problems, including mechanical tolerances computation, fringe effects evaluation, electron-optical system optimization, etc.

Indeed, it is very important in practice to know what accuracy of mechanical parts manufacturing and feeding voltages stability are needed to obey technical requirements on a particular device. If the nominal geometry of the system in question is axisymmetric or planar, those questions commonly bring us to a three-dimensional boundary-value problem being very close to the nominal two-dimensional one. We find ourselves in the same situation if we need to estimate the fringe field contribution in a planar system. In all those cases, the direct use of general 3D field calculation algorithms is far not the better way out. Much more accurate and reliable results can be obtained with the use of perturbation theory which allows explicit correlations between the small boundary variations and electromagnetic field perturbation in the domain of interest. Inasmuch as any numerical optimization procedure assumes a step-by-step changing of the structural parameters involved, numerical optimization in charged particle optics also requires the knowledge on partial contribution of small boundary variations to electron-optical characteristics in question.

In 1876 Bruns put forward a method to calculate the gravitational field perturbation induced by the deviation of the Earth shape from the ideal sphere [1, 2]. One and seventy years later, in 1947, Bertein for the first time applied the Bruns' approach to the problems of electrostatics and electron optics [3, 4]. Since that the Bruns-Bertein method was used for tolerances evaluation in charged particle optics by many authors, including Sturrock [5], Glaser and Schiske [6], Der-Schwartz and Kulikov [7], Janse [8], Munro [9] and others. The main idea of the method is replacing the real boundary perturbation by some equivalent potential perturbation defined on the nominal boundary in terms of the unperturbed potential gradient. More exactly, if φ^0 is unperturbed potential distribution, $\delta\mathbf{R}$ is boundary deformation vector, and $\delta\varphi$ is distribution of the potential perturbation in space, we easily come to the Dirichlet problem for Laplace equation $\Delta[\delta\varphi]=0$ with the boundary condition $\delta\varphi = -\langle \delta\mathbf{R}, \nabla\varphi^0 \rangle$ on the unperturbed boundary Γ_0 .

Strictly speaking, the Bruns-Bertein method can be applied only to the domains with smooth boundaries upon which the gradient $\nabla\varphi^0$ is regular and finite. This condition proves to be certainly violated if the boundary possesses some singular points or lines (edges, ribs, corners, etc.) which are, as a rule, present in any, pithy enough, practical problem. It is well known that in those cases the gradient $\nabla\varphi^0$ tends to infinity near the boundary singularities,

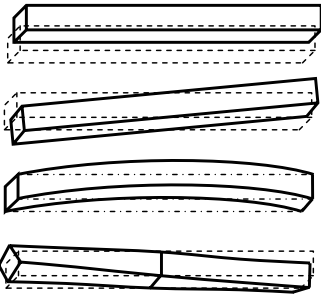


Fig. 1. Examples of planar geometry perturbations (shift, tilt, sagging, twist)

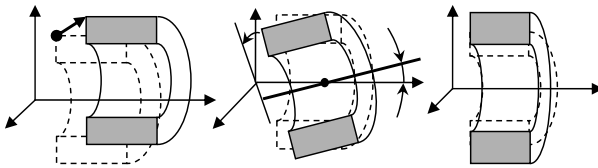


Fig. 2. Examples of axisymmetrical geometry perturbations (shift, tilt, ellipticity)

which makes the calculation process low-accurate and essentially unstable. Another difficulty arises if both sides of the infinitely thin charged surface are immersed into the optically active field area— in this case the double layer potential is needed to calculate potential perturbations with integral equations method.

This paper represents some new features of another, more versatile and numerically efficient, perturbation approach [10] based on direct variational analysis of the first-kind Fredholm integral equation in terms of the so-called *Lagrangian variations* of the boundary. First, the Fedorenko' variational scheme is applied for varying the Dirichlet problem for Laplace equation in general 3D case, and both the *integral variational equation* and the *conjugate integral equation* for the corresponding Green function are obtained. The integral variational equation is then applied to the case of small 3D perturbations of

axisymmetric (Fig. 1) and planar (Fig. 2) nominal boundary, with some relevant examples considered. Finally, we describe a perturbation-based numerical approach for accurate evaluation of potential perturbations caused by the *locally strong* 3D boundary perturbations.

References

1. H. Bruns. // J. Math., vol. **81** (1876), p. 349
2. N.I. Idelson. *The theory of potential* // ONTI, Moscow-Leningrad, 1936 (in Russian)
3. F. Bertein. // Ann. de Radioelectricite, vol. **2** (1947), p. 379
4. F. Bertein. // Ann. de Radioelectricite, vol. **3** (1948), p. 49
5. P.A. Sturrock. // Philosophical transactions of the Royal Society of London, Ser. A, vol. **243**, 862 (1951), pp. 387-429
6. W. Glaser and P. Schiske. // Zs. angewandte Physik, **5** (1953), p. 329
7. G.V. Der-Schwartz and Yu.V. Kulikov. // Radioengineering and Electronics, vol. **32**, (1962), p. 2067 (in Russian)
8. J. Janse. *Optik*, **33** (1971), p. 270
9. E. Munro. *Finite-difference programs for computing tolerances for electrostatic lenses* // J. Vac. Sci. Technol., vol. **B 6** (3), (1988) pp. 941 – 948
10. M.A. Monastyrskiy and S.V. Kolesnikov. *New method of calculating the potential perturbations in the problems with slightly perturbed axial symmetry* // Zhurnal Tekhnicheskoi Fiziki, vol. **53** (1983), no. 9, pp. 1668 – 1677 (in Russian). English version - Soviet Physics – Technical physics, vol. **28**

COULOMB DYNAMICS OF FEMTOSECOND ELECTRON BUNCHES IN TIME-DEPENDING ELECTRIC FIELDS

Dmitry Greenfield and Mikhail Monastyrskiy

Photoelectronics Department, A.M. Prokhorov General Physics Institute,
Russian Academy of Sciences 38, Vavilov St, Moscow 119991, Russia
dm.greenfield@yahoo.ru +7(926)2103189

Ultrashort electron bunches provide a promising instrument for investigation of the physical and chemical processes with femtosecond time resolution, for example, in the Time Resolved Electron Diffraction (TRED) experiments [1]. Traditionally, the femtosecond electron bunches are generated with the use of photoelectron tubes in which the electrons originated from a laser-activated photocathode are accelerated and focused by electric field. In TRED experiments, those electrons experience diffraction upon the sample after a controllable time delay after the sample has been excited with the ultrashort laser pulse. The diffraction pattern formed on an image receiver carries direct information on molecular structure of the compounds under investigation in a certain time moment, thus giving the possibility to see a kind of ‘molecular movie’, the temporal resolution of which depends upon duration of the electron probe.

There are three major factors which prevent the laser-induced photoelectron bunches from temporal compression: initiating laser radiation duration, chromatic spread of the photoelectrons, and Coulomb repulsion between the electrons while traveling from the photocathode to the sample. We have proposed [2], and it was then confirmed by other authors [3], that using non-stationary electric fields in so-called dynamic photoelectron tubes may suppress the two first factors. All the more, the factor of Coulomb repulsion is still very significant.

Electrons traveling in the external electric field Φ^{ext} obey the Lorenz equation

$$\frac{d^2 \vec{x}}{dt^2} = \frac{e}{m} \nabla(\Phi^{ext} + \Phi_C) \quad (1)$$

where

$$\Phi_C(\vec{x}) = \sum_{n=1}^N \frac{e}{|\vec{x} - \vec{x}^{(n)}|} + \text{mirror charge field} \quad (2)$$

is the ‘internal’ Coulomb potential of the bunch containing N particles. Every individual particle may be described with a set of initial parameters: the emission time moment τ , initial energy components $\varepsilon_x, \varepsilon_y, \varepsilon_z$ and the initial coordinates x_0, y_0 (hereafter we consider the axially symmetrical systems with the axis coinciding with z).

Integrating (1) for every individual particle is cumbersome; it is much more effective to use aberrational approach instead. With this aim in view, we represent the solution in the form of Taylor expansion

$$x^i(t; \underbrace{\sqrt{\varepsilon_x}, \sqrt{\varepsilon_y}, \sqrt{\varepsilon_z}, x_0, y_0, \tau}_{\xi_\alpha}) = x_0^i(t) + \sum_\alpha x_\alpha^i(t) \xi_\alpha + \frac{1}{2} \sum_{\alpha, \beta} x_{\alpha\beta}^i(t) \xi_\alpha \xi_\beta + \dots \quad (3)$$

where the initial conditions are treated as small parameters and combined together in the vector ξ_α . We also introduce the arrival time expansion

$$T(z; \xi) = T_0(z) + \sum_{\alpha} T_{\alpha}(z) \xi_{\alpha} + \frac{1}{2} \sum_{\alpha, \beta} T_{\alpha\beta}(z) \xi_{\alpha} \xi_{\beta} + \dots \quad (4)$$

which denotes the time moment when a particle reaches the plane $z = z(t; 0 \dots 0)$. The first-order coefficients in (3) and (4) are interrelated with the formula $T_{\alpha}(z(t; 0)) = -z_{\alpha}(t) / z_0(t)$. The expansion (4) holds everywhere except for the very starting point $t = 0$ where the particle velocity $z_0 = 0$, and its coefficients determine the temporal spread of the electron bunch at a certain plane. The most significant coefficients are the ‘temporal’ magnification T_{τ} and the first-order chromatic aberration $T_{\sqrt{\varepsilon_z}}$. It may be shown that these coefficients are always proportional [2]

$$T_{\sqrt{\varepsilon_z}} \equiv -\frac{\sqrt{2m}}{eE_0} T_{\tau} \quad (5)$$

where E_0 is the electric field at the photocathode. In static field, the time-of-flight $T(z; \dots \tau) - \tau$ doesn’t depend on the emission moment τ and, consequently, the temporal magnification $T_{\tau} \equiv 1$. According to (5), the chromatic aberration coefficient is also constant, and namely its contribution defines the resolution limit of nowadays electron tubes for TRED purposes. The beam motion in dynamic (time-dependent) field is another matter – T_{τ} may change in time and reach zero at some point on the optical axis. In this point, referred to as temporal focus, the first order chromatic aberration also vanishes which offers the promising opportunity to compress the electron bunch down to durations of several femtoseconds, practically unachievable in static tubes.

The effect of temporal compression may be described in terms of evolution of the coefficient T_{τ} as a function of the coordinate z . If we introduce the kinetic energy W and the first variation of the full energy T_{τ} as

$$W(z, \xi) = m \frac{z_0^2(t)}{2} \Big|_{t: z(t, 0) = z} \quad \text{and} \quad E_{\tau}(z) = \frac{\partial}{\partial \tau} \left[m \frac{z(t, \xi)^2}{2} + e\Phi(z) \right]_{\substack{t: z(t, 0) = z \\ \xi = 0}} \quad (6)$$

we are in position to derive [4] the system of two differential equations

$$\frac{dT_{\tau}}{dz} = -\frac{\sqrt{m}}{(2W)^{3/2}} E_{\tau} \quad (7)$$

$$\frac{dE_{\tau}}{dz} = e \frac{\partial^2 \Phi}{\partial t \partial z} T_{\tau} - \frac{4\pi e}{S(z)} J_0 \quad (8)$$

with initial conditions $T_{\tau}(0) = 1$ and $E_{\tau}(0) = 0$. The last term in (8) is introduced to account for the Coulomb repulsion in the electron bunch, which is considered as a homogeneously charged disk as shown in Fig. 1. Here $S = \pi r_b^2$ is the effective bunch’ cross-section and J_0 is the initial current of the electrons right after emission.

The equation (8) shows the important difference in Coulomb dynamics of electron bunches in static and dynamic systems. In static fields, the first term in the right part is zero and the second term has constantly negative sign. As a result, the variation of the full energy E_{τ} is always negative which leads, according to (7) to permanent growth of the temporal

magnification: $T_\tau(z) > 1$ for $z > 0$. No temporal focusing is possible - the bunch duration may only grow with time. In dynamic fields, the mixed derivative of the electric potential may be done positive, so that the first term in (8) would be equal or exceeding the second term by its absolute value, thus effectively suppressing the effect of Coulomb repulsion. The latter actually results in some shift of the temporal focus from its nominal position, which may be corrected by appropriate adjusting the electrode voltages and their temporal dependences.

It should be noted here that the second term in (8) is based upon the coarse assumption that the charge density is homogeneous within the bunch. Moreover, the accurate modeling of the electron bunch requires taking into account all terms of the expansions (3) and (4) up to the second-order variations at least. In our computer modeling we preserve the third-order terms and use a special algorithm of space-charge effect modeling which combines efficiency of the aberrational expansions with accuracy of integrating the individual Lorentz equations. To analyze the effect of Coulomb repulsion on ultrashort bunch formation, we used a special numerical algorithm based on the improved Barnes-Hut method [5].

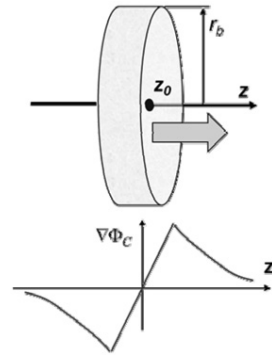


Fig. 1. The model of homogeneously charged electron bunch. Coulomb electric field is linear within the bunch

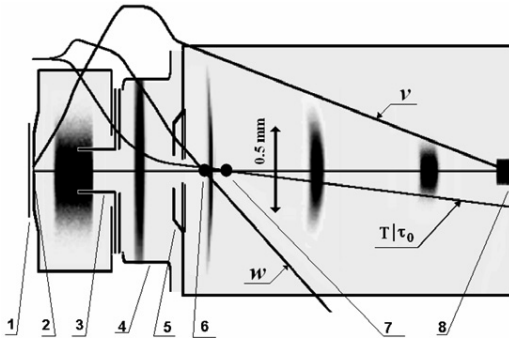


Fig. 2. Structural scheme of the photoelectron gun :

- 1 – photocathode,
- 2 – fine-structure grid,
- 3 – temporally focusing electrode,
- 4 – spatially focusing electrode,
- 5 – anode, 6 – crossover point,
- 7 – temporal focus point,
- 8 – CCD image receiver.

The bunch shape at different time moments is essentially scaled-up with respect to the electrode dimensions.

The object of our simulation was the electron tube shown in Fig. 2. The experimental model of this device was than manufactured and experimentally tested in the Photoelectronics Department of the General Physics Institute of Russian Academy of Sciences. The tube is capable of operating in two modes: static and dynamic. In the static mode, the voltages on all electrodes are fixed and chosen in such way that the electron bunch is being focused on the image receiver 8. The beam duration in the crossover point was found to be 500 fs if no space-charge is taken into consideration. With the number of electrons being $N = 300$, the bunch duration doubled and reached 1000 fs.

In the dynamic mode, the voltage on the temporally focusing electrode 3 ramps from $U_{initial} = 960V$ to $U_{final} = 1960V$ during $\Delta t = 0,35ns$ when the electron bunch travels from the grid (2) to this electrode. Under these conditions, temporal focusing occurs in the

point 7 situated in the close vicinity of the crossover 6. It corresponds to the minimum of the curve 1 in Fig. 3 $\delta T = 250$ fs. Then we have repeated the simulation with the Coulomb repulsion taken into account with $N = 1000$, $N = 2000$ and $N = 3000$ electrons in the bunch. The bunch duration δT was growing. However scanning the voltage ramp $\Delta U = U_{final} - U_{initial}$ in the range $900 \div 1700$ V revealed the minimums of bunch duration for every N . Thus the operation mode of the tube can be adjusted to suppress the Coulomb repulsion for any bunch intensity and obtain the shortest duration. The minimal possible bunch duration still depends upon the number of particles but much slower than in the static case. So, δT doubles up to 500 fs only with $N \approx 1000$ and reaches the value of 1000 ps with only $N \approx 4000$.

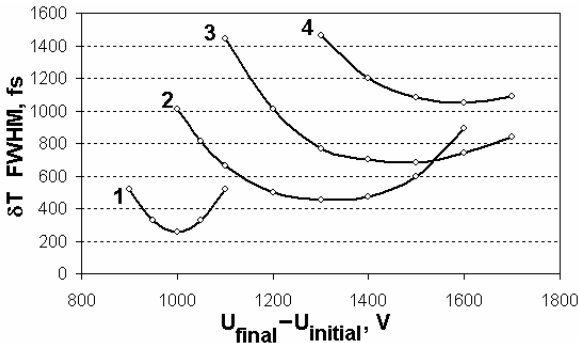


Fig. 3. Bunch temporal spread vs. the voltage ramp amplitude for different numbers N of electrons in the bunch: 1– no space charge taken into account, 2 – $N=1000$, 3 – $N=2000$, 4 – $N=3000$.

Briefly summarized, the main result of this work is as follows: the theoretical consideration and numerical simulation of Coulomb dynamics in ultrashort electron bunches for TRED experiments has shown that the effect of space-charge repulsion may be efficiently suppressed in the electron tubes with dynamic temporal compression using non-stationary electric fields.

References

- [1] V.A. Lobastov, R. Srinivasan, and A.H. Zewail. “Four-dimensional ultrafast electron microscopy” // Proc. Nat. Acad. Sci. USA, vol. 102 (2005), no. 20, pp. 7069 – 7073.
- [2] M.A. Monastyrskiy, S.V. Andreev, D.E. Greenfield, V.A. Tarasov, and M.Ya. Schelev // Proceedings SPIE, vol. 4948 (2003), pp. 305 – 310.
- [3] E. Fill, L. Veisz, Apolonski, and F. Krausz, “Femtosecond electron gun for diffraction experiments” // Proceedings SPIE, vol. 6194 (2006), #61940J.
- [4] S.V. Andreev, D.E. Greenfield, V.P. Degtyareva, M.A. Monastyrskiy, V.A. Tarasov, and M.Ya. Schelev // Proceedings SPIE, vol. 6636 (2007), #66360J.
- [5] J. Barnes and P. Hut. “A hierarchical $O(N \log N)$ force calculation algorithm” // Nature, 1986, vol. 324, pp. 446 – 449

A CONVERSION ELECTRON MÖSSBAUER SPECTROMETER FOR THE ANALYSIS OF MARS-ANALOGUE SAMPLES

M. Hahn and G. Klingelhöfer

Johannes Gutenberg-Universität, D-55128 Mainz (hahnmi@uni-mainz.de)

Introduction

Mössbauer Spectroscopy (MS) with a cobalt-57-source is a method to analyse the composition of surfaces and close-to-surface layers of iron-bearing samples.

After recoilfree emission and absorption of 14.4 keV gamma quanta, the excited nuclear state of the sample atoms can decay in several processes (see **Fig. 1**). With the detection of reemitted resonant electrons or gamma quanta, a Mössbauer spectrum is obtained. On the basis of the Mössbauer parameters, it is possible to distinguish between different oxidation states with a high accuracy.

The resonant gamma quanta (6.3 and 14.4 keV) originate from a sample depth of max 50 μm in iron and 130 μm (6.3 keV) / 500 μm (14.4 keV) in a basaltic composition [1], whereas resonant low energy electrons ($E < 15$ eV) have typically an escape depth of 2 to 4 nm [2]. That means, using Integrated Low Energy MS (ILEEMS), an excellent surface-sensitivity is given, while using gamma-ray MS one is able to look deeper into the sample. A combination of both methods can be applied if, for example, one is interested in depth-selective information about weathering processes of iron minerals.

The aim of the project

Our research group provided the miniaturised Mössbauer Spectrometer (MIMOS II) for both NASA Mars Exploration Rovers, which have now been operating on the martian surface for more than 4 years. We are collecting Mössbauer data from terrestrial Mars-analogue samples in order to compare them to the Mössbauer data received from Mars and to understand weathering processes that take part on Mars, either with or without the presence of water. This can give hints to the evolution of the earth-like planet Mars.

For analyses of the sample surfaces of Mars-analogue samples, a conversion electron Mössbauer spectrometer was developed in this work [3].

The state-of-the-art Conversion Electron Mössbauer Spectrometer

It is possible to operate the spectrometer either in low energy electron mode and be more surface sensitive (2 to 4 nm, ILEEMS) or to record the whole spectrum of emitted conversion electrons and analyse the sample in higher depths (200 to 300 nm [4], ICEMS).

Simulations have shown that low energy electrons emerge with large angles to the surface normal of the sample, whereas electrons of higher energies emerge more and more with smaller angles to the surface normal [5]. The angle between sample and electron detector (channeltron) in the experiment is variable, but was chosen to be 45° for test-measurements.

For the detection of low energy electrons, a bias voltage of 80V is applied to the channeltron. Former measurements have shown [6], that the quality of an integral spectrum can be improved by several factors of magnitude by applying a bias current. The low energy electrons account for more than 50 % of the integral electron spectrum [7].

Sample and detector are both placed inside a vacuum chamber (a pressure of less than 10^{-4} mbar is needed to operate the channeltron). A standart Mössbauer drive is used, operated with a frequency of 19 Hz.

It is possible to measure iron-bearing samples either as foils or as on-block-samples (size: 50 x 50 x 50 mm³ or less). The Count rate is app. 9000/min for ILEEMS and app. 1000/min for

ICEMS with a source intensity of 233 MBq. An integration time of 7 h (22 h) is required to obtain a signal-to-noise-ratio of 3% or better (for alpha-Fe foils, see **Fig. 3**).

References

- [1] Fleischer, I. et al. Journal for Geographic Research, (2008), in print
- [2] Klingelhöfer, G. and Kankleit, E.. Hyperfine Interactions, 57 (1990) pp 1905-1910
- [3] Michaela Hahn. Universität Mainz, Diplomarbeit 2007.
- [4] Vandenberghe, R.E. et al. Physica Mag. 20 (1998) 4 pp 339-353
- [5] Ralph Gellert. Technische Hochschule Darmstadt, Diplomarbeit 1994.
- [6] Sawicki, J.A. and Tyliszczak, T.. Nucl. Instr. and Meth., 80 (1970) pp 35-39
- [7] Zabinsky, J.S. and Tartachuk, B.J.. Nucl. Instr. and Meth., B31 (1983) pp 576-583

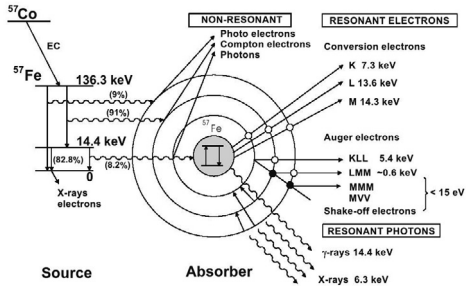


Figure 1: Scheme of various backscattering processes for Fe-57

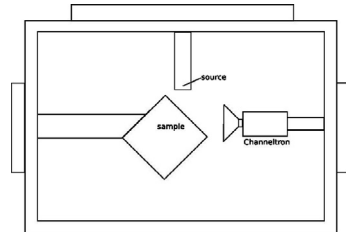


Figure 2: Scheme of the experimental assembly inside the vacuum-chamber

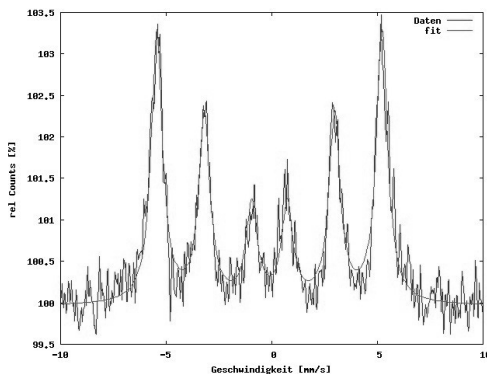


Figure 3:
ICEMS
Calibration
spectrum of an
alpha-Fe foil,
measuring time:
22.4 h

EXPERIMENTAL RESULTS FROM A MAGNETIC BEAM SEPARATOR SPECTROMETER IN THE SEM

Hung. Quang Hoang, Mans Osterberg, and Anjam Khursheed

National University of Singapore, 4 Engineering Drive 3, Singapore 117576.

Email: eleka@nus.edu.sg

Recently, a proposal to redesign the Scanning Electron Microscope (SEM) so that it can acquire high resolution images and perform parallel energy spectral analysis has been made based upon the use of a round magnetic sector beam separator [1, 2]. The magnetic sector beam separator is designed to deflect the primary beam, typically through 90° , while at the same time acting as the first stage of an energy spectrometer for scattered electrons. The plates of the magnetic sector are segmented and excited in such a way that it operates like a round lens, and its effective aberrations in the final image are predicted to be relatively small (well below 2nm). This was experimentally confirmed by using the round beam separator to deflect the primary beam of a conventional SEM through 90° and subsequently focusing it on to the specimen with a miniature transmission lens. Fig. 1 shows the high resolution from which the effect of the sector aberrations were deduced to lie well under 2 nm, see Ref [3] for more details. The purpose of this paper is to present the first experimental results for the beam separator acting as a spectrometer.

A schematic diagram of the experimental set up is shown in Fig. 2. A small beam separator/permanent magnet immersion lens attachment was designed to fit on to the specimen stage of a conventional SEM. A 5 kV SEM primary beam is deflected through 90° by the magnetic beam separator, and is focused on to the specimen by the add-on objective lens. The specimen is biased to around -3650V, yielding low landing energies (1350 eV). The scattered electrons subsequently travelling back through the lens are deflected by the beam separator and then energy filtered by an electrostatic mirror. In the original spectrometer proposal, a transfer lens working together with magnetic sector post-deflectors is proposed, however, due to the lack of space in the SEM chamber, an electrostatic mirror operating in retarding field mode is used in this preliminary setup, reflecting secondaries back through the beam separator for a second pass. The secondaries are collected by a PMT, while the backscattered electrons are transmitted through the mirror and not monitored in this experiment. The detected PMT current was monitored as a function of the mirror voltage V_M , effectively providing an integrated form of the secondary electron energy spectrum. The specimen voltage, V_S , is changed in one volt steps, and for each value of V_S , the PMT signal is curved fitted, normalized, and then differentiated in software form. The results are given in Fig. 3. The SE spectrum linearly changes as a function of specimen voltage, as expected. These preliminary results serve to demonstrate that spectral information of the scattered electron spectrum can be obtained through the use of a magnetic beam separator spectrometer.

References

- [1] A. Khursheed and M. Osterberg, Nucl. Instrum. And Meth. in Phys. Res. A **556** (2006) pp 437-444
- [2] A. Khursheed and H. Q. Hoang, Ultramicroscopy **108** (2008) pp 151-157.
- [3] M. Osterberg, PHD Thesis, National University of Singapore, 2006.

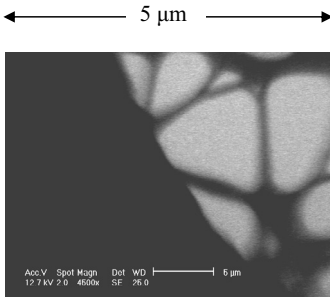


Figure 1 : High resolution transmission image of a lacey carbon specimen supported by a copper grid, captured at an image magnification of around 27,000 and a primary beam energy of 12.7 keV. A round magnetic sector beam separator unit was used to deflect the primary beam of a conventional SEM by 90° before it was focused on to the specimen by a permanent magnet transmission lens. The effect of sector beam aberrations on the image were deduced to be well below 2 nm [3].

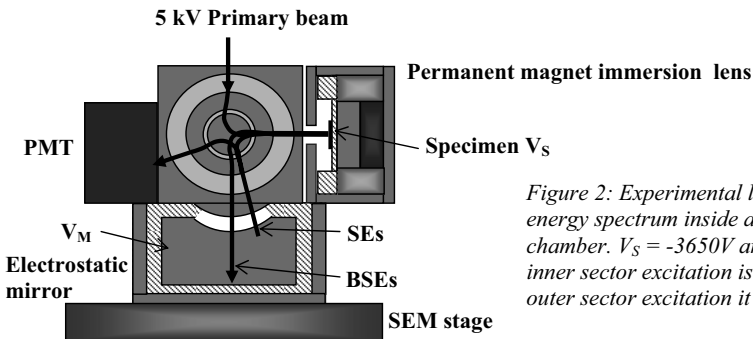


Figure 2: Experimental layout to acquire SE energy spectrum inside a conventional SEM chamber. $V_s = -3650V$ and the beam separator inner sector excitation is 70.5 AT, while for the outer sector excitation it is - 9 AT.

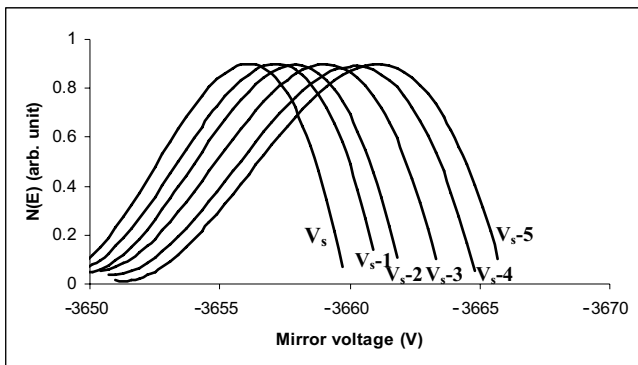


Figure 3: Experimental secondary electron spectra as a function of the specimen voltage varying in one volt steps. The PMT signal has been curve fitted, normalized and differentiated in software form.

WIEN FILTER ELECTRON OPTICAL CHARACTERISTICS DETERMINING USING SHADOW PROJECTION METHOD

M. Horáček, I. Vlček and M. Zobač

Institute of Scientific Instruments AS CR v.v.i., Královopolská 147, 61264 Brno,
Czech Republic
e-mail: mih@isibrno.cz

Wien filter is suitable for the separation of the primary and the signal electron beams in very low energy scanning electron microscope with cathode lens [1]. We have modified the *two-grid shadow method* [2] to determine experimentally electron optical properties (cardinal elements and aberrations) of the Wien filter, which is not a rotationally symmetric element. We call the modified method the *shadow method with grid and moving screen*. The advantage of the shadow method is its geometrical simplicity allowing the comparison of the experimentally obtained and numerically computed trajectories.

The arrangement of the *two-grid shadow method* is shown schematically in Figure 1(a). The electron beam from the point source passes through horizontally oriented linear grid, next the beam passes through the measured optical element, makes an image of the source, passes through a vertically oriented second linear grid, and casts a shadow upon a fluorescent screen. The inclination tangent of input trajectories can be determined from the point source position and from the known dimension of the first grid. The inclination tangent of the output trajectory can be determined from the shadow image of the first grid and the distance between the screen and the intersection of the trajectory with the optical axis. This distance can be determined from the second grid and its shadow image. Angular magnification can be calculated from these trajectories. Hence, with knowledge of potentials in image and object planes, we can calculate linear magnification. Two measurements at two different geometrical configurations are necessary to calculate the remaining cardinal elements, i.e. the positions of principal planes and focal distances [3]. The calculation of angular magnification from shadow image of two grids is possible only for rotationally symmetric element. Therefore, our modification of the *two-grid shadow method* is necessary to measure electron optical elements without rotational symmetry.

The arrangement of the modified *shadow method with grid and moving screen* is shown in Figure 1(b). The rectangular grid situated in front of the measured Wien filter (outside the filter fields) together with the point source position fully determines the input trajectories. Output trajectories can be determined from the two shadow images taken at two fluorescent screen positions. The advantage of the method remains the use of the grid as a scale, thanks to this the coordinates of the characteristic points are sufficiently precisely determined before the measurement. The grids can be used to calibrate distances on the screen. Additionally, the information about transverse coordinates of the trajectories is contained in one image, so image processing methods can be used to read the coordinates of the characteristic points from the image. Only the determination of the screen position is important.

All the types of aberrations will manifest in the shadow image: geometrical, chromatic, and diffractive, as well as blurring due to finite dimension of the point source. The method is based on reading the coordinates of the characteristic points from the shadow image. The edge blurring caused by the chromatic and diffractive aberrations and the finite dimension of the point source makes the precise reading of the points coordinates difficult. Therefore, deviations in the image caused by the above mentioned aberrations have to be minimized and the deviations in the image caused by the geometrical aberrations have to be maximized. Simultaneously the aberrations must be large enough to be measured. The calculation of the

aberration coefficients will be made by fitting of the measured trajectory using the least squares method. The method can be also used for calculation of chromatic aberrations coefficients if the measurements for different electron energies would be made.

The experimental UHV apparatus for measurement of our Wien filter properties have been designed and made. The Wien filter uses eight combined poles-electrodes to produce nearly identical magnetic and electrical field. Schottky thermal field cathode is used as a point source of electrons.

- [1] I. Vlček, B. Lencová, M. Horáček in “Proc. of the 13th EMC” (Antwerp, 2004) Vol. I, p.337
- [2] K. Spangenberg and L.M. Field, *Electrical Communications* **20** (1942), p. 305.
- [3] L.A. Baranova and S.YA. Yavor in “Advances in Electronics and Electron Physics”, ed. P.W. Hawkes (Academic Press, Boston) (1989), p. 1.
- [4] Supported by Grant Agency of the Academy of Sciences of the Czech Republic, grant no. IAA100650803 and Academy of Sciences of the Czech Republic, grant no. AV0Z20650511.

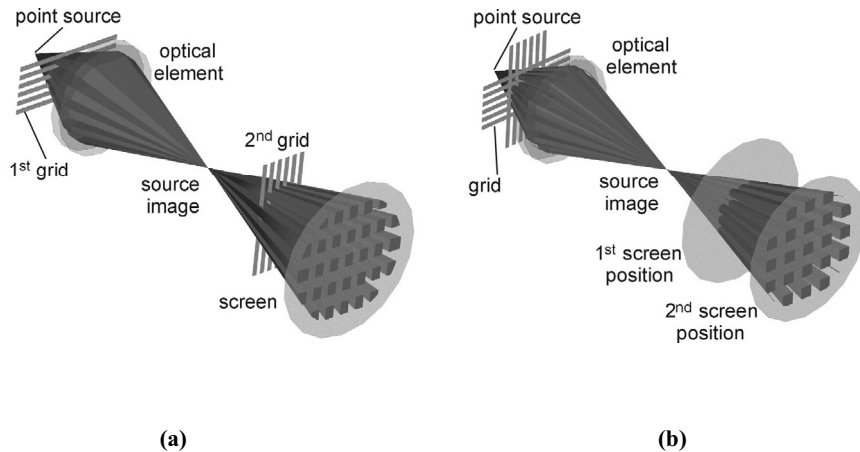


Figure 1. (a) The arrangement of the two-grid shadow method. (b) The arrangement of the modified shadow method with grid and moving screen.

SCANNING LOW ENERGY ELECTRON MICROSCOPY OF DOPED SILICON AT UNITS OF eV

M. Hovorka*, Š. Mikmeková, L. Frank

Institute of Scientific Instruments AS CR, v.v.i., CZ-612 64 Brno, Czech Republic

*e-mail address: hovorka@isibrno.cz

Very low energy electron microscopy with the primary beam of hundreds of eV has proven very useful when imaging doped areas in semiconductors at high lateral resolution and high sensitivity to the dopant concentration. We employed the scanning low energy electron microscope equipped with the cathode lens in imaging the doped silicon samples at the landing energy of few eV only.

Dynamic effects owing to the charge injected in small p-type patterns (10^{17} to 10^{19} cm^{-3}) were observed (see Figs. 1 and 2). Electron dose and size of the doped patterns are the parameters, which determine the rate of negative charging induced by the primary beam. Negatively charged areas decrease kinetic energy of incident electrons down to nearly total reflection of the beam toward or off the detector (Fig. 1), causing a strong contrast between doped areas even at light doping that exhibits only poor contrast at 1 keV. High image contrast of the doped structures, obtained in this way, is free of radiation damage and enables one to study charging effects at high lateral resolution [1].

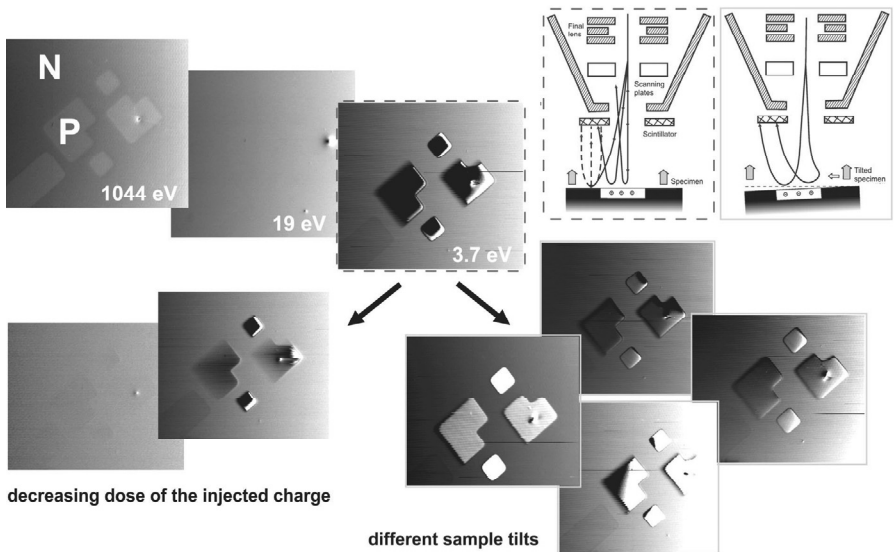


Fig. 1: Dependence of the contrast between strongly charged p-type patterns (doped to 10^{18} cm^{-3}) and lightly doped n-type substrate on electron dose and specimen tilt at units of eV of the landing energy of electrons. The size of patterns and the electron dose govern the contrast – see the bottom left corner. When tilting the sample we detect a part of the signal previously escaping through the central bore of the detector – see the bottom right corner and schematic view of the experimental setup for both not tilted and tilted sample in the upper right corner.

Below 20 eV strong elastic backscattering of electrons takes place and variations in the local density of states induced by doping demonstrate themselves as electron energy variations in the reflectivity [2]. Large p-type areas on a lightly doped n-type substrate exhibit some contrast at 1 keV, which gradually decreases to zero when lowering the landing energy. At few eV a strong contrast, attributed to the modulated reflectivity, reappears with the opposite sign (see Fig. 2 for 2.2 eV and the region B in Fig. 3).

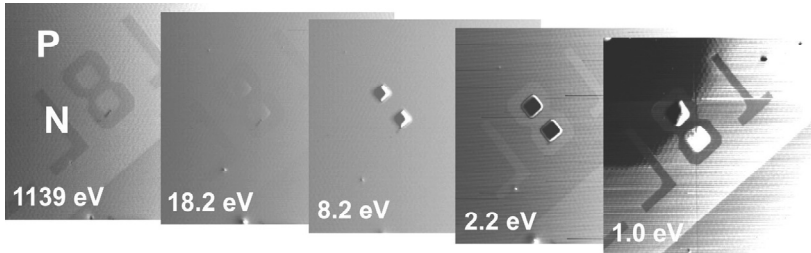


Fig. 2: Contrast evolution between p- and n-type areas when decreasing the landing energy of the primary beam. Notice the charging of small p-type islands and inversion of the contrast at 2.2 and 1.0 eV.

When the sample surface is contaminated with hydrocarbons, the primary beam decomposes them forming a graphitic layer and hence some subsurface metal-semiconductor junction [3]. When approaching the total reflection conditions at few eV, we encountered dynamical behaviour probably connected with the graphitic contamination layer. Contrast of the doped areas, now obviously uncharged ones, inverts its sign once more and becomes very strongly pronounced (see Fig. 2 for 1.0 eV and the region A in Fig. 3).

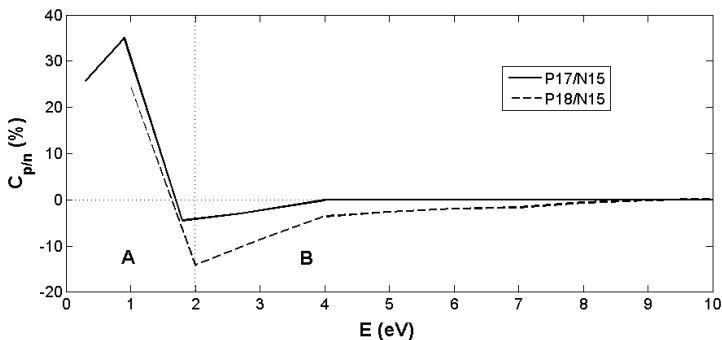


Fig. 3: Contrast $C_{p/n}$ between large p-type areas and the n-type substrate as a function of the landing energy E of primary beam - for more details see the text.

References

- [1] Frank L., Müllerová I. (2005) *Ultramicroscopy* 106, 28-36.
- [2] Müllerová I., Frank L., Hutař O. (2001) *Scanning* 23, 115.
- [3] El-Gomati, M. M. et al (2005) *Surf. Interface Anal.* 37, 901-911.
- [4] The study is supported by the Grant Agency of AS CR under grant no. IAA100650803.

NUMERICAL SIMULATIONS OF THERMIONIC ELECTRON GUNS

P. Jánký, B. Lencová and J. Zlámal*

Institute of Scientific Instruments of the ASCR, v.v.i., Královopolská 147, 612 64 Brno,
Czech Republic
E-mail: jansky@isibrno.cz

* Institute of Physical Engineering, Faculty of Mechanical Engineering, Brno University of
Technology, Technická 2, 616 96 Brno, Czech Republic

Thermionic triode electron guns with directly heated cathode are still in wide use for their low requirements on operation conditions, high emitted currents and low service costs. In ISI Brno we started with simulations of thermionic electron guns for electron beam welding machine [1] used also for experiments with electron beam micromachining. Numerical simulations enable us to understand the space charge effects and it can help us to improve the geometry of gun electrodes.

For simulations we use the program EOD (Electron Optical Design) [2]. Computation of potential is based on accurate finite element method in large meshes. Space charge distribution is set from tracing test particles and the potential is iteratively improved. From the field intensity near the cathode surface we determine a new estimation of the emission current limited by space charge. After each change of emission current the space charge distribution must be recalculated and emission current estimation improved as well as the area of the emitting region on cathode. If the space charge effect is significant, the area of this region depends not only on Wehnelt bias but also on the emitted current.

Fig. 1 shows a simulation of thermionic electron gun with planar cathode intended for experiments with micromachining. Accelerating voltage is 50 kV. Emitted beam is calculated as space charge limited, for Wehnelt bias 1050 V the beam current is 3.4 mA. Fig. 2 shows profiles of current density in 3 different planes.

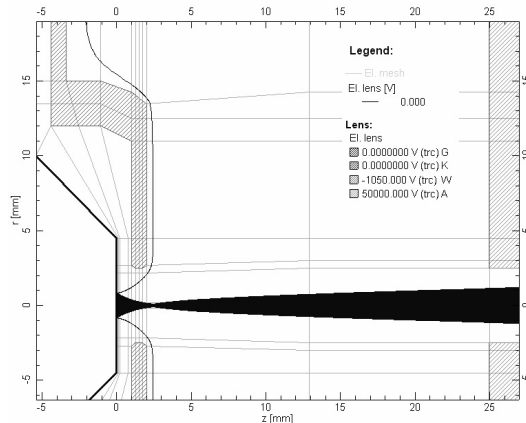


Figure 1: Simulation of the thermionic electron gun with planar cathode. Accelerating voltage is 50 kV. Beam was simulated as monochromatic with starting energy close to 0 eV. For Wehnelt bias 1050 V the beam current is 3.4 mA.

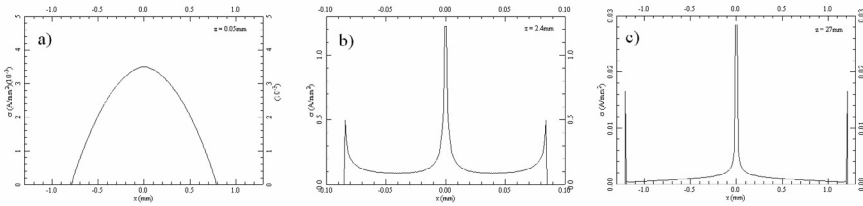


Figure 2: Beam profiles at three different planes: a) near the cathode surface at $z=0.05\text{mm}$, b) at the plane $z=2.4\text{mm}$ and c) at the plane $z=27\text{mm}$.

Figure 3 shows one of the calculated electron guns for electron microscopy. Its geometry and beam properties are described in [3]. Electron gun is simulated as rotationally symmetric problem, the cathode is simulated as a cylinder with a spherical cap. For accelerating voltage 10 kV and Wehnelt bias -121 V the calculated emission current is 93 μA .

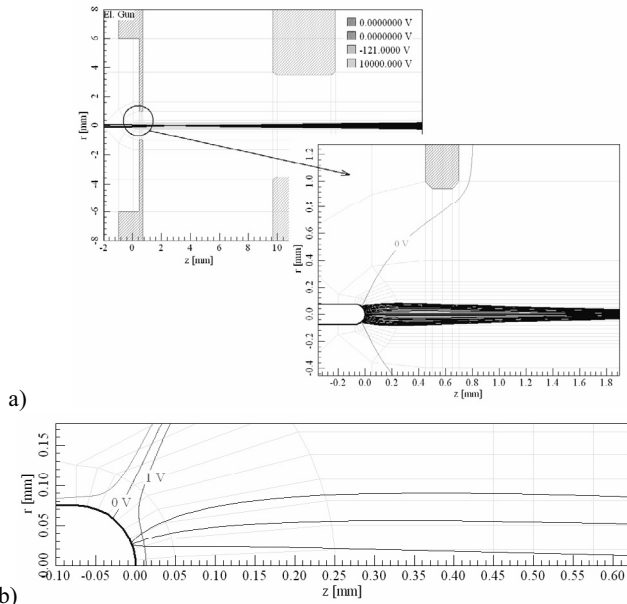


Figure 3: a) Simulation of the thermionic electron gun. From the heated cathode approximated by a cylinder with a spherical cap the electron beam is emitted. The beam energy is 10 kV, Wehnelt bias -121 V. b) A pencil of rays near the cathode for beam energy 0.24 eV. Equipotential lines -1 V, 0 V and 1 V are shown.

- [1] J. Dupák, I. Vlček, M. Zobač, Vacuum 62, 159-164, 2001.
- [2] B. Lencová and J. Zlámal, Microsc. Microanal. 13, Suppl 3 (2007), p. 2
- [3] R. Lauer in "Advances in Optical and Electron Microscopy Vol. 8" ed. R. Barer and V. E. Cosslett, (Academic Press Inc, 1982).
- [4] This work was supported by Grant Agency of AS CR, grant no. IAA100650805 and AV0Z20650511.

SETTING UP A PICOSECOND ELECTRON SOURCE BY COMPRESSING PULSES OF A PHOTO EMISSION CATHODE

R.Janzen*, G. Schönhense

Johannes Gutenberg-Universität, Institut für Physik, D-55099 Mainz, Germany

* Janzen Consulting, Ludwigstr. 3, D-64653 Lorsch, Germany

e-mail address: info@dr-janzen.de

In order to investigate dynamic phenomena various exciting sources with excellent time structures are used. Whereas optical pulses are widely available and used, electron optical devices in material science mainly focus attention to continuous beam applications. We intend to transfer the principle of phase focusing that is well known in accelerators (e. g. [1]) to an electron source in order to build up a picosecond pulse electron probe for future material science applications.

The idea of phase focusing is the compression of an initial electron pulse (by a factor of 10 or 20) using dynamic fields in order to decelerate the early electrons at the front of the pulse and accelerate the late ones. During a drift space the late electrons then approach the early ones. If there was no energy spread within the initial pulse, all electrons would reach the end of the drift space at the same time, which is denoted by time focus or longitudinal focus. Of course real electron pulses have an energy spread which disturbs the phase focus mechanism transforming itself into a time structure. This kills any effort to remove the energy modulation used for phase focusing (just before the pulse reaches its time focus). Thus the mechanism of phase focusing transforms the initial time structure into an energy spread and vice versa. The product of both, that is the pulse length times the energy spread remains constant by virtue of Liouville's law.

In order to create the initial pulse we will combine a GaAs photo emitter with a pulsed laser. Though GaAs requires crucial UHV conditions we decided for it because there is experimental experience with that kind of photo emitters in our group that we can rely on. Well why not generating the picosecond pulse directly using that technique? The main reason is that such short pulses expand very fast, whereas the minimum length of compressed pulses can (and should) be reached at the sample. In addition the length of the non compressed pulse could solely be influenced by varying the potential and the distance between the photo emitter and the sample.

So far the physical context is straight forward. Now let's ask what power is needed in order to do the phase focusing. We have to take into account that the duration of stay of the electrons inside the dynamic field is usually longer than the period of oscillation of the field and strongly depends on the acceleration (or deceleration) that the electrons experience inside the field. The best and easiest way to do so nowadays

is solving the equation of motion numerically. The result can be seen in figure (1) where the power needed for compressing a pulse of 20 ps initial length by a factor of 20 is shown as a function of the drift length which is the distance between the resonator and time focal point.

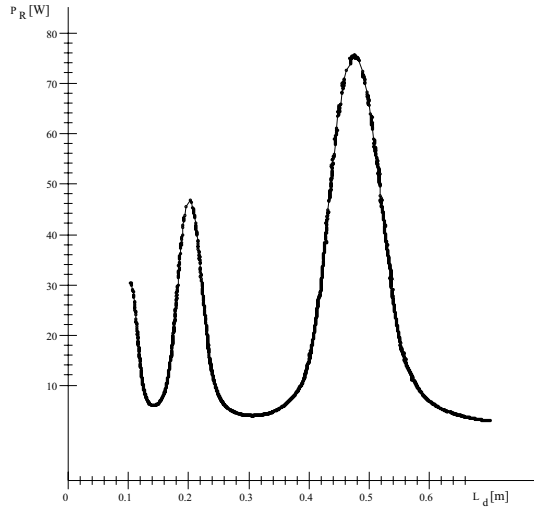


Figure 1: Power necessary for compressing a pulse of 20 ps length by a factor of 20 as a function of the drift length. The resonator's height was arbitrarily chosen to be 6 cm, its quality factor was assumed to be $Q = 1000$ and the frequency of the field was chosen to be $\nu = 2.5$ GHz.

Of course one has to take advantage of resonance effects. In the calculation leading to figure (1) the cylindrical resonator's height was chosen to be about half the wavelength. This is an arbitrary choice, as long as the desired TM_{010} -mode of a cylindrical resonator is used. The quality factor of the resonator was assumed to be $Q = 1000$. The maxima of the curve in figure (1) match the condition that the duration of stay of the electrons inside the resonator is n times the oscillation time of the wave, where n is an integer. This means that accelerating and decelerating forces nearly cancel out.

What are we intending to do after having successfully compressed an electron pulse? First we have to build a transfer optics that allows us to focus the beam onto the sample

such that the lateral focus and the longitudinal focus coincide. If we are ambitious to build a small electron probe we have to pay attention to space charge effects: Even 100 electrons per pulse (that we aim for) cause an average normalised beam current κ of about $\kappa = 0.3$, where κ is calculated by $\kappa = 3790 * \frac{I}{\alpha^2 * U^{1.5}}$ (see [2] for details). In this estimation the acceleration potential was set to $U = 5$ kV and the opening angle α was approximated by the ratio of the radius of the emission area of about $150 \mu\text{m}$ and the drift length of about 0.5 m. An average pulse length of 10 ps leads to a beam current I of approximately $2 \mu\text{A}$. As shown in [2] values of $\kappa > 0.01$ lead to irreversible beam broadening due to space charge effects.

In the meantime we intend to apply the pulse for a time-resolved investigation of high-frequency modes of ferromagnetic particles. These modes lie in the GHz range and can be tuned to a certain extent by choosing the proper material, size and thickness of the thin-film structures. Their excitation spectrum is well known from ferromagnetic resonance work, i.e. observation in the frequency domain. We will observe such modes in the time domain by driving the eigenmode with the same master oscillator as the source and pulse compressor. By varying the phase shift between the driving signal and the electron pulse, a stroboscopic mode of observation is possible. The magnetic response of the particle (i.e. the precessional motion of the magnetisation vector) will be measured via the spin polarisation of the secondary electrons (parallel imaging SEMPA).

References

- [1] V.I. Shvedunov, M.-O. Ihm, H. Euteneuer, K.-H. Kaiser, Th. Weis. Design of a prebuncher for Increased Longitudinal Capture Efficiency of MAMI. Proc. of the 1996 European Particle Accelerator Conference, Barcelona, 10.6. - 14.6.96, p. 1556
- [2] Rainer Spehr. Broadening of charged particle microprobes by stochastic Coulomb interactions. *Optik* 70, No. 3 (1985) 109-114

A SECOND-ORDER FOCUSING TOROIDAL SPECTROMETER

Anjam Khursheed

National University of Singapore, 4 Engineering Drive 3, Singapore 117576.

Email: eleka@nus.edu.sg

At present, toroidal energy spectrometers that are designed to collect electrons/ions over 2π radian emission angles in the azimuthal direction have first-order focusing properties [1,2]. The following work presents a second-order focusing toroidal spectrometer design, one which is based upon obtaining an intermediate focus in the r-z plane, this allows for second-order spherical aberration contributions accumulated before and after the intermediate focus to cancel. A range of different geometrical designs were investigated, the best of which have the following simulated predictions: second-order focusing with an expected energy resolution of 0.146% for acceptance angles between $\pm 6^\circ$, comparable to the theoretically best resolution-transmittance performance of the Cylindrical Mirror Analyzer (CMA) [3]; parallel energy acquisition where the increase in energy resolution with respect to the band centre rises by less than a factor of 2 for energies that lie within $\pm 4\%$ of the pass energy; a maximum input angular spread of $\pm 10^\circ$ and a maximum parallel energy band width of $\pm 15\%$ (30% total) of the pass energy; retarding/accelerating field mode of operation without the need to incorporate auxiliary lenses; and depending on the precise application, no working distance limitations.

Fig. 1 depicts simulated trajectory paths through the toroidal spectrometer for different emission angles. The central ray enters the spectrometer at an angle of 45° with respect to the horizontal axis. For parallel energy detection, the detection plane lies on the surface of a shallow cone whose slanting side makes an angle of around 26.4° with respect to the horizontal, as shown in Fig. 2. The conical detection plane can be well approximated by an array of multi-channel flat strip detectors in the azimuthal direction, without incurring any significant degradation to the energy resolution. For low energy electrons, typically less than 50 eV, electrons can be mirrored on to a flat plate detector located below the specimen after they pass through the spectrometer. The energy resolution is only marginally degraded by doing this, predicted to be 0.196% at the centre pass band energy for an input angular spread of $\pm 6^\circ$.

References

- [1] C. Miron, M. Simon, N. Leciercq and P. Morin, *Rev. Sci. Instrum.*, **68** (10), 3728-3737 (1997).
- [2] E. I. Rau, A. Khursheed, A. V. Gostev, and M. Osterberg, *Rev. of Sci. Instrum.*, **73**, No. 1, 227-229 (2002)
- [3] H. Z. Sar-El, *Rev. of Sci. Instrum.*, **41**, No. 4, 561-564 (1970).

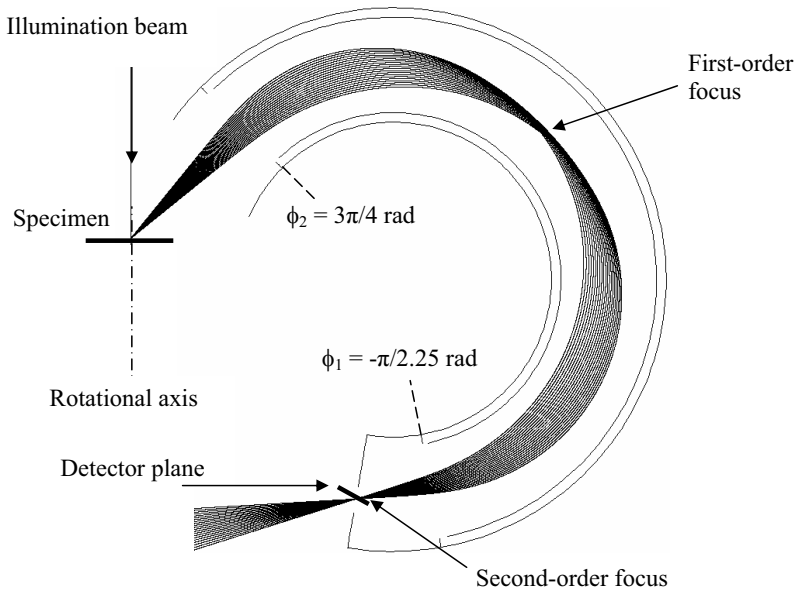


Figure 1: Simulated ray paths of electrons through the spectrometer at the pass energy for a wide variety of entrance angles. The central ray enters in at 45° and 21 trajectories are plot over uniform steps for an input angular spread varying from -104 mrad to $+104$ mrad (-6° to 6°).

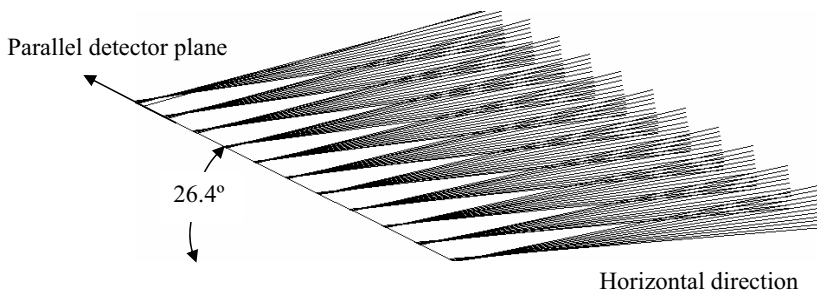


Figure 2: Simulated trajectories around the output focal plane for 11 emission energies ranging from 95% to 105% of the pass energy and 11 input angles from -52 mrad to 52 mrad around the central ray in uniform steps.

VARIABLE MAGNETIC SECTOR FIELD ELECTRON SPECTROMETERS FOR PARALLEL ENERGY ACQUISITION

Anjam Khursheed, Hung. Q. Hoang and Saravanan K. Musuwathi

National University of Singapore, 4 Engineering Drive 3, Singapore 117576.

Email: eleka@nus.edu.sg

Significant improvements to Auger Electron Spectroscopy (AES) and Electron Energy Loss Spectroscopy (EELS) depend on finding better electron energy spectrometer designs. In particular, data-acquisition times of such techniques can be considerably shortened from the use of parallel energy spectrometers that capture spectral information simultaneously over a scattered energy range that spans several orders of magnitude. Recently, two such spectrometers have been proposed in the context of AES, and both are electrostatic in nature [1, 2]. This proposal presents a magnetic sector spectrometer alternative, one which promises to be more compact than previous designs, giving rise to the possibility of developing a parallel energy spectrometer array.

The present design is based upon the concept of using an array of permanent magnets (or electromagnets) to create a deflection field whose strength varies along the length of a simple sector magnet. The strengths of the magnets are selected so that they create an asymmetric Gaussian-like field distribution. An extended two dimensional finite element program is used to calculate the required three dimensional magnetic scalar potential distribution [3]. Simulation results predict that this kind of field distribution is able to disperse and focus scattered electrons on to a straight-edged detector lying in the plane of deflection (x - y) for emission energies that vary by more than an order of magnitude, as shown in Fig. 1. Two identical sector boxes are used, box 1 for secondary and low energy Auger electrons (0.5 – 1 keV) and box 2 for higher energy Auger and backscattered electrons (1 – 20 keV). The sector excitation strengths within each box can be appropriately adjusted in order to detect the energy range of interest.

Since the spectrometer dimensions are relatively small, measuring only 34 mm by 15 mm with a plate separation distance of 8 mm in the z direction, a large array of such spectrometers placed around the point of emission in the azimuthal and polar angular directions should in principle be possible. They can be placed within an existing SEM as add-on units, providing quantitative spectral information in addition to the topographical information obtained by the SEM's existing SE and BSE detectors.

References

- [1] M. Jacka, M. Kirk, M. El Gommati and M. Prutton, *Rev. Sci. Instrum* **70**, 2282 (1999)
- [2] F. H. Read, *Review of Scientific Instrum.*, **73**, No. 3, pp 1129-1139 (2002)
- [3] Hung Quang Hoang and Anjam Khursheed, to be published in the proceedings of CPO-7 *Nucl. Instrum. Meth. in Phys.Res. A*.

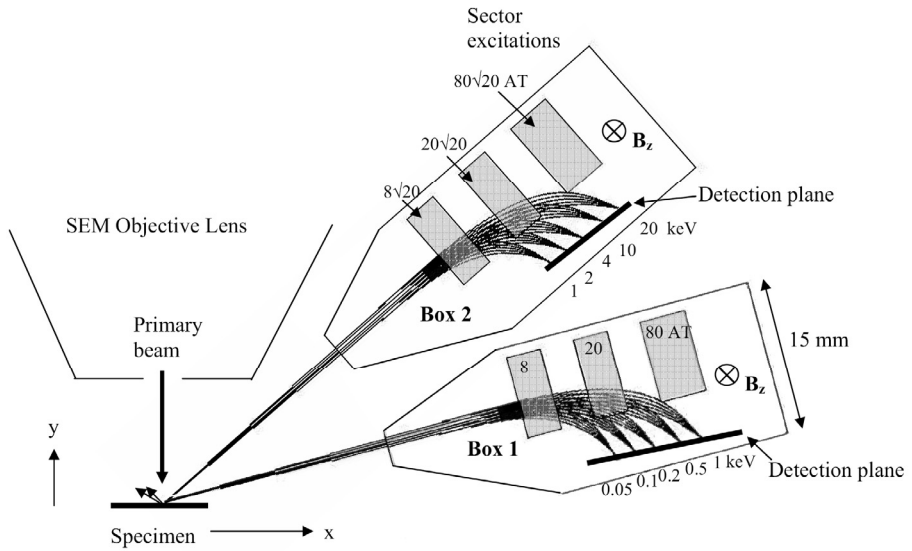


Fig 1: Simulated in-plane (x - y) electron trajectory paths through variable field magnetic sector spectrometers for the energies of 0.05, 0.1, 0.3, 0.5, 1 keV (box1) and 1, 2, 4, 10 and 20 keV (box2) with the emission angles ranging from 0 to ± 20 mrad in steps of 10 mrad. The plate separation distance in the z direction is 8 mm.

SIGNAL COLLECTION WITH SECONDARY ELECTRON DETECTORS IN SEM

I. Konvalina, M. Hovorka, M. Dvořáková and I. Müllerová

Institute of Scientific Instruments, Academy of Sciences of the Czech Republic, v.v.i.,
Královopolská 147, 612 64 Brno, Czech Republic

E-mail: konvalina@isibrno.cz

The standard method of the secondary electron (SE) detection in the scanning electron microscope (SEM) is to use the Everhart Thornley (ET) detector [1]. ET detector is used for collection of signal electrons in microscopes, where the specimen region is free of magnetic field, but also in arrangements with magnetic field in the specimen vicinity. For both cases this paper examines the trajectories of SE with regard to their energy and angular distributions.

The ET detector with a weak electrostatic field used to attract low energy SE is called here the “standard” system. Modern SEMs achieve their improved image resolution by allowing the strong magnetic field of the objective lens (OL) to penetrate to the specimen surface (the “immersion” system). Two SE detectors are usually used in this case: one is below the OL just as the standard ET detector (the “lower” detector) and the other is positioned above the OL (the “upper” detector) (see Figure 1). Calculated distributions of the axial magnetic field [2] are shown in Figure 2.

The final contrast of SE images for a particular specimen varies with the energy and angular sensitivity of the detectors collection, connected with specific distributions of electrostatic and magnetic fields in the specimen region. In order to interpret the observed contrast properly, it is necessary to study in detail the collection efficiency of individual detectors [3,4].

Three above-mentioned detection systems have been simulated in order to determine which part of the emitted SEs is collected. The collection efficiency was calculated for the SE energies of 1, 2, 3, 5, 10 and 20 eV and the primary beam energy of 1 keV for which only weak magnetic field in the specimen region is sufficient to focus the probe. One example of the calculated collection efficiency for the whole energy spectrum of SE is in Figure 3. Obviously, the collection efficiency of the standard detector is much smaller than that of the in-lens detector but the difference diminishes with increasing working distance.

In order to be able to verify the simulated data, the arrangements were chosen identical to geometries of microscopes used for experiments. However, the upper detector was not accessible to measurement of its geometry and no construction drawing was available. In this situation, we assumed that the in-lens detection system was designed to very high effectiveness so that all SEs entering the OL are deflected toward scintillator of the upper detector. Hence the collection efficiency of the upper detector was estimated according to penetration of SE through the OL.

Each of the three above-described detectors prefers a specific range of polar angles of the SE emission. The upper detector is capable of collecting SEs in the full azimuthal angle for any polar angle while the standard detector collects in the azimuthal direction not more than about 150 degrees.

For verification of the simulated data we used the standard resolution-testing specimen with Au particles on a carbon substrate. Figure 4 shows micrographs taken by the three detector systems for the primary beam energy 1 keV. In order to aid identification of the signal electrons detected, we excluded SE I and SE II from the detected signal by positive biasing

(+50 V) the specimen (see Figures 4, right column). Then both the “upper” and “standard” detectors exhibit a strong decrease in signal, unlike the lower detector the signal of which is significantly contributed by SE III released by backscattered electrons (BSE) that bombard OL and other surfaces. This fact explains the zero simulated efficiency of the lower detector. Contrasts of the micrographs for the primary beam energy 1 keV correspond with BSE and SE yields measured by Zadražil and El-Gomati [5] (see Figure 5). The software packages EOD [2] and SIMION 3D [6] were used in all simulations.

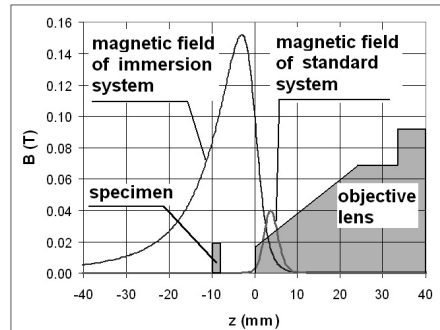
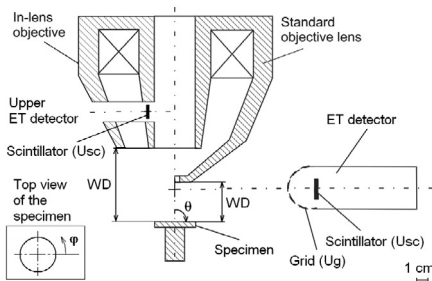


Figure 1 Geometrical arrangement used for simulations; left half-plane of the OL shows geometry of the immersion system and the right-half plane shows the standard system.

Figure 2 Axial magnetic fields of immersion and standard systems.

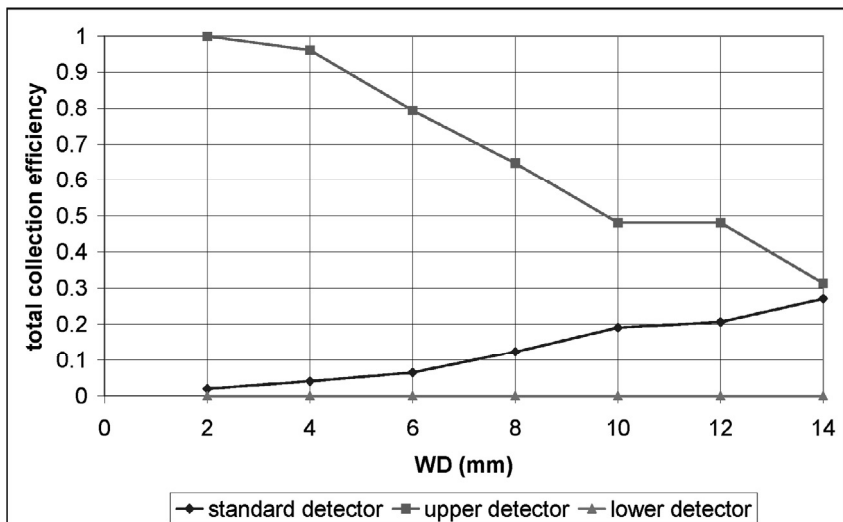


Figure 3 Example of calculated total collection efficiencies of the “standard” and “lower” detector and the estimated collection efficiency of the “upper” detector as a function of the working distance; $E_p = 1$ keV, complete energy spectrum of SE.

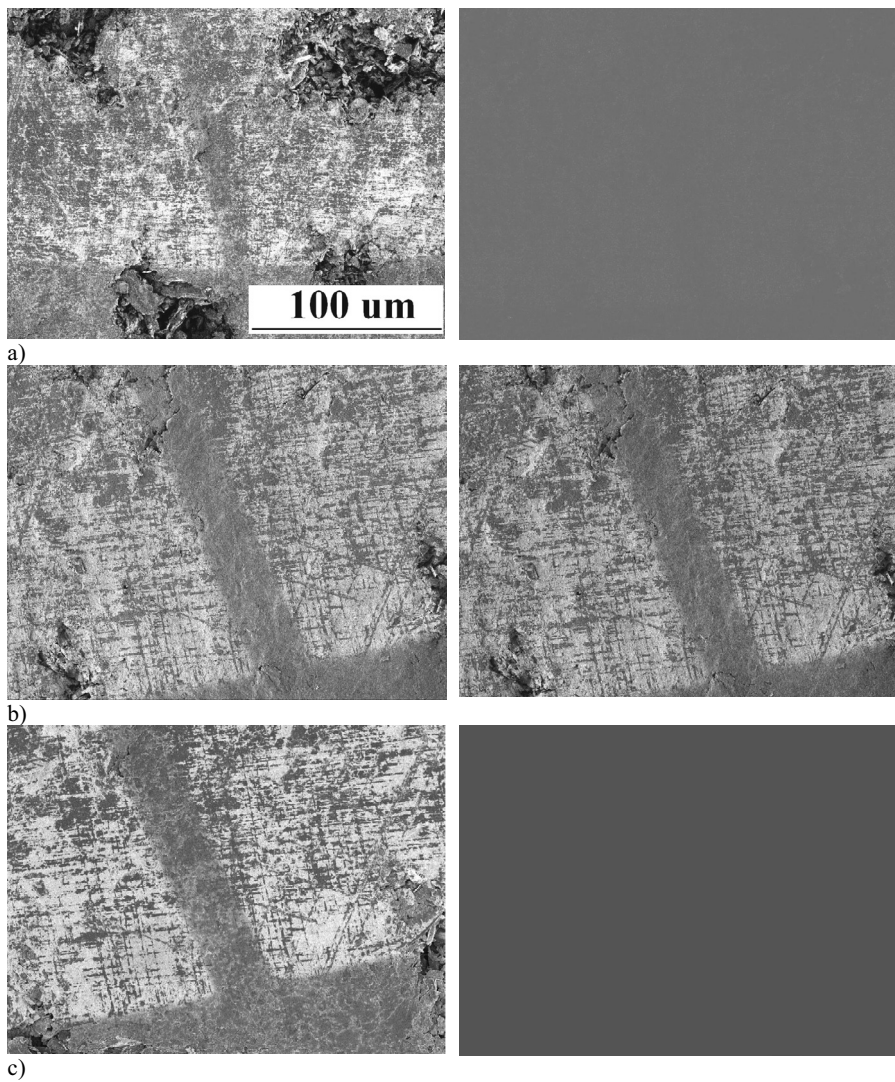


Figure 4 Micrographs of the standard resolution-testing specimen with Au particles on a carbon substrate, taken by the standard (a), lower (b) and upper (c) detectors; $E_p = 1$ keV, $WD = 8$ mm, $U_{spec} = 0$ V (left column), $U_{spec} = +50$ V (right column)

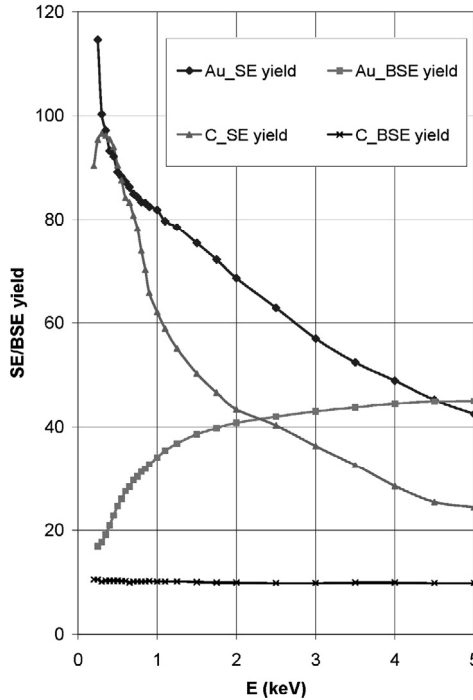


Figure 5 Comparison of the SE and BSE yields from the gold and carbon targets for normal impact of primary electrons (measured by Zdražil and El-Gomati, see [5]).

References:

- [1] Everhart T.E. and Thornley R.F.M., 1960, J. Sci. Instrum. 37, 246-248.
- [2] Lencová B. and Zlámál J., 2007, Microscopy and Microanalysis 13, 2-3.
- [3] Cazaux J., 2004, Journal of Microscopy 217, 16-35.
- [4] Konvalina I. and Müllerová I., 2006, Scanning 28, 245-256.
- [5] Müllerová I. and Frank L., 2003, Advances in Imaging and Electron Physics 128, 309-443.
- [6] Dahl D. A., 2000, Int. J. Mass Spectrom. 200, 3-25.
- [7] This work is supported by the Grant Agency of AS CR under grant no. KJB 200650602.

SOLVING COMPLEX ELECTRON OPTICAL PROBLEMS WITH EOD

B. Lencová

Institute of Scientific Instruments, AS CR, Královopolská 147, 612 64 Brno, Czech Republic,
e-mail: bohunka@isibrno.cz

1. Introduction

The computations in particle optics require accurate determination of 2D electrostatic and magnetic focusing, deflection and multipole fields and accurate evaluation of optical properties from aberration theory or from ray tracing. The EOD program allows these types of computations. Moreover, it is a complete workplace equipped with user interfaces for all these tasks, graphical outputs and processing [1,2]. From the user point of view it is important to have simple and easy-to-use tools for the data input and output that are smoothly working under Windows XP. This was one of the basic aims behind the development of EOD.

2. First order finite element method

The most suitable method to cover the computations of all these required fields is the finite element method (FEM). Saturated magnetic lenses represent a very important class of electron optical problems, and the FEM is the only method that can analyze them successfully. Our experience has shown that all requirements are fulfilled with the first order finite element method, supposing that the program uses proper algorithm to set up the coefficients of FOFEM equations, a sufficiently large number of mesh points and a mesh with graded mesh step. All the older FOFEM packages were implemented in EOD as dll modules. Already the accuracy comparison of CDM, FDM and FEM in 1998 made it clear that even on electrostatic problems we get proper results [3].

The user has to overcome certain barrier, namely the basic philosophy behind the input of the geometry with a topologically regular coarse mesh made of horizontal and vertical mesh lines and subdivision into quadrilaterals. On the other hand, the simple topology makes the computation faster and easier, and as a rule much more accurate than the "standard" FEM with triangular meshes. EOD allows the coarse mesh with practically unlimited number of coarse mesh lines, and this allows input of a complete microscope geometry into a single computation. Moreover, the fine mesh with graded mesh step is automatically generated from one or more "gaps" containing user given number of fine mesh lines. Again, the number of fine mesh points can be very large.

With ever increasing computation speed of personal computers a typical computation in $\frac{3}{4}$ million points is around a minute for the field computation, and the attention naturally shifted from the field problems to ray tracing. However, the immediate implication of the high accuracy of the available field is an improvement of the possibilities for ray tracing, limited before by the inaccuracies at 2D interpolation.

3. Optics and ray tracing

Standard procedure in particle optics is the use of paraxial imaging and aberration theory. For geometrical aberrations this starts with developing the third order geometrical aberration theory, implemented in EOD for any combination of lenses and deflectors. The next step is the fifth order aberrations, for which no complete set of aberration integrals was published! Moreover, differential algebra starts to be popular, because no explicit expression of integrals is needed and the prerequisite, the accuracy of higher order field derivatives, is never discussed in detail. Axial potential or field is interpolated in EOD with cubic or quintic spline

and the 4th-5th order variable-step Runge-Kutta procedures is applied for paraxial trajectories and aberrations.

Ray tracing is another story. One of the biggest obstacles is the need to understand well the 2D interpolation in FEM meshes by the slice method (abandoned in EOD) or ZRP [4] method, used with success before. Ray tracing solves the particle equation of motion in any combination of focusing and deflection fields, even the fields of higher multipole elements (quadrupoles, sextupoles and octupoles) can be used with any of the interpolation methods. The problem is to use efficiently the large amount of output provided by ray tracing. In large smooth meshes the accuracy of the ray tracing results can be very high, so that we can easily and correctly derive from the final positions the geometrical aberration coefficients of the 5th order and the chromatic aberrations of the 4th rank, demonstrated already in 1996 on this seminar on the example of electron mirror [5]. In EOD the ray tracing has been programmed anew and the ZRP method was complemented with bicubic, biquintic and B-splines for 2D interpolation. The variable-step 7th-8th order Runge-Kutta-Fehlberg method is again used.

4. EOD examples

In electron optics we lack suitable data to be used for comparison. If realistic geometries are used, then they are not described properly. Typical complex electrostatic problems are the cathode lenses and the electron mirrors. At CPO7 we gave the analysis of a cathode lens of a LEEM lens we published in 1998 [6]. The mirror is even more complex, see [7]. In 1996 we used the dipole mirror as a test example [5], and it is also used as one example in CPO-2D of Read [8] with the same object/image position at $z=-120$ mm that we analysed (in [7] the numerical values were given for a different position, see below). We tried to implement in EOD the computation of the third order geometrical aberrations from accurate ray tracing, and the mirror was again used as an example. The fit to axial rays provides Cs3 and Cs5 coefficients with an excellent agreement to published ones (see figure 1), and the first attempt provided also off axis aberrations (see table 1). Here anisotropic aberrations should be zero, but Cs3 is slightly lower than the correct value, as illustrated by a slight (mis)agreement of the ray traces with the analytical expressions using the computed coefficients. Even so these results look very promising. A more serious analysis was tried for the only usable recent data with the two tube electrostatic lens of Liu [9]. Here it was possible to obtain a complete set of 5th order geometrical aberrations (Oral, unpublished).

Another complex problem that could be analysed with EOD is the hexapole aberration corrector [10]. Figure 3 shows what happens to the circular beam entering the corrector.

Table 1. Fitted aberration coefficients to ray tracing for mirror.

Image position zi=	-38.744 mm
Image magnification=	-1.00004 times
Angular magnif.=	-0.99991
Defocus=	-1.1127126E-03 mm
Aberration coefficients	calculated from real rays!
Sum of squares=	2.25E-09 mm ²
Error per particle=	5.03E-8 mm
request.=	5.00E-7 mm
Traced particles=	955
Aberration coefficients	related to image
axial spherical aber.:	-3.245E+03 mm
iso,aniso coma length:	-1.705E+02, -1.111E-03
field curvature:	-4.796E+00 1/mm
iso,aniso astigmatism:	-2.196E+00, -2.943E-06 1/mm
iso,aniso distortion:	-6.582E-02, -9.258E-07 1/mm ²

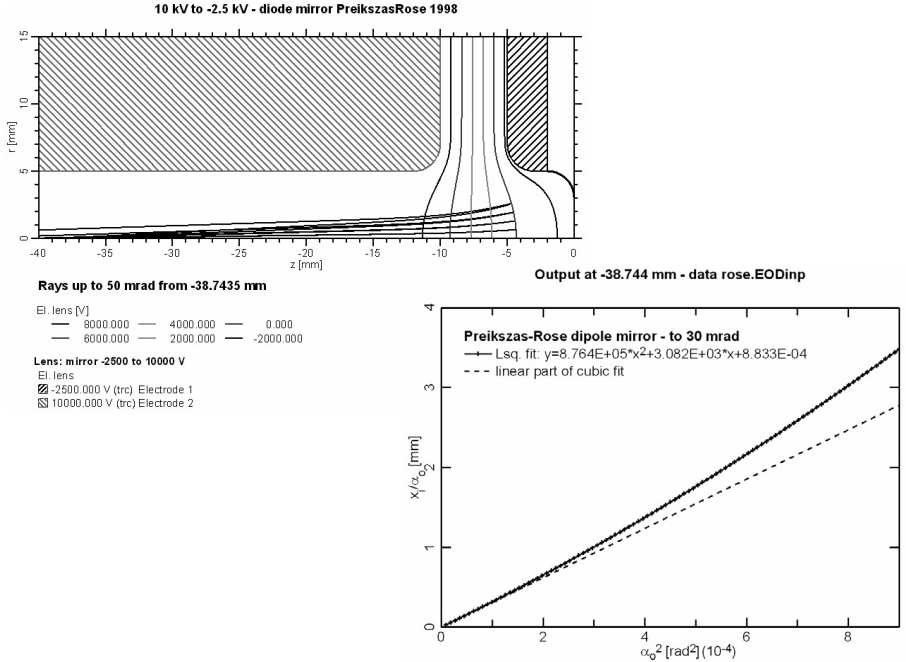


Figure 1. The geometry of the dipole mirror with representative equipotentials and trajectories (top) and the axial geometrical aberrations obtained by fitting in EOD, which evaluates correctly the effect of fifth order spherical aberration. Up to about 8 mrad the fifth order aberration has negligible effect.

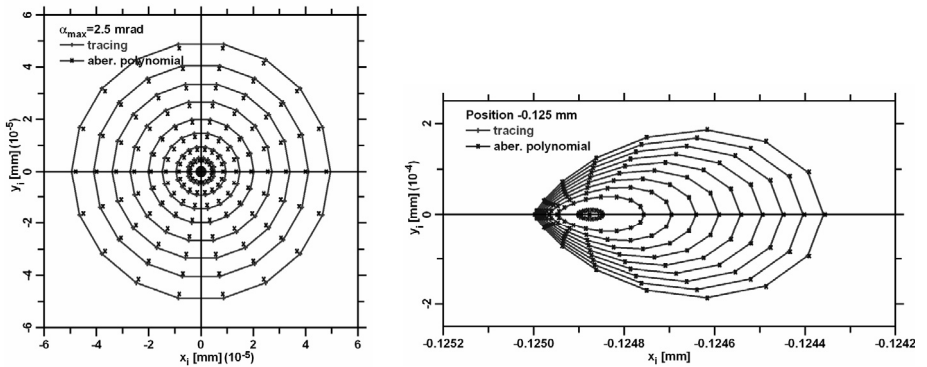


Figure 2. Axial and off axis image of a point object by the mirror: a comparison of positions by ray tracing and from analytically computed values using the coefficients shown in table 1. The initial angle changes linearly in α_o^2 .

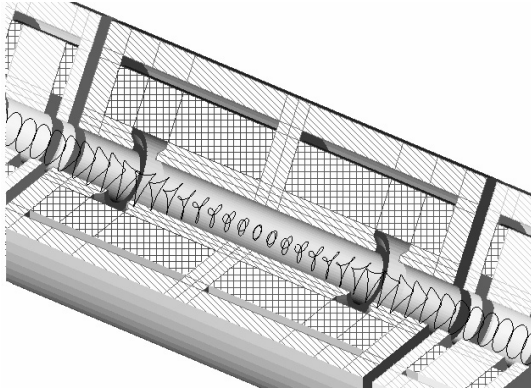


Figure 3. Beam profile of a circular beam inside hexapole corrector. The initial beam radius is 0.1 mm, the beam distance from the axis is magnified 50 times.

5. Conclusions

The EOD program has reached a high degree of maturity. It has a complete and extensive documentation of some 200 pages, an on-line help available as 200 pages of PDF, and a number of documented examples. The development of any software like EOD is a never-ending process. The applications of EOD are ranging from detector design via computations of individual lenses to systems and their optimization. New problems and applications, such as space charge or electron-gas interactions, force us to improve and extend the existing program.

References

- [1] B. Lencová and J. Zlámal, CPO7 abstracts at www.mebs.co.uk.
- [2] B. Lencová and J. Zlámal, *Micr. Microan. Suppl.* 3, 2-3 (2007).
- [3] D. Cubric et al, *Nucl. Instr. Meth. in Phys. Res. A*427 (1999), 357-362.
- [4] J. Chmelík and J. E. Barth, *Proc. SPIE* 2014 (1993) 133-141.
- [5] B. Lencová and J. Zlámal, *Proc. "Recent trends"*, Brno 1996, 55-56.
- [6] P. Adamec, E. Bauer and B. Lencová, *Rev. Sci. Instr.* 69 (1998), 3583-3587.
- [7] D. Preikszas and H. Rose, *J. El. Microsc.* 1 (1997), 1-9.
- [8] F. H. Read, CPO-2DS program, see <http://www.electronoptics.com>.
- [9] Z. X. Liu, *Ultramicrosc.* 106 (2006), 220-232.
- [10] M. Haider et al, *Optik* 99 (1995), 167-179.

TIME-OF-FLIGHT- AND SPIN-FILTERING IN LOW-ENERGY ELECTRON MICROSCOPY

P. Lushchik^a, M. Hahn^a, G. Schönhense^a, A. Oelsner^b, D. Panzer^b, A. Krasnyuk^c, J. Kirschner^c

^aInstitut für Physik, Johannes Gutenberg Universität Mainz (Germany)

^bSurface Concept GmbH, Staudingerweg 7, 55128 Mainz (Germany)

^cMax-Planck-Institut für Mikrostrukturphysik, Halle (Germany)

The manipulation of the electron beam in a low-energy electron microscope by “unconventional” insertion elements offers fascinating possibilities for the instrument performance. Besides common image information, there are additional degrees of freedom in the electron beam that can be exploited: The electrons’ time-of-flight (TOF) and spin polarisation (SP). In this contribution we will discuss novel approaches giving access to these degrees of freedom. TOF filtering is established in several groups (for a recent review see [1]), whereas spin filtering is just being tested for the first time.

The possibility of **TOF-filtering** was first demonstrated using a gated camera [2]. Due to the limited time resolution of the fluorescent screen, we moved to a different approach using a delayline detector (DLD) [3] as an imaging device, being originally developed for coincidence detection of particles. Recent advances led to a lithographically-fabricated meander-type detector that is characterised by far better impedance matching and by an excellent long-term stability compared to a wire detector containing flat coils of very thin wires around ceramics rods. Fig. 1 shows a photo of the meander (a) and PEEM-images (b,c) taken with this detector. In measurements on Ag dots on Si under excitation with a blue laser (400 nm) we obtained “hot spot” emission on a dark background. These high contrast images show an ultimate dynamic range up to 10^6 , which surmounts the dynamic range of the common image detector (MCP-fluorescent screen-CCD camera) by orders of magnitude. This is a virtue of the coincidence technique used for image formation in a DLD, where single-electron detection is employed and the x, y and t coordinates of each counting event are determined via precise time measurements. The present time resolution of the DLD (best achieved: 108 ps) translates into an energy resolution of better than 100 meV at a drift energy below 50 eV for the given geometry of our TOF-PEEM.

Dynamic manipulation of TOF-dispersed beams opens fascinating possibilities for aberration correction [1]. The approach is based on precise time-dependent operation of lenses

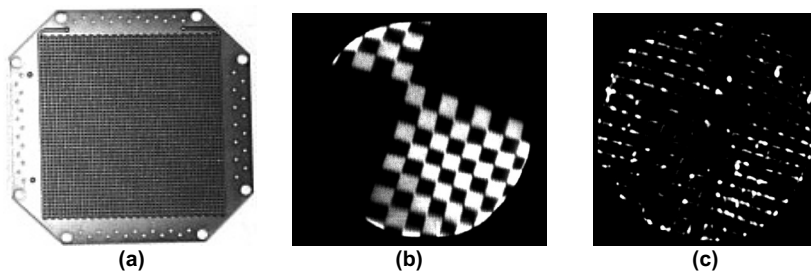


Figure 1: Meander delayline detector (a) and PEEM images of (b) test structure (Chessy, Plano) and (c) “hot-spot” emission from Ag nanodots on Si taken with this image detector.

or acceleration elements, phase locked with the pulsed electron signal from the sample. This opens a new field of research and development because femtosecond lasers and synchrotron radiation provide sources with excellent repetitive time structure.

The *spin degree of freedom* is exploited in SEMPA [4] (being not suited for real-time imaging of fast processes) and SP-LEEM [5] using diffraction of polarised electrons from magnetic surfaces for generating high magnetic contrast. We are developing two alternative approaches by implementing an imaging spin-filter into the column of a low-energy microscope. In the first set-up, illustrated in Fig.2, spin-polarised electron diffraction from a single crystal surface is used for spin filtering. A telescopic beam is reflected from the surface such that the electron-optical image is retained and can be further magnified and viewed on an imaging unit. The method makes use of the Bragg condition for the electron rays in combination with spatial separation of the rays analogous to an optical mirror. Inelastic and diffuse scattering can be suppressed by an additional “diffraction-contrast aperture“ located in a crossover plane behind the spin filter crystal.

An alternative method uses spin dependent transmission through an ultra thin ferromagnetic foil at low electron energies where the mean free path increases steeply. From spectroscopy experiments it is known that the optimum analysing power of such a transparent foil can be very high due to the differences in inelastic mean free path for low-energy electrons in ferromagnets [6]. For the generation of an electron-optical image at very low energy close to the threshold we use a special strategy that generates a magnified image on the plane of the spin filter foil.

In combination, TOF- and spin-filtering based on diffraction will constitute a spin-resolved spectromicroscope. The optimum working point of the analyser crystal allows for the simultaneous analysis of energy intervals $> 3\text{eV}$. In addition, dynamic refocusing of the lens system synchronised with the excitation source facilitates chromatic aberration correction.

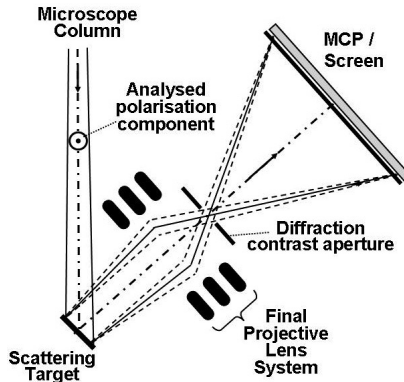


Figure 2: Spin-filtering in a low energy electron microscope in the diffraction mode. The contrast is based on spin polarised electron diffraction from a single crystal surface.

The project is supported by DFG (SCHO341/9-1).

References:

- [1] G. Schönhense, H.J. Elmers, S.A. Nepijko, C.M. Schneider, Adv. in Imaging and Electron Phys. **142**, 159 (2006)
- [2] H. Spiecker et al., Nucl. Instr. and Meth. A **406** (1998) 499
- [3] A. Oelsner et al., Rev. Sci. Instrum. **72** (2001) 3968
- [4] H.P. Oepen, J. Kirschner, Scanning Microsc. **5** (1991) 1
- [5] Th. Duden, E. Bauer, Surf. Rev. Lett. **5** (1998) 1213
- [6] G. Schönhense, H. C. Siegmann, Ann. Phys. **2** (1993) 465

LOW ENERGY ELECTRON MICROSCOPY FOR SEMICONDUCTOR APPLICATIONS

M. Mankos, V. Spasov, L. Han, S. Kojima, X. Jiang, S. Harb, L. Grella and C. Czarnik
KLA-Tencor, 160 Rio Robles, San Jose, CA, USA
email:marian.mankos@kla-tencor.com

A LEEM suitable for semiconductor applications must be capable of imaging insulating surfaces at high throughput. Increased throughput requires a large total beam current, which results in increased e-e interactions. We have introduced several new electron-optical components into a LEEM column to minimize e-e interactions: a magnetic immersion objective lens, a tunable magnetic prism array and a magnetic immersion gun lens. A dual beam approach, where two beams with different landing energies illuminate the field of view, is used to mitigate the charging effects when the LEEM is used to image semiconductor substrates with insulating or composite (insulator, semiconductor, metal) surfaces.

The cathode objective lens is one of the key components determining the performance of a LEEM. In general, the e-e interactions can be reduced for a given beam current in the cathode objective lens by increasing the illuminated area, which decreases the current density. We have found [1] that an immersion magnetic lens shows a significantly reduced effect of e-e interactions for currents as high as several μA . This is due to the fact that electrons emitted from rest inside a magnetic field have a finite angular velocity when they emerge in the field free region which prevents the formation of a sharp, well defined crossover in the back-focal plane of the objective lens, resulting in reduced e-e interactions. The crossover becomes dependent upon the illumination area, and increases with increasing magnetic flux density at the substrate. In such a lens, the e-e interactions-induced blur becomes practically independent of beam current at low current densities. This means that large currents can be used for imaging, provided the current density is kept below a threshold of approximately 10 mA/cm^2 (at 20keV).

The second key electron-optical component is the beam separator, in our case a magnetic prism array. The electron-optical properties of the prism array strongly impact the design of the entire tool, since the physical size of the prism array determines the location of the image and diffraction planes. Unfortunately, the focusing properties of simple magnetic prisms differ considerably in the horizontal and vertical planes, giving rise to large astigmatism and distortion. Ideally, we need a magnetic prism with a net deflection of 90° which behaves like a set of round lenses and images simultaneously the real-space image of the sample and the diffraction pattern (back-focal plane of the objective lens). This can be achieved in a close-packed magnetic prism array [2,3], consisting of a large, central square magnetic field, surrounded by several smaller regions where the magnetic field is about three times stronger and in the same direction.

The third novel electron-optical component of our high-throughput LEEM is the illumination optics. The immersion nature of the objective lens strongly impacts the design of the illumination optics, in particular for the mirror mode. In the mirror electron microscopy imaging mode, the illuminating electrons are reflected above the surface, without hitting the surface. In order to obtain high spatial resolution, the electrons must turn around just several nanometers above the surface. In a magnetic immersion objective lens, this can be achieved at points near the optical axis. However, at points further from the optical axis, the electrons (when emitted from a conventional electron gun) acquire a 'twist', i.e. the electrons' angular velocities in the magnetic field cause them to have circumferential kinetic energies at the turning point, which are proportional to the square of their off-axis distances. The total energy of the electron is conserved, so the axial energy component is reduced. As a

result, the distance of the turning point from the substrate increases, causing a serious degradation of resolution, particularly for large fields of view. In systems with rotationally symmetric magnetic fields, an electron beam typically has an angular velocity inside the lens magnetic fields, and zero angular velocity outside the magnetic field. However, this situation can be reversed if we can arrange for the beam to have an angular velocity when it is outside the magnetic field. This situation can be produced by immersing the cathode of the electron gun in a magnetic field. In this case, the electrons are emitted normal to the cathode, i.e. without angular velocity, inside the magnetic field, and when they emerge from the magnetic field they then have a finite angular velocity in the field free region. If the beam then passes back into a magnetic field, the angular velocity can be cancelled inside the field. By appropriately matching the magnetic field at the cathode to the magnetic field at the wafer, it is possible in principle to cancel the circumferential velocity at the wafer, and the illumination optics is considered to be twist-corrected (Fig.1).

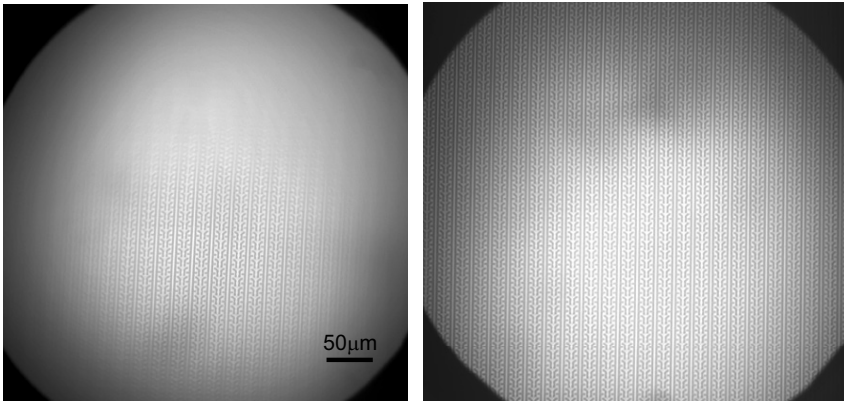


Figure 1. Experimental confirmation of twist correction. Right image – mirror image optimized for maximum field of view; left image – mirror image with all lenses unchanged except the immersion gun lens, which is reversed in polarity.

The dual beam approach is driven by the difficulties encountered when electron microscopes are used to image insulating surfaces. The imbalance between the arriving and leaving flux of electrons causes the surface to charge up, resulting in increased blur and distortions. On a homogeneous insulator surface, the charging can be suppressed by operating at a landing energy resulting in a net secondary yield of 1. However, this approach restricts the landing energy and typically does not work when different insulating materials are present on the surface. We have developed a dual beam approach that mitigates the charging effect when two electron beams with different landing energies are used for imaging [4]. The first beam is partially mirrored and its high energy tail is absorbed, which charges the surface negatively (Fig. 2a). The second beam strikes the wafer with energies of typically few hundred eV, which results in a total (secondary and backscattered) yield larger than 1 that charges the surface positively. The charge equilibrium, required to image insulating surfaces, is achieved when the negative charge of the mirror beam that is absorbed equals to the positive charge created by the higher energy beam. This state of charge control is a dynamic quasi-equilibrium, and the surface is at a potential that is slightly ($<1\text{eV}$) more negative than the cathode potential (0V), depending on the fraction of absorbed mirror electrons. This is

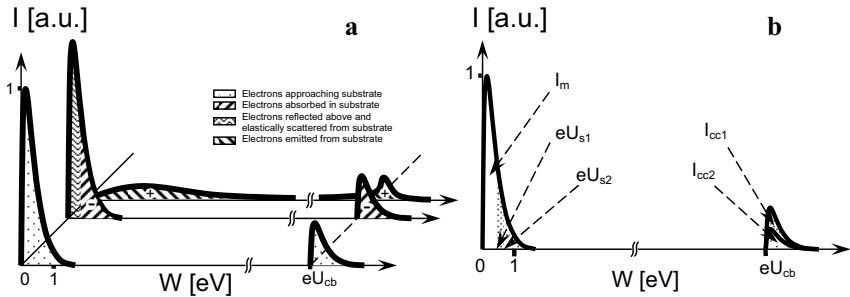


Figure 2. (a) - Energy spectrum of illuminating electrons approaching the substrate surface and signal electrons leaving the surface, U_{cb} - relative cathode bias; (b) - Energy spectrum for two different charge control currents..

demonstrated in Fig. 2b. When the charge control beam current I_{cc1} (or total yield σ) slightly increases, the surface begins to charge positively, thus attracting the mirror beam, and a slightly larger number of mirror beam electrons will get absorbed, returning the insulating surface to a charge equilibrium at a slightly less negative potential U_{s1} when compared to the cathode potential. Similarly, when the charge control beam current I_{cc2} (or total yield σ) slightly decreases, the surface begins to charge negatively, which repels the mirror beam, and a slightly smaller number of mirror beam electrons will get absorbed, returning the insulating surface to a charge equilibrium at a slightly more negative potential U_{s2} when compared to the cathode potential. The potential variation is expected to be small and is greatly exaggerated in Fig. 2b, considering the small width and steep slope of the energy distribution and the typical emission stability achieved with electron sources (<1%).

We have experimentally generated two independent electron beams in an illumination optics with two perpendicular branches (Fig.3), which are combined by an additional magnetic prism array combiner [5]. In our dual beam approach, we have introduced two

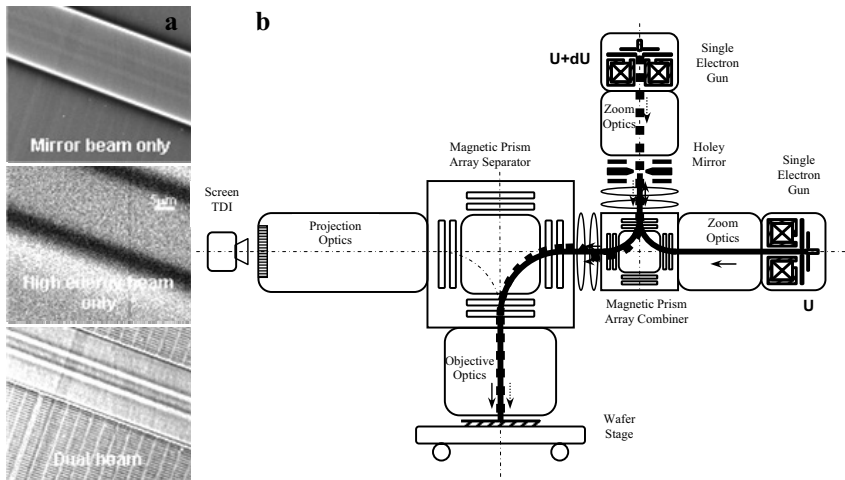


Figure 3. (a) - Dual beam charge control on a gate layer Si wafer;(b) - Layout of electron-optical column with dual beam illumination.

perpendicular branches (Fig.3b) in the illumination optics, which are combined by an additional magnetic prism array combiner. The horizontal lower energy beam is deflected in the combiner by 90 degrees into a semitransparent, holey mirror, which reflects the electrons back. The combiner deflects this beam back into the horizontal microscope axis, and the prism array separator deflects it into the objective lens, where the electrons are decelerated and focused by the objective lens on the specimen. The vertical, few hundred eV higher energy electron beam passes through the semitransparent, holey mirror and becomes coaxial with the first, lower energy beam. The magnetic prism array combiner deflects this beam by slightly less than 90 degrees back almost parallel to the horizontal microscope axis, and when the magnetic prism array combiner and separator have identical dispersion, the higher beam is deflected by the magnetic prism array separator into the objective lens, thus making the two beams at different energies coaxial again. We have experimentally demonstrated this phenomenon by imaging a variety of semiconductor device wafers without deleterious charging effects.

The experimental verification of the dual beam charge control approach was successfully demonstrated on a variety of semiconductor substrates [6]. We have imaged semiconductor wafers with a variety of structures and materials on the surface, including oxide structures and gate structures on silicon, flat surfaces incorporating metals and insulators after a chemical-mechanical polishing process on silicon and silicon-on-insulators substrates, resist-coated wafers, as well as imprint masks on quartz substrates.

References

1. M. Mankos and D. Adler, *Ultramicroscopy*, **93**, p. 347 (2002).
2. V. Kolarik, L.H. Veneklasen and M. Mankos, *Optik*, **87**, p. 1 (1991).
3. R. Degenhardt, *Ph.D.Dissertation*, Technische Hochschule Darmstadt (1992).
4. L.H. Veneklasen and D.L.

HARD X-RAY PHOTOELECTRON SPECTROSCOPY UP TO 15 KEV: RECENT DEVELOPMENTS AND RESULTS WITH A NOVEL INSTRUMENT

M.Merkel^{1*}, M.Escher¹, N.Weber¹, J.R.Rubio-Zuazo², G.R.Castro²

¹FOCUS GmbH, Huenstetten, Germany

²SpLine Spanish CRG Beamline at the ESRF, Grenoble, France

*m.merkel@focus-gmbh.com

Hard X-ray photoelectron spectroscopy (HAXPES) is a new method for non destructive and bulk sensitive chemical analysis. Its advantage over conventional XPS is based on the long mean free path of high energetic electrons. The information depth can reach several 10 nm for 15keV electrons. New instruments and the availability of a number of suitable high energy synchrotron beam lines allows for the realization of dedicated instrumentations [1].

We developed an analyzer for HAXPES with energies up to 15 keV that simultaneously fulfils the geometrical restrictions of the XRD (X-ray diffraction) setup. After commissioning the instrument in 2006 it is used routinely for two years now in the full energy range at the Spanish CRG-beam line SpLine at ESRF in Grenoble. A partial view of the setup with the analyzer is shown in figure 1.

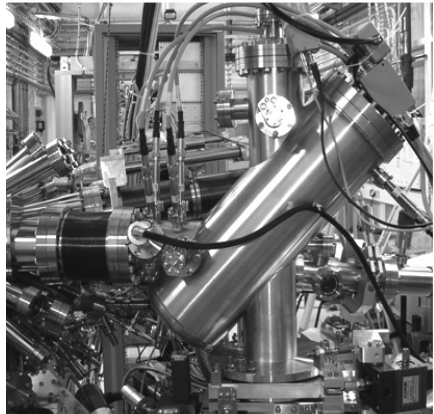


Figure 1: The HV CSA analyzer setup at the Spanish beam line SpLine at the ESRF in Grenoble. The setup is designed for simultaneously HAXPES and XRD measurements.

The analyzer is an electrostatic cylinder-sector (FOCUS HV CSA). With its compact geometry and high transmission due to second order focusing it is highly efficient for high energy spectroscopy. The analyzer is capable to handle kinetic energies both up to 15 keV and down to a few eV with the same analyzer setup and power supply [2].

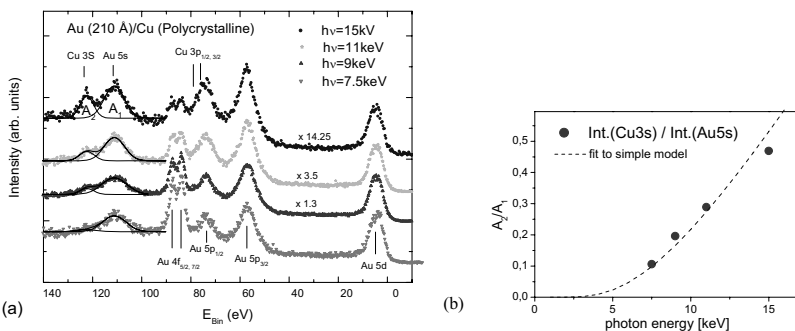
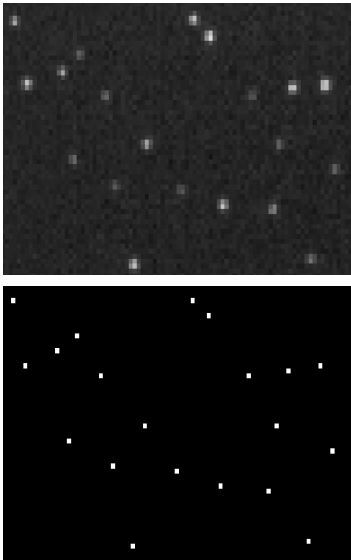


Figure 2: (a) HAXPES spectra on a Cu sample coated with a 21 nm Au overlayer. Note the absolute and relative cross section differences.

(b) Energy dependence of the substrate (Cu 3s) and overlayer (Au 5s) signal intensities.

A fit with simple models delivers the layer thickness and interface properties.

Buried layers, as they are common for a number of nano-technological applications, are invisible with most non-destructive analytical methods. To demonstrate the potential of electron spectroscopy to obtain properties of buried layers and interfaces at high kinetic energies we used a 21nm thick Au layer deposited onto a clean Cu substrate as a model system for bulk sensitive photoemission. Representative spectra of Au and Cu peaks excited with different photon energies are shown in figure 2. Absolute and relative peak intensities evolve with the photon kinetic energy due to different mean free path lengths and different cross sections. The analysis of substrate and overlayer intensities with simple models can yield the thickness of the overlayer and even the thickness of an interdiffusion layer or an interface roughness, if the layer thickness is known from other methods e.g. from XRD [3]. The relevant depth information can efficiently be probed with electron energies ≥ 10 keV only.



As an important recent improvement of the analyzer, the implementation of a 2D detector will be described. The 2D detector consists of a camera based single event counting system that will increase the measurement speed. By this means we will overcome the restrictions imposed by the low cross sections at high kinetic energies. At the same time this approach is well suitable to get rid of the high detector potential of up to 15 kV.

First results obtained with the new detector will be presented and the increase in transmission and energy resolution will be discussed.

Figure 3 (left): 2-D event counting;
top: single frame shot of the detected events;
bottom: the same map of events after applying the
discrimination algorithm

This work was supported through the Spanish Ministry of Education and Science (MEC), grants nos. FAP-2001-2166 and MAT1999-0241-C01 and the German Ministry of Education and Research (BMBF) under grant no. FKZ 13N9033.

- [1] Proceedings of the Workshop on Hard X-ray Photoelectron Spectroscopy, Nucl. Instr. Meth. Phys. Res. A 547 (2005). Workshop on Hard X-ray Photoelectron Spectroscopy 2006, Spring-8, Japan, September 2006.
- [2] M.Escher, M.Merkel, J.R.Rubio-Zuazo, G.R.Castro, Proceedings of the 10th Int. Sem., Skalsky Dvur, 2006, p.17
- [3] J.R.Rubio-Zuazo, M.Escher, M.Merkel, G.R.Castro, J. Phys. Conf. Ser.**100** (2008) 072032
J.R.Rubio-Zuazo, G.R.Castro, J. Phys. Conf. Ser.**100** (2008) 012042

UNIFIED ABERRATION THEORY OF NARROW AND WIDE BEAMS: TENSOR VERSION OF THE TAU-VARIATION APPROACH

M. Monastyrskiy

Photoelectronics Department, A.M. Prokhorov General Physics Institute

Russian Academy of Sciences

38 Vavilov Street, 119991 Moscow, Russia

monast@ran.gpi.ru

1. A little excursus to the history of aberration theory

The comparatively smooth evolution of the narrow-beam aberration theory intended mainly for electron microscope was disturbed by two papers published in the beginning of 40s. The first of the papers belonging to Recknagel [1] was devoted to imaging problems of electron mirrors. In the second one, authored by the outstanding Russian physicist Artsimovich [2], it was shown that in the case of emission-imaging systems (in particular, in cathode lenses) the routine aberration procedure based on regular perturbation theory necessarily leads to very unpleasant oddities in the aberration coefficients behavior near the emitter surface.

From mathematical standpoint, those singularities are directly connected with the presence of the “moving” singular point in the well-known *stationary trajectory equation*

$$\mathbf{r}'' + \frac{1 + \mathbf{r}'\mathbf{r}'^*}{\varphi - \varphi_0 + \varepsilon} \left(\frac{\mathbf{r}'}{2} \frac{\partial \varphi}{\partial z} - \frac{\partial \varphi}{\partial \mathbf{r}^*} \right) +$$

$$+ i \sqrt{\frac{e}{2m} \frac{1 + \mathbf{r}'\mathbf{r}'^*}{\varphi - \varphi_0 + \varepsilon}} \left[\mathbf{r}' \frac{\partial \varphi_m}{\partial z} + \mathbf{r}'^2 \frac{\partial \varphi_m}{\partial r} - (2 + \mathbf{r}'\mathbf{r}'^*) \frac{\partial \varphi_m}{\partial \mathbf{r}^*} \right] = 0 \quad (1)$$

which was first derived by O. Scherzer [3] from Lorenz equation with the use of the energy integral. Here e, m are, accordingly, charge and mass of a particle; $\mathbf{r} = x + iy$ is two-dimensional vector describing the charged particle position in the plane perpendicular to the main optical axis Oz ; φ, φ_m are, accordingly, electrostatic and magnetostatic potentials; φ_0 is electrostatic potential at the starting point; $e\varepsilon$ is particle' initial energy; the asterisk signifies complex conjugation and the upper stroke signifies differentiation with respect to the coordinate z .

It can be easily seen that the equation (1) degenerates in the vicinity of the starting point at small initial energies ε . Physically, the presence of such mathematical singularity points to some image formation peculiarities which are intrinsic to wide-beam emission-imaging system and cannot be satisfactory described in the frame of regular aberration procedures of the narrow beam theory.

Over a period of 50s-60s, and especially in 70s, a large number of papers were aimed at overcoming the difficulties revealed by Artsimowich. Concurrently and practically independently, the narrow beam theory confined by the assumption of small initial beam

apertures and high initial energies of charged particles had been permanently developing and perfecting. As a result, the difference between the narrow and wide beam aberration theories resembled the situation described in the famous novel by Jonathan Swift: the inhabitants of the Lilliput country were divided into two uncompromising belligerents - the “Little-Endians” and the “Big-Endians” - as to which end of the boiled egg should be broken first!

2. The essence of the tau-variation technique

The first version of a new versatile aberration approach - *the tau-variation technique* - valid for aberrational description of narrow and wide beams both in stationary and non-stationary electromagnetic fields was published by Monastyrskiy and Schelev [4] in 1980 as applied to the theory of temporal aberrations in ultrafast photoelectronic imaging. More extended versions, along with applications to various problems of charged particle optics, the reader can find, as example, in [5, 6]. This paper is to give a brief sketch of the latest, tensor version of the tau-variation technique.

According to the tau-variation technique, the computation of spatial and temporal aberrations consists of two numerical procedures which may be carried out “synchronously”: 1) numerical integration of a system of differential equations for isochronous variations (*tau-variations*) of the solutions of the Lorenz equation (1), and 2) linear transformation of the *tau-variations* into the aberration coefficients on each integration step (the so-called *contact transformation*).

The tau-variation technique possesses high computational stability: this follows from the fact that the tau-variations represent *regular* components of the aberration coefficients. The advantage of the invariant tensor form is that it is most convenient for program realisation and allows effective combining of the “direct ray-tracing” and “aberration” ideas in charged particle optics.

Consider the charged particles motion described by the Lorenz equation in tensor representation

$$\dot{x}^i = f^i(x, \dot{x}, \tau) = \frac{q}{m} \Gamma(\dot{x}) \left(E^i + \frac{1}{c} \varepsilon^{ijk} \dot{x}^k B^j \right) \quad (2)$$

where x^i ($i = 1, 2, 3$) are homogeneous Cartesian coordinates of the three-dimensional vector x , τ is time, E^i, B^i are, accordingly, electric and magnetic field components, q/m is charge-to-mass ratio, and ε^{ijk} is alternator tensor. The summation is made over all repeated “dumb” indexes i, j, k, \dots . The relativistic factor $\Gamma(\dot{x}) = [1 - (1/c^2) \sum_{i=1}^3 (\dot{x}^i)^2]^{-1/2}$, where c is the speed of light. We assume that the initial conditions for the equation (2)

$$x^i(\tau_0(\xi), \xi) = X^i(\xi), \quad \dot{x}^i(\tau_0(\xi), \xi) = V^i(\xi) \quad , \quad (3)$$

are dependent on the small parameters vector $\xi = \{\xi_\alpha\}$, $\alpha = 1, 2, \dots, p$, the components of which may specify the initial positions, velocities, energies, and angles of charged particles; the particles' start time; the structural parameters responsible for geometric and potential perturbations of the system' boundary; the excitation currents in magnetic coils, etc. It should be emphasized that the electric and magnetic field vectors $E^i(x, \tau, \xi)$, $B^i(x, \tau, \xi)$ in the right part of (2) are dependent not only on the coordinates and time but also on the parameters vector ξ , which makes both the optimization problem and the problem of mechanical tolerances computation automatically included in the tau-variations procedure.

According to the well known Poincare theorem, under the condition that the electromagnetic field in the domain of the bunch motion is smooth enough, the solutions $x^i(\tau, \xi)$ of the Lorenz equation (2) in the vicinity of any *principal trajectory* $x(\tau, 0)$ may be expanded into the Taylor power series

$$x^i(\tau, \xi) = x_0^i(\tau) + \sum_{\alpha=1}^P x_{\alpha}^i(\tau) \xi_\alpha + \frac{1}{2} \sum_{\alpha, \beta=1}^P x_{\alpha\beta}^i(\tau) \xi_\alpha \xi_\beta + \frac{1}{6} \sum_{\alpha, \beta, \gamma=1}^P x_{\alpha\beta\gamma}^i(\tau) \xi_\alpha \xi_\beta \xi_\gamma + \dots \quad (4)$$

which uniformly converges within a finite time interval $\tau \in [0, \tau_{\max}]$. The coefficients of this expansion are the partial derivatives

$$x_{\alpha\beta\dots}^i(\tau) \equiv \left. \frac{\partial^n x^i(\tau, \xi)}{\partial \xi_\alpha \partial \xi_\beta \dots} \right|_{\xi=0} \quad (n = 1, 2, \dots) \quad (5)$$

calculated at a fixed time moment τ . We call the coefficients (5) the tau-variations (or isochronous variations) because the expansion (4) determines the phase state of the particles comprising the bunch at a *fixed time moment* τ . Numerical solving of the *regular* linear non-homogeneous differential equations for the tau-variations (5), which can be easily obtained in tensor form from the Lorenz equation (1) by means of consecutive varying with respect to ξ , represent the first of the two tau-variation procedures.

In contrast to celestial mechanics, in charged particle optics we are mostly interested in the particle distribution not in the temporal plane $\tau = \text{const}$ but upon a smooth surface S which we commonly call the particle collector or image receiver. Let $\tau_S(\xi)$ be the time for an individual particle "marked" by the parameter ξ to arrive at the surface S , and $x_S(\xi) = x(\tau_S(\xi), \xi)$ be the particle' position on the surface S . Under the same general assumptions of smoothness, we may represent the function $x_S(\xi) = \{x_S^i(\xi)\}$ as a series

$$x_S^i(\xi) = x_S^i(0) + \sum_{\alpha=1}^P (x_S^i)_\alpha \xi_\alpha + \frac{1}{2} \sum_{\alpha, \beta=1}^P (x_S^i)_{\alpha\beta} \xi_\alpha \xi_\beta + \frac{1}{6} \sum_{\alpha, \beta, \gamma=1}^P (x_S^i)_{\alpha\beta\gamma} \xi_\alpha \xi_\beta \xi_\gamma + \dots \quad (6)$$

in which

$$(x_S^i)_{\alpha\beta\dots} \equiv \left. \frac{\partial^n x_S^i(\xi)}{\partial \xi_\alpha \partial \xi_\beta \dots} \right|_{\xi=0} \quad (n=1,2,\dots) \quad (7)$$

are consecutive derivatives of the function $x_S^i(\xi)$ calculated on the principal trajectory at $\xi = 0$. Obviously, (6) is the aberrational representation of the beam on the surface S with respect to the set of small parameters $\{\xi_\alpha\}$, and the derivatives (7), accurate to certain factorial multipliers, are aberration coefficients on the principal trajectory $x(\tau, 0)$. It can be easily shown that the aberrations coefficients (7) may be easily obtained from the tau-variations (5) by a linear algebraic transformation which we call the *contact transformation*. Such transformation also possesses a tensor form and comprises the second of the tau-variation procedures. In the simplest case, the contact transformation is performed upon the particle collector or image receiver surface to evaluate the “final” aberrations of the bunch. Nevertheless, it is very often of interest to know the aberration coefficients on some intermediate virtual surfaces (virtual screens) being intentionally placed on the path of the bunch motion. Moreover, the possibility of displaying the aberration coefficients in the form of some continuous curves originating from the physical or virtual emitter may offer the researcher important information as to the optical properties of the system in question. In this case the contact transformation of the tau-variations into the aberration coefficients is being made on every integration step of the differential equations for tau-variations.

References

- [1] A. Recknagel. *Theorie des elektrischen elektronen Mikroskops für selbststrahler* // Z. angew. Physik, vol. **117** (1941), pp. 689 – 708
- [2] L.A. Artsimovich. *Electrostatic properties of emission-imaging systems* // *Proceedings of the USSR Academy of Sciences (physical series)*, vol. **8** (1944), no. 6, pp. 131 – 329 (in Russian)
- [3] O. Scherzer. *Die schwache elektrische Einzellinse geringster sphärischer Aberration.* // Z. angew. Physik, vol. **101** (1936), no. 1, 2, pp. 23 – 26
- [4] M.A. Monastyrskiy and M.Ya. Schelev. *Theory of temporal aberrations in cathode lenses* // Lebedev Physical Institute, the USSR Academy of Sciences, pre-print no. 128 (1980) (in Russian)
- [5] S.V. Kolesnikov and M.A. Monastyrskiy. *General theory of spatial and temporal aberrations in cathode lenses with slightly broken axial symmetry. Parts 1,2.* // Soviet Physics - Technical Physics, vol. **33** (1988), no.1, pp. 1 – 11
- [6] D.E. Greenfield, M.A. Monastyrskiy, and V.A. Tarasov. *Perturbation techniques in the problems of computational charged particle optics* // Proc. SPIE, vol. **6278** (2006), pp. 15 – 29.

DESIGN OF ABERRATION CORRECTORS USING THE DIFFERENTIAL ALGEBRAIC METHOD

Eric Munro, John Rouse, Haoning Liu and Liping Wang

Munro's Electron Beam Software Ltd, 14 Cornwall Gardens, London SW7 4AN, England

e-mail: eric@mebs.co.uk Tel & Fax: +44 20 7581 4479

Introduction

All rotationally symmetric electron lenses have positive spherical and chromatic aberration ($C_s > 0$ and $C_c > 0$) [1] and also positive field curvature. However, these aberrations can be corrected using *multipole lenses* and *electron mirrors* [2]. In the last 10 years, difficulties in the construction and alignment of aberration correctors have been overcome, and electron microscopes with aberration correctors now offer significantly better resolving power than the best uncorrected microscopes. Examples include the Nion C_s corrector [www.nion.com], the JEOL JSM-7700F SEM [www.jeol.com] with a C_s/C_c corrector from CEOS [www.ceos.com], and the "TEAM" C_s -corrected TEM with 0.05 nm imaging [investor.fei.com]. This paper describes how such correctors can be designed using the Differential Algebraic Method.

Differential Algebraic Method ("DA Method")

The "*Differential Algebraic Method*" (or "*DA Method*") [3,4] computes aberrations of any order, with any symmetry, including multipole lenses and mirrors, in a unified way. "*DA Quantities*" are used, which are polynomials containing the aberrations to the required order n , expanded in v basis variables. For mirrors and lenses, there are 5 basis variables ($v=5$), namely the initial coordinates, slope components and energy deviation (x_o, y_o, x_o', y_o' and ΔV). These DA Quantities form a new "Data Type", which can be programmed as a Class in C++. DA Quantities for the ray coordinates ($X(z), Y(z)$) and slope components ($X'(z), Y'(z)$), as functions of the axial coordinate z , are traced from object plane z_o to image plane z_i , in a single ray trace, by solving the equations of motion numerically, using DA Quantities instead of simple variables. The DA Quantities at the image plane then contain all the aberration coefficients. For electron mirrors, time t is used as independent variable (instead of z), and the DA Position ($X(t), Y(t), Z(t)$) and Velocity ($\dot{X}(t), \dot{Y}(t), \dot{Z}(t)$) are traced as functions of time t [5]. The fields for each optical element must be passed to the ray trace algorithm as differentiable analytic functions. In our software, analytic fits to the fields are generated using series of Hermite functions. We illustrate this method with three design examples of aberration correctors for e-beam equipment for the semiconductor manufacturing industry.

Quadrupole Octopole C_s/C_c Corrector for CD SEM

C_s and C_c can be corrected with 4 quadrupoles and 3 octopoles (Figure 1).

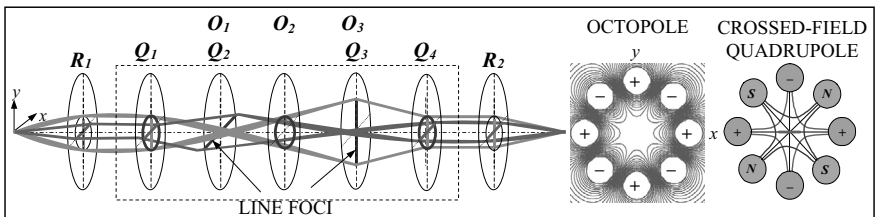


Figure 1. C_s/C_c corrector. Q_1-Q_4 =Quadrupoles. O_1-O_3 =Octopoles. R_1-R_2 = Round Lenses.

Quadrupoles $Q_1 - Q_4$ form two line foci at the planes of Q_2 and Q_3 . The octopoles $O_1 - O_3$ are adjusted to cancel C_s . C_c is corrected by making Q_2 and Q_3 crossed-field electrostatic-magnetic quadrupoles, which act as Wien filters with negative chromatic dispersion

Figure 2 shows such a corrector inserted in an electrostatic SEM column similar to [6]. An Einzel lens collimates the beam and creates a parallel beam entering the objective lens. The corrector is inserted between collimator and objective lens. The round lens fields were computed using second order finite element method (SOFEM) and the multipole fields using 3D finite difference method (3D FDM), and the axial field functions were extracted and fitted with series of Hermite functions. Paraxial rays were computed and the quadrupoles adjusted for stigmatic imaging (Figure 4). The aberrations were then computed by the DA Method.

Before correction, $C_s = 8.83$ mm and $C_c = 2.93$ mm. The magnetic quadrupoles were the adjusted to cancel C_c and the electrostatic octopoles adjusted to cancel C_s . The residual aberrations were: fifth-order spherical aberration $C_{S5} = 195.3$ mm ($d_{CS5} = C_{S5} \alpha^5$); high-rank chromatic aberrations $C_{CA} = 6.125$ mm ($d_{CCA} = C_{CA} \alpha (AV/V)^2$), $C_{CB} = 10.68$ mm ($d_{CCB} = C_{CB} \alpha (AV/V)^3$), and $C_{CC} = 76.19$ mm ($d_{CCC} = C_{CC} \alpha^3 (AV/V)$); where $\alpha =$ Numerical Aperture (NA) and $AV/V =$ fractional energy spread at image plane.

The probe diameter (Table 1) was computed before and after correction. The Gaussian beam diameter, spherical and chromatic aberration disks and diffraction disk were added in quadrature to estimate overall beam diameter. The optimum NA was found which minimized overall beam size. Before correction, optimum NA = 4 mrad with beam diameter = 16.7 nm. After correction, optimum NA = 25 mrad with beam diameter = 3.1 nm. So NA is increased by 6 \times and beam size is reduced by 5 \times , thereby improving both resolution and throughput.

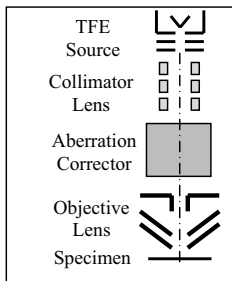


Figure 2. CD SEM column.

		<i>Before Correction</i>	<i>After Correction</i>
Optimum NA	α (mrad)	4	25
Gaussian Beam Size	d_g (nm)	2.11	2.11
Spherical Ab. Disk	d_s (nm)	0.28	0.62
Chromatic Ab. Disk	d_c (nm)	11.72	1.20
Diffraction Disk	d_d (nm)	11.67	1.87
Overall Beam Size	d_{total} (nm)	16.68	3.12

Table 1. Properties of CD SEM column before and after correction.

Hexapole Planator for Projection Electron Beam Lithography

For projection e-beam lithography, a symmetric doublet [7] is generally used, which eliminates distortion and transverse chromatic aberration. Coma can also be corrected by using two doublets [8]. The remaining geometrical aberrations – field curvature, astigmatism and spherical aberration – can only be corrected by using a multipole corrector.

Rose [9] has proposed a *hexapole planator* (Figure 3) for correcting field curvature, astigmatism and spherical aberration. It uses 6 hexapoles ($H_1 - H_6$), 4 round lenses ($L_1 - L_4$) and 2 transfer lenses (T_1, T_2). The hexapoles are energized in two groups – NI_1 is applied to H_1, H_3, H_4 and H_6 , and NI_2 to H_2 and H_5 . The hexapoles introduce second order aberrations which cancel by symmetry, and third order aberrations of **field curvature, astigmatism and spherical aberration, all with negative sign**. The hexapole strengths are adjusted to cancel the field curvature and astigmatism. The residual spherical aberration is also reduced.

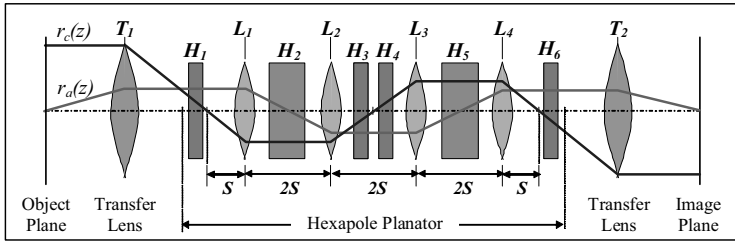


Figure 3. Hexapole planator. H_1 - H_6 =Quadrupoles. R_1 - R_4 = Round Lenses. T_1 - T_2 = Transfer Lenses.

We simulated this planator with our MULTIPOLE_WR5 software, which computes and optimizes all aberrations up to fifth order by the DA Method, and used it to correct the aberrations of a $5\times$ magnetic doublet. Figure 4 shows paraxial rays in the combined planator and doublet, and Table 2 lists the aberrations, for NA = 4 mrad. The first column shows the doublet aberrations for 200 μm square field size. Total blur is 18.8 nm. Dominant aberration is field curvature (15.3 nm). The second column shows the combined aberrations of doublet + planator, after optimizing the hexapole excitations. The planator cancels the field curvature and astigmatism and reduces the spherical aberration. The total blur is reduced to 8.61 nm. The field size can now be increased to 450 μm (see final column in Table 2), with total blur still less than 20 nm. This is a $2.25\times$ increase in field size, i.e. $5\times$ increase in projected area.

Our MULTIPOLE_WR5 software also computes the higher order aberrations. In this example, the largest residual aberration was fourth-order distortion. This could be corrected with a second planator, which corrects all fourth-order aberrations except fourth-order coma.

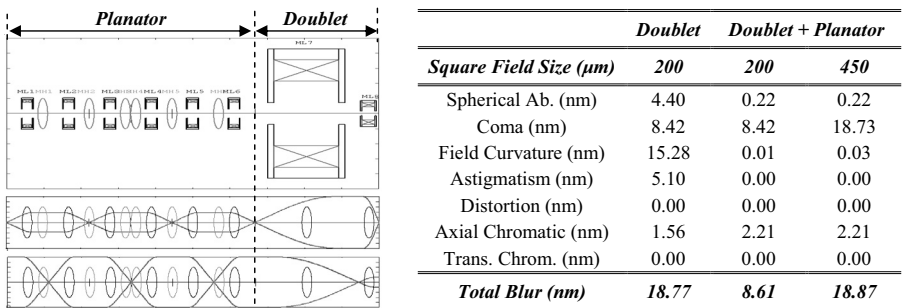


Figure 4. Paraxial rays in planator + doublet. Table 2. Aberrations of planator + doublet @ 4 mrad

Mirror Corrector for Reflective Electron Beam Lithography (“REBL”)

In *Reflective Electron Beam Lithography* (“REBL”) [10] (Figure 5(a)), the beam from an electron gun passes through a magnetic prism and is focused on to a *Digital Pattern Generator* (“DPG”). The DPG contains a matrix of tiny metallic pads, which can be individually switched positive or negative relative to cathode potential. At positive pads the incident beam is absorbed, while at negative pads it is reflected back through the prism and writes a pixel on the wafer. By appropriately setting the DPG pad voltages, any desired pattern can be written on the wafer.

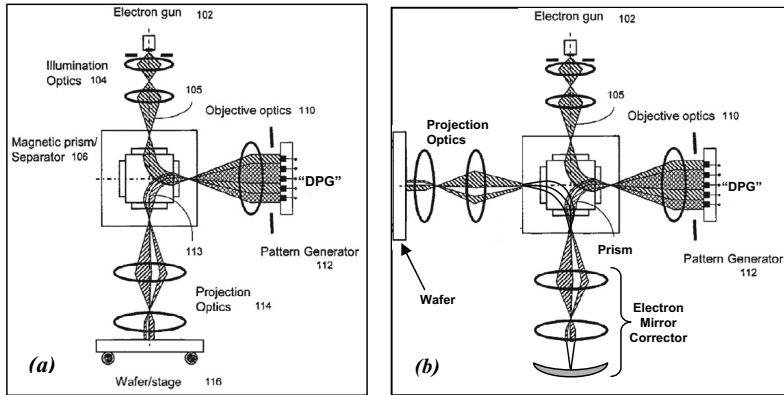


Figure 5. (a) Reflection Electron Beam Lithography. (b) With electron mirror corrector added.

The aberrations in REBL could be corrected with electron mirror (Figure 5(b)). We simulated a pentode mirror (Figure 6) with our MIRROR_DA software. The electrode voltages were adjusted to give negative spherical aberration, chromatic aberration and field curvature. Using the same $5\times$ magnetic doublet as in Figure 4, we computed the combined aberrations of mirror and doublet. Table 3 listed the results for $NA = 4$ mrad. The first column lists the aberrations of the doublet alone, for $200\ \mu\text{m}$ square field size. The second column lists the aberrations of doublet + mirror. The mirror reduces field curvature from $15.3\ \text{nm}$ to $1.2\ \text{nm}$ and eliminates chromatic aberration. Overall blur is reduced from $18.8\ \text{nm}$ to $12.1\ \text{nm}$. The field size can now be increased to $283\ \mu\text{m}$ square (see final column), maintaining total blur of $< 20\ \text{nm}$. So the mirror corrector allows the projected area to be doubled for a similar blur.

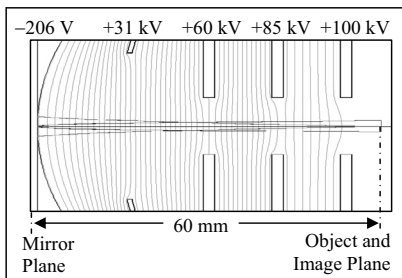


Figure 6. Pentode electron mirror.

	Doublet	Doublet + Mirror	
Square Field Size (μm)	200	200	283
Spherical Ab. (nm)	4.40	4.38	4.38
Coma (nm)	8.42	8.42	11.91
Field Curvature (nm)	15.28	1.17	2.34
Astigmatism (nm)	5.10	7.39	14.78
Distortion (nm)	0.00	0.00	0.00
Axial Chromatic (nm)	1.56	0.02	0.02
Trans. Chrom. (nm)	0.02	0.00	0.00
Total Blur (nm)	18.77	12.09	19.62

Table 3. Aberrations of mirror + doublet ($NA=4\text{mrad}$)

References

- [1] O. Scherzer, *Z. Physik* **101**, 593 (1936).
- [2] O. Scherzer, *Optik* **2**, 114 (1947).
- [3] M. Berz, *Particle Accelerators* **24**, 109 (1989).
- [4] L. Wang, T. Tang and B. Cheng, *Optik* **111**, 285 (2000).
- [5] L. Wang, J. Rouse, E. Munro, H. Liu and X. Zhu, *Optik* **119**, 90 (2008).
- [6] J. Zach and M. Haider, *Nuclear Instrum. Meth. in Phys. Res. A* **363**, 316 (1995).
- [7] M.B. Heritage, *J. Vac. Sci. Technol.* **12**, 1135 (1975).
- [8] E. Munro, X. Zhu, J. Rouse and H. Liu, *Proc. SPIE* **4510**, 218 (2001).
- [9] H. Rose, *Proc. 12th European Cong. on Electron Micros.* (Brno, Czech Republic), **Vol. 3**, 121 (2000).
- [10] M. Mankos et al., "Maskless reflection e-beam projection lithography", US Patent 6,870,172 B1 (2005).

LOW ENERGY ELECTRON MICROSCOPY IN MATERIALS SCIENCE

I. Müllerová¹, K. Matsuda², L. Frank¹

¹Institute of Scientific Instruments ASCR, v.v.i., Královopolská 147, 612 64 Brno, Czech Republic, e-mail: ilona@isibrno.cz

²Faculty of Engineering, University of Toyama, 3190 Gofuku, Toyama 930-8555, Japan

In the standard Scanning Electron Microscope (SEM) the secondary electrons (SE) are traditionally collected by a detector side-attached somewhere below the objective lens (OL), while an axially symmetrical detector located just above the specimen collects the backscattered electrons (BSE). The collection efficiency of these detectors is relatively low and amplification of the BSE detector decreases at low primary beam energies (E_p), otherwise highly advantageous for the SEM operation [1].

Collection efficiency and amplification of the BSE detector can be considerably improved when using the cathode lens mode (CLM) [2]. If the BSE detector at ground potential serves as an anode of the CL and the negatively biased specimen forms the CL cathode, the signal electrons are accelerated in the CL field toward the detector and collimated toward the optical axis. In this way, nearly 100% collection efficiency and a high detector amplification are achieved in the energy range from the primary beam energy of, say, 10 keV down to units of eV with the nominal lateral resolution preserved throughout this energy range. When the circular, axially symmetrical BSE detector is split to several coaxial rings, images formed by electrons emitted under various polar angles can be distinguished and hence attention drawn to the emission anisotropy from crystalline samples [3].

The CL was originally used as a part of the objective lens for emission electron microscopes operated below 100 eV at a high resolution of images [4]. We are using a similar OL for nearly twenty years in the SEM [2,5] and have found this type of the objective lens excellent not only at the lowest energies but even in the low keV range.

Figure 1 shows the superconductive MgB_2/Al composite material extruded into wires, imaged with a side-attached SE detector at $E_p = 10$ keV (left) and in the CLM at the landing energy of $E_L = 2$ keV (right). The CLM image not only offers a better resolution thanks to small interaction volume and preserved low aberrations, but also a higher contrast, which is optimum at 2 keV for these materials, as well as a high signal to noise ratio owing to the high collection efficiency. An example of applying the BSE detector with eight concentric channels to a polycrystalline sample in the CLM is shown in Figure 2. The highest grain contrast is formed by the high-angle inelastic BSE emitted at about $E_p/4$ while the outermost annulus of the detector acquires the high-angle elastic BSE exhibiting the supreme surface sensitivity. Figure 3 shows pyramidal precipitates appearing when silver is added to the Al-Mg-Si alloy. While the standard BSE image shows only some silver-depleted zones around precipitates, the CLM reveals an internal structure of the precipitates unexplained as yet.

[1] Pawley J.M., in: *Advances in Electronics and Electron Physics* 83 (ed. P.W. Hawkes), Academic Press, Inc. (1992) 203-274.

[2] Müllerová I. and Frank L., in: *Advances in Imaging and Electron Physics* 128 (ed. P.W. Hawkes), Elsevier (2003) 309-443.

[3] Müllerová I., Konvalina I. and Frank L.: *Material Transactions* 48 (2007) 940-943.

[4] Recknagel A.: *Z. Phys.* 117 (1941) 689-708.

[5] Müllerová I. and Lenc M., in: *Proc. XII ICEM* (ed. Peachey L.D. and Williams D.B) San Francisco Press, Inc., Vol. 1 (1990) 398-399.

[6] Work supported by the E!3963-ICD project of Eureka (OE08012).

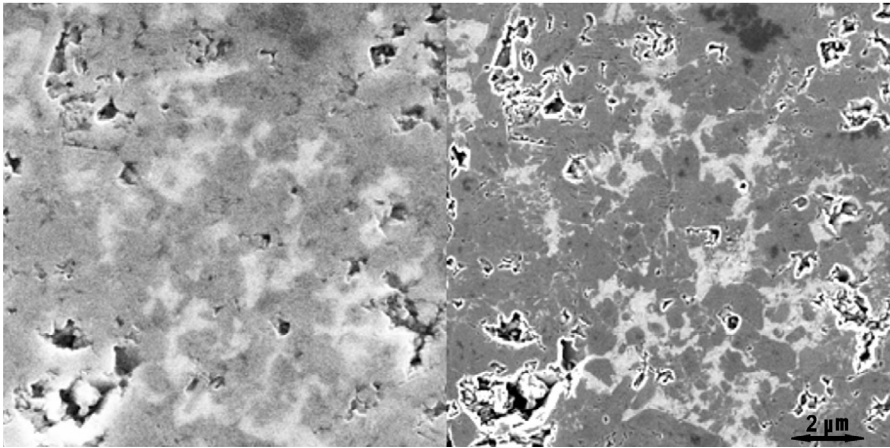


Fig. 1: Superconductive MgB_2/Al composite material imaged by a side-attached SE detector at $E_p = 10$ keV (left) and in the CLM at $E_p = 10$ keV and $E_L = 2$ keV (right).

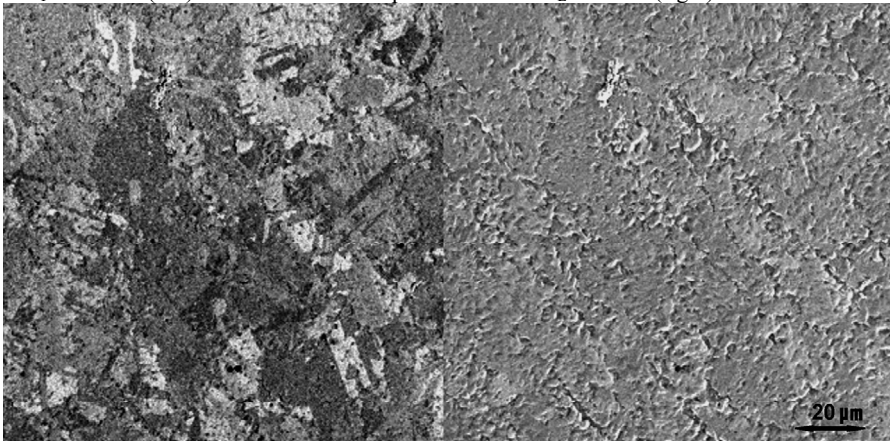


Fig. 2: Ni surface imaged in the CLM by a multi-channel BSE detector; signals of the second (left) and the outermost (right) rings at $E_p = 10$ keV and $E_L = 4$ keV.

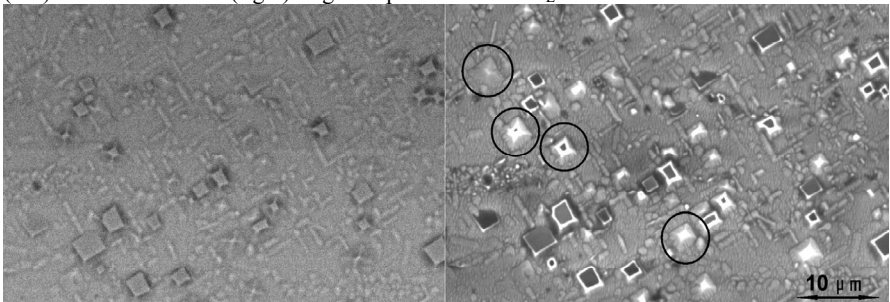


Fig. 3: Al-1.0 mass% Mg_2Si -0.5 mass% Ag alloy imaged by the standard BSE signal at $E_p = 10$ keV (left) and in the CLM at $E_p = 10$ keV and $E_L = 4$ keV (right).

SIGNAL TRANSPORT IN SCINTILLATION DETECTORS OF SECONDARY ELECTRONS IN SEM

Libor Novák

Institute of Scientific Instruments of the ASCR, v.v.i., Brno, Czech Republic
lnovak@isibrno.cz

Introduction

The scintillator-light guide-photomultiplier combination has been used for the detection of the secondary electrons (SE) in the SEM for decades [1]. The signal yield of the detector and the statistical distribution of this signal are determined by the following processes and parameters of the detector:

- SE emission from the sample
- detector collection efficiency
- conversion of electrons to photons in the scintillator
- efficiency of the light transfer from the scintillator to the photomultiplier
- pulse-height distribution of the photomultiplier
- signal digitalization

The aim of this study is to analyze the experimental data describing the signal transfer in the scintillation detector and to create a numerical simulation of the detection channel.

Experimental data

Part of the data concerning the light yield of the scintillator and the light transfer from the scintillator to the photomultiplier was taken from earlier studies [2, 3]. In order to examine the time-response of the scintillation detectors, a fast detection system with a time constant of 3 ns was developed [4]. The response of the scintillation detector was measured for the detector directly bombarded by the primary beam to eliminate the influence of the SE emission from the sample. For very low primary currents, single electron responses were recognizable at the output of the detection system and were further separable to single photoelectron responses (Fig. 1). The distribution of the number of photoelectrons was measured for several different scintillators (Fig. 2) and for different energies of primary electrons (Fig. 3). The pulse-height distribution of the photomultiplier output pulses was derived from the heights of the pulses forming single electron responses (Fig. 4).

Numerical simulation

The data obtained in this way were used for the numerical simulation (SIMULANT program) of the signal transfer in the scintillator-light guide-photomultiplier detector. In the user interface of this program, the shape of the sample line-scan as well as the parameters of the detection system should be specified. During the numerical simulation, randomly generated numbers enter the inversion cumulative distribution functions of the processes taking place in the detection channel. Various signal processing modes, including the counting of pulses, can be applied to the signal. The simulated detector output signal can further be processed in order to obtain the signal to noise ratio and the detective quantum efficiency that are generally considered as a measure of the detector performance.

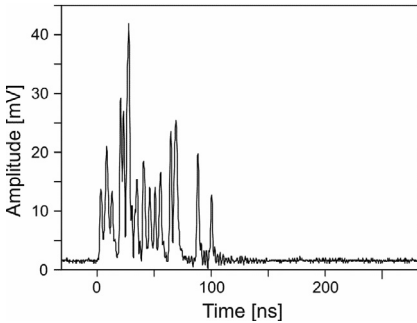


Fig. 1: Response to one 10 keV electron at the output of the photomultiplier. Short pulses are responses to individual photoelectrons.

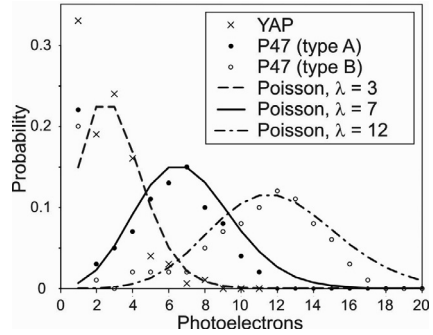


Fig. 2: Distribution of the number of photoelectrons forming a single electron response; three scintillators were tested using a 10 keV primary beam and the acquired data were fitted by the Poisson distribution.

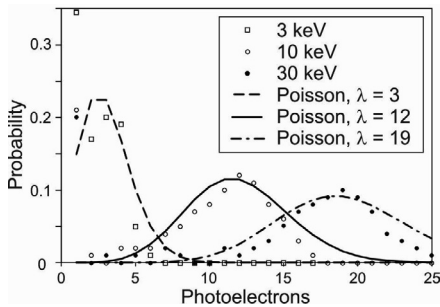


Fig. 3: Distribution of the number of photoelectrons forming a single electron response; P47 (type B) scintillator (Fig. 2) was tested under 3, 10 and 30 keV primary beam.

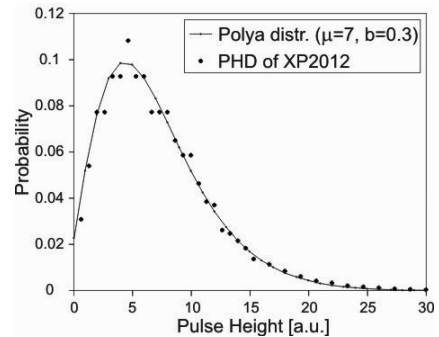


Fig. 4: Pulse-height distribution (PHD) of the XP2012 photomultiplier used for the experiment (fitted by the Poly distribution).

References:

- [1] T.E. Everhart, R.F.M. Thornley: Wide-band detector for micro-microampere low-energy electron currents. *J. Sci. Instr.* 37 (1960), p. 246-248
- [2] W. Baumann, L. Reimer: Comparison of the Noise of Different Electron Detection Systems Using a Scintillator-Photomultiplier Combination. *Scanning* 4 (1981), p. 141-151
- [3] C.W. Oatley: The detective quantum efficiency of the scintillator/photomultiplier in the scanning electron microscope. *J. Microsc.* 139 (1985), p. 153-166
- [4] L. Novák, I. Müllerová: Single Electron Response of the scintillator-light guide-photomultiplier detector. *J. Microsc.* (to be published)
- [5] Research was supported by FEI Czech Republic, Ltd.

A CHROMATIC AND SPHERICAL ABERRATION CORRECTED PEEM

M. Osterberg, and A. Khursheed

National University of Singapore, 4 Engineering Drive 3, Singapore 117576
e-mail: eleombj@nus.edu.sg

The photoemission electron microscope (PEEM) is a valuable tool for surface scientists, but it suffers from limited spatial resolution of some 20-50 nm in practice, depending on the excitation source [1]. This limitation stems mainly from chromatic aberration of its cathode lens. Time-of-flight (TOF) based chromatic aberration correction for PEEM, whereby the source excitation is pulsed and electrons made to disperse spatially in a drift-tube, according to their take-off energy, before dynamically being focused using a time varying electrode voltage, has been proposed by Schonhense [1], and Khursheed [2], with preliminary results shown by Schonhense.

In addition to the chromatic aberration, a PEEM system will also suffer from spherical aberration. This paper looks at the possibility of simultaneously correcting the chromatic aberration according to Khursheed's scheme, and the spherical correction using an electrostatic equivalent to the magnetic hexapole corrector invented by Rose [3]. Computer simulations are carried out based upon several different methods of direct ray tracing. For the correction of chromatic aberration, a combined cathode lens/drift tube design is proposed, as depicted in Fig. 1. Electrons are accelerated from the specimen by the extraction electrode to a few hundred eV, before being slowed down to 20 eV at the entrance of the drift-tube. The first electrode after the drift tube will then accelerate the electrons back to a few hundred eV, and this is also the electrode that will be dynamically varied for the correction. The next electrode is used to trim the output direction of electrons before they are fed into the hexapole corrector, which requires electrons to enter parallel to the optical axis. The last electrode sits at ground potential and thus achieves final acceleration to the desired beam energy.

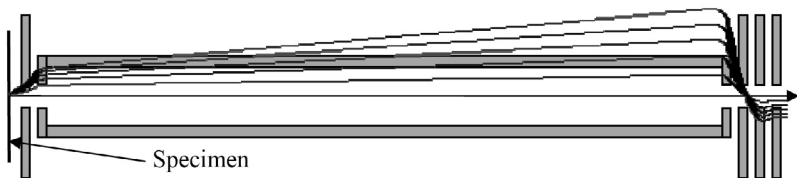


Fig. 1. Proposed cathode lens/drift tube for dynamic chromatic aberration correction.

Spherical aberration was investigated separately, preliminary results have been obtained for the cathode lens/drift tube, with trajectories shown in Fig. 2. More detailed results will be given at the conference. For the hexapole corrector, both on- and off-axis aberrations have been investigated using a conventional 3-electrode cathode lens, see Fig. 2, and for a particular energy, the on-axis spherical aberration can be brought down to around 10nm for an initial take-off angle of 0.5rad. However, problems crop up due to the initial spread in take-off energy, which results in electrons generally not being parallel

as they exit the cathode lens, thereby reducing the efficiency of the correction significantly. Initial off-axis aberrations spot diagram simulation results are shown in Fig. 3, as expected, correction is most effective close to the axis.

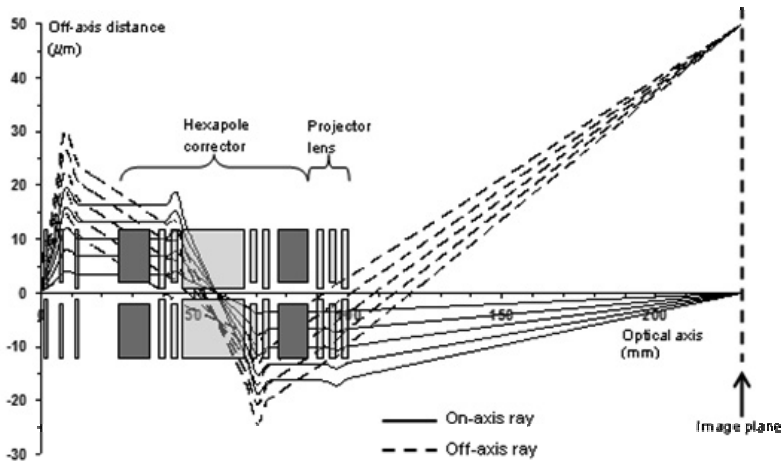


Fig. 2. The hexapole corrector incorporated into the PEEM column. Here, the system has been set for a final 10 times magnification.

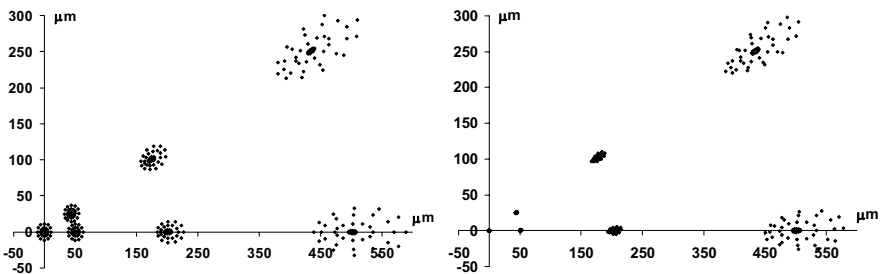


Fig. 3. Simulated spot diagrams for on- and off-axis spots: (a) show spots without hexapole corrector action. (b) shows corrector activated. Note that the spots have been enlarged 20 times for clarity.

Simulation results combining the chromatic and spherical aberration correction will be presented at the conference. The main challenges are expected to be in the tuning of the drift tube electrodes in order to find suitable electron exit conditions to feed into the hexapole corrector, and at the same time be able to cancel chromatic aberrations of lenses as well as the hexapole corrector itself.

References

- [1] A. Khursheed, *Optik* 113 (2002) 505
- [2] G. Schonhense, and H. Spiecker, *J. Vac. Sci. Technol. B*20(6) (2002) 2526
- [3] H. Rose, *Optik* 85 (1990) 19

MODERN APPLICATIONS OF THE ANCIENT WIEN FILTER

E. Plies

Institut für Angewandte Physik, Universität Tübingen, Auf der Morgenstelle 10,
D-72076 Tübingen, Germany, e-mail: erich.plies@uni-tuebingen.de

The Wien filter was first mentioned in 1897 [1], 30 years before Busch [2] demonstrated that the axially symmetric field generated by a coil acts on electrons like a convergent lens in light optics. Herzog [3] explained that the Wien filter (WF) focusses one-directionally just as a cylindrical lens. Since the WF has a straight optic axis but a dispersion, it acts like a direct-vision prism, too. Though the velocity dispersion of the WF is comparatively low it is often preferred to magnetic or electrostatic prisms due to the experimental advantage of its straight axis. Nevertheless, the WF has second-order aberrations which are typical for elements with dipole fields. Additionally, the possible hexapole components of the crossed inhomogeneous electrostatic and magnetic fields of the WF contribute to the second-order aberrations. – The WF can even act like a round lens for electrons with the nominal velocity ($v=E_x/B_y=\Phi_{1C}/\Psi_{1S}$) if the crossed fields have an appropriate electric and/or magnetic quadrupole component.

Since Legler [4] the Wien filter was already used as an electron monochromator in the 1960s. Boersch et al. [5,6] employed one WF as a monochromator and a second WF as an energy analyser. Andersen and Le Poole [7] used a double WF as a high resolution analyser and Seliger [8] applied the WF as a mass separator for ions. To separate primary electrons (undeflected) and secondary electrons (deflected) the Wien filter was used by many authors [9-16]. In [11,13,15-16] a second WF is additionally installed to precompensate for the dispersion and the second-order aperture aberrations.

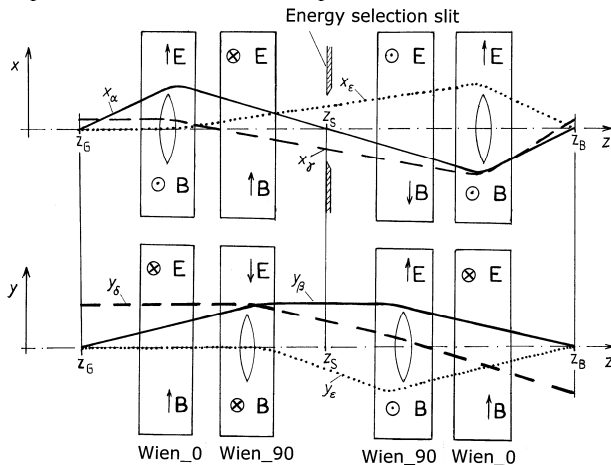


Figure 1: Scheme of an electron monochromator consisting of „normal“ Wien filters (Wien_0) and rotated Wien filters (Wien_90) together with the computed fundamental rays.

x_α, y_β = axial rays;

x_γ, y_δ = off-axial rays;

x_ϵ, y_η = dispersion rays.

The total length of the computed monochromator is $z_B - z_G = 320\text{mm}$.

The recent high interest in the ancient WF is mainly as an electron monochromator [17-20], but also as an imaging energy filter [21-23] or as a corrector for the chromatic and the spherical aberration [24-26]. The correct matching of the Wien condition demands that the electrostatic and the magnetic dipole fields have the same axial distribution. This problem was treated by many authors [13,16,18-23,27-30] and usually electrodes and pole pieces are made

from the same (conductive) ferromagnetic material. To correct some second-order aberrations or to make a system dispersion-free, two WF [18-19,30-31] or four WF [32-33] are used.

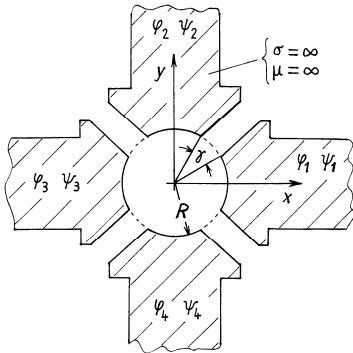


Figure 2: 4-pole element to generate the crossed fields of the Wien filters used in the systems of Fig. 1 and 3. For the „normal“ Wien filter (Wien_0) the scalar potentials are $\varphi_1=U_D$, $\varphi_2=0$, $\varphi_3=-U_D$, $\varphi_4=0$ and $\psi_1=0$, $\psi_2=NI_D$, $\psi_3=0$, $\psi_4=-NI_D$. For the rotated Wien filter (Wien_90) the potentials are rotated by 90° . – In the case of the mass filter of Fig. 3 the potential U_Q must be added to the first and the third electrode and $-U_Q$ to the second and the fourth electrode to generate a quadrupole field, and the high potential U_{it} is superimposed to all electrodes.

The novel and highly symmetric 4-WF-monochromator [20] is essentially different from [32-33], because it consists of two „normal“ Wien filters (E_x , B_y) and Wien filters which are rotated by 90° (E_y , $-B_x$), see Fig.1. This makes the optical calculation more difficult but such a system is covered by [34,35]. Using this general theory the program ABERW of Mebs Ltd., London, based on [36] was extended by H. Liu and the author for rotated WF including the related aberrations of second rank. Then the resulting code, ABERW2, was developed up to the aberrations of third rank [37] using algorithms from [35]. [38]

Table 1: Electric excitations of the symmetric 4-Wien-filter-system with $|M_x| = |M_y| = 1$.

WF = Wien filter, $A = 1084$ V, $a = 846$ V, $B = 1221$ V, $b = 592$ V.

System number	1	2	3	4	5	6	7	8	9	10	11	12	13	14	15	16
WF1 (Wien_0)	A	A	A	A	a	a	a	a	A	A	A	A	a	a	a	a
WF4 (Wien_0)	A	A	A	A	a	a	a	a	-A							
WF2 (Wien_90)	-b	b	-B	B	-b	b	-B	B								
WF3 (Wien_90)	b	b	B	B	b	b	B	B	b	b	B	B	b	b	B	B

4-pole elements as shown in Fig. 2 are sufficient to generate the crossed fields of the 4-WF-monochromator. The non-vanishing hexapole component of such an element is given in the main field of the first WF (Wien_0) by $\Phi_{3C} = c \Phi_{1C} / R^2$ with $\Phi_{1C}(z) = -E_x(0,0,z)$ and constant $c = 0.33 - 0.27$ for a gap angle γ between 15° and 45° . There is a similar formula for the magnetic hexapole component Ψ_{3S} and also for Φ_{3S} and Ψ_{3C} in the case of the rotated WF (Wien_90). However, in this case the hexapole components can be accepted because the second-order aperture aberrations are corrected in the image plane z_B by the symmetry of fields and rays in the x - z and in the y - z section, see Fig. 1. Regarding 1 keV electrons, the x -dispersion in the energy selection plane z_S is $36 \mu\text{m}/\text{V}$ and the lateral magnification $M_x = -1.66$. Furthermore, if we assume a beam size of $1 \mu\text{m}$ in the object plane z_G and an aperture of 1.5 mrad the aperture aberration in x -direction is $2.1 \mu\text{m}$ in the plane z_S and the energy width of the electrons can be reduced to 0.1 eV using a slit width of $3.5 \mu\text{m}$. The y -dispersion in z_S is only 26% of the x -dispersion and it is neither usable nor disturbing. If we characterize a WF by the parameter $\lambda = \frac{1}{2} \Phi_{1C} / \Phi$ with $\Phi = U_B = 1$ kV = beam voltage this results in $\lambda = 49.4/\text{m}$ for the outer two WF which have the strongest excitation. One should mention that there are sixteen 4-WF-systems which deliver an 1:1 magnification, see Table 1. But all systems except number 1, 4 and 16 suffer from the fact that the dispersion does not vanish in the image plane z_B and/or the system is telecentric, i.e. there is no intermediate image in the midplane z_S ,

neither astigmatic nor stigmatic. System 4 has a stigmatic image in the midplane which is a disadvantage regarding Coulomb interactions. For system 16 the useful dispersion in the plane z_S is only 42% of the dispersion of system 1. Besides, system 1 (shown in Fig. 1) has the lowest maximum excitation compared to system 4 and 16. Therefore type 1 is best suited as an electron monochromator and a corresponding system is currently being built.

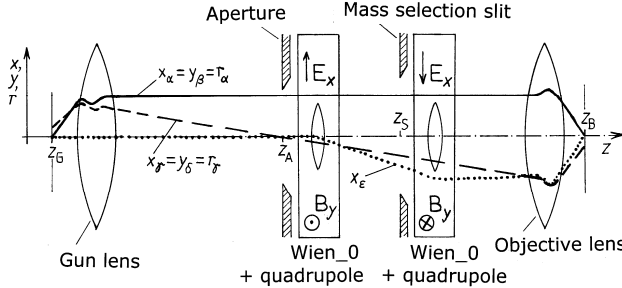


Figure 3: Scheme of a mass filter with entirely astigmatism-free Gaussian rays. Axial kinetic potentials:
 $\Phi(z_G)=3.5\text{kV}$;
 $\Phi(z_A)=\Phi(z_S)=U_{II}=8\text{kV}$;
 $\Phi(z_B)=2\text{kV}$.
 Length $z_B-z_G=453\text{mm}$.

Another possible application of the ancient Wien filter is a mass filter as proposed in Fig. 3. Due to the symmetry of fields and rays there is no energy and no mass dispersion in the image plane z_B . Here the two WF have the same orientation and again 4-pole elements are used to generate the crossed fields of the WF. But now an additional quadrupole component is generated by the applied potentials $\pm U_Q$ (see caption of Fig. 2) to give the WF the focussing behaviour of a round lens. Then the adequate condition $\Phi_{2C} = \Phi_{1C}^2 / (8 U_{II})$ for entirely astigmatism-free Gaussian rays yields the relation $U_Q \approx 0.08 U_D^2 / U_{II}$ for a gap angle $\gamma \leq 45^\circ$. Such a system guarantees $M_x = M_y$ and is more flexible than the system [31] composed of two classical WF (without Φ_{2C}) and a separate quadrupole lens between the two WF.

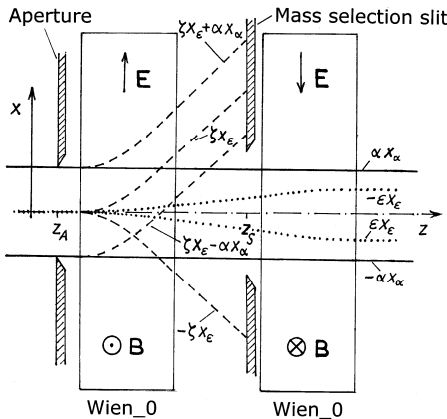


Figure 4: Mass filtering principle showing the axial ray bundle $\pm\alpha x_\alpha$ of nominal mass and nominal energy (—), the energy dispersion rays $\pm\epsilon x_\epsilon$ (.....) and the mass dispersion rays $\pm\zeta x_\zeta = \pm\zeta x_\epsilon$ (-----) together with the mass dispersion ray bundle $\zeta x_\epsilon \pm \alpha x_\alpha$ (-.-.-.-). For an 8 keV Ga^+ ion beam $\epsilon = \Delta E/E = \Delta E/(eU_{II}) = \pm 6 \cdot 10^{-4}$ and $\zeta = \Delta m/m = 2.9 \cdot 10^{-2}$ are valid.

The focussing voltages of the gun and objective lens of the focussed ion beam system shown in Fig. 3 must be weaker only by less than 1% when it is operated with the mass filter because the focussing effect of the WF is rather weak. For both modes the rays are telecentric ($x_\alpha'(z_S) = 0$) and source and image positions are fixed. Here, the parameter λ of the WF has the value $\lambda = \Phi_{1C} / (8^{1/2} U_{II}) = 5.0/\text{m}$ which is one order of magnitude weaker than in the case of the 4-WF-monochromator.

In the WF the fundamental ray x_ζ of the mass dispersion differs from the fundamental ray x_ϵ of the energy dispersion only by the sign ($x_\zeta = -x_\epsilon$) which is already considered in Fig. 4.

This fact directly follows from the relation $\Delta v/v = \frac{1}{2} \Delta E/E - \frac{1}{2} \Delta m/m$. As can be seen from Fig. 3 and 4 the mass filtering is not done (as usual) in an intermediate image. Anyhow, the mass filtering works fine for an aperture $\alpha \leq \frac{1}{2} \zeta x_e(z_s) / x_a(z_s)$ with $\zeta = \Delta m/m$ (see Fig. 4). Using a Ga^+ ion beam with two isotopes (60.2% of ^{69}Ga and 39.8% of ^{71}Ga) this yields $\alpha \leq 3$ mrad (diaphragm diameter $\leq 145 \mu\text{m}$) for the chosen optical parameters. For a common Ga^+ emitter this results in a total Ga^+ ion beam current of (at least) 400 pA directly before and 240 pA of pure $^{69}\text{Ga}^+$ behind the mass filter. Moreover, selecting the elements of an alloy liquid metal ion source which is of high interest in nanotechnology is even easier.

- [1] W. Wien, *Verhandl. der physikal. Ges. zu Berlin* **16** (1897) 165.
- [2] H. Busch, *Arch. Elektrotech.* **18** (1927) 583.
- [3] R. Herzog, *Z. Physik* **89** (1934) 447.
- [4] W. Legler, *Z. Physik* **171** (1963) 424.
- [5] H. Boersch, J. Geiger, H. Hellwig, *Phys. Letters* **3** (1962) 64.
- [6] H. Boersch, J. Geiger, W. Stickel, *Z. Physik* **180** (1964) 415.
- [7] W.H.J. Andersen, J.B. Le Poole, *J. Phys. E: Sci. Instrum.* **3** (1970) 121.
- [8] R.L. Seliger, *J. Appl. Phys.* **43** (1972) 2352.
- [9] T. Otaka, Y. Nakaizumi, K. Kuroda, *Int. Patent Appl. Number PCT/JP85/00170* (1985).
- [10] E. Plies, *Nucl. Instrum. Meth. Phys. Res. A* **298** (1990) 142.
- [11] W.D. Meisburger, A.D. Brodie, A.A. Desai, *J. Vac. Sci. Technol. B* **10** (1992) 2804.
- [12] M. Sato, H. Todokoro, K. Kageyama, *Proc. of SPIE*, Vol. **2014** (1993) 17.
- [13] D. Pejchl, I. Müllerová, L. Frank, V. Kolařík, *Czechoslovak J. of Physics* **44** (1994) 269.
- [14] K. Tsuno, *Ultramicroscopy* **55** (1994) 127.
- [15] S. Beck, E. Plies, B. Schiebel, *Nucl. Instrum. Meth. Phys. Res. A* **363** (1995) 31.
- [16] M. Kienle, E. Plies, *Nucl. Instrum. Meth. Phys. Res. A* **519** (2004) 325.
- [17] H.W. Mook, P. Kruit, *Ultramicroscopy* **81** (2000) 129.
- [18] M. Mukai et al., *Proc. of ICEM 15, Durban, 2002, Vol. III*, 321.
- [19] M. Tanaka et al., *Microsc. Microanal.* **8**, Suppl.2 (2002) 68.
- [20] E. Plies, J. Bärtle, *Microsc. Microanal.* **9**, Suppl.3 (2003) 28.
- [21] H. Rose, *Optik* **77** (1987) 26.
- [22] K. Tsuno, *Rev. Sci. Instrum.* **64** (1993) 659.
- [23] G.K.L. Marx, V. Gerheim, G. Schönhense, *J. Electr. Spectr. Rel. Phenom.* **84** (1997) 251.
- [24] H. Rose, *Optik* **84** (1990) 91.
- [25] T. Steffen et al., *Proc. of EUREM 12, Brno, 2000, Vol. III, I 151*.
- [26] S.A.M. Mentink, T. Steffen, P.C. Tiemeijer, *Inst. of Physics Conf. Ser.* **168** (2001) 147.
- [27] T.T. Tang, *Optik* **74** (1986) 51.
- [28] K. Tsuno, J. Rouse, *J. Electron Microsc.* **45** (1996) 417.
- [29] B. Lencová, I. Vlček, *Proc. of EUREM 12, Brno, 2000, Vol. III, I 87*.
- [30] G. Martínez, K. Tsuno, *Ultramicroscopy* **100** (2004) 105.
- [31] J. Teichert, M.A. Tiunov, *Meas. Sci. Technol.* **4** (1993) 754.
- [32] Y. Kawanami et al., *Nucl. Instrum. Meth. Phys. Res. B* **37/38** (1989) 240.
- [33] X.D. Liu, T.T. Tang, *Nucl. Instrum. Meth. Phys. Res. A* **363** (1995) 254.
- [34] E. Plies, D. Typke, *Z. Naturforsch.* **33A** (1978) 1361 and **35A** (1980) 566.
- [35] E. Plies, *Ultramicroscopy* **93** (2002) 305.
- [36] H. Liu, *Proc. of SPIE*, Vol. **3777** (1999) 92.
- [37] K. Marianowski, E. Plies, *Proc. of EUREM 14, Aachen, 2008*, accepted.
- [38] I kindly acknowledge the help of Mebs Ltd. in general and Haoning Liu in special.

HIGH-ORDER FIELD DERIVATIVES FOR COMPUTATION OF ABERRATIONS

T. Radlička

Institute of Scientific Instruments, AS CR Královopolská 147, 612 64 Brno, Czech Republic
radlicka@isibrno.cz

The aberrations are important optical characteristics of the electron optical system. The third order of aberrations has been described [1] and the calculation of the fifth order aberrations is an object of recent research. This contribution is focused on marginalized part of these calculations – the calculation of analytical expansion of the field near the axis.

It is well know that the field in real electron optical devices cannot be calculated analytically, but it is a numerical solution of Laplace equation [1]. The numerical methods are mostly based on the Finite Elements Method (FEM), the results of such a calculation are the values of potential at nodal points of the mesh. However, this form of the field cannot be used in methods that lead to aberration integrals or in Differential Algebra method, these methods require the field in form of the an analytical expansion into powers of distance from the optical axis, e.g. in case of rotationally symmetric electrostatic potential:

$$\Phi(z, r) = \sum_{n=0}^{\infty} \frac{1}{(n!)^2} \left(-\frac{r^2}{4} \right)^n \phi^{(2n)}(z).$$

Hence, for the calculation of the analytical expansion we need the derivatives of the axial potential known only in a discrete set of points. The paper will summarize possible methods and compare their results on an example of unipotential electrostatic lens.

The first method, implemented by Munro [2], is based on the expansion of the axial function into a series of Hermite functions. The second method was suggested by Berz [3] and used by Liu [4]. It is based on the discrete Gaussian wavelet transformation. The third method was suggested by Venturini and Dragt [5] and it comes from the properties of the field as a solution of Laplace equation. It requires the field on the surface of infinite cylinder with the axis coinciding with axis z and the fulfilled Laplace equation inside the cylinder.

The last requirement is often too strong, therefore using Green theorem we generalized the approach of Venturini and Dragt on a general rotational symmetric volume V . Let us assume that the axis of V coincides with axis z . In r, z coordinates the border of V is formed by the curve ζ . If Laplace equation is fulfilled inside V , the n^{th} derivative of the axial potential can be found in form

$$\phi^{(n)}(z) = \frac{1}{4} \int_{\zeta} \left(\frac{\partial^n}{\partial z^n} \left(\frac{1}{\sqrt{(z-z')^2 + r'^2}} \right) \frac{\partial \Phi(r', z')}{\partial \mathbf{n}'} - \Phi(r', z') \frac{\partial^n}{\partial z^n} \frac{\partial}{\partial \mathbf{n}'} \left(\frac{1}{\sqrt{(z-z')^2 + r'^2}} \right) \right) d\zeta'$$

where \mathbf{n} is outer normal of surface of V the rotation symmetric surface, i.e. the value of potential and its normal derivative must be known on the surface of V .

We compare the results of the three approaches on the example of a simple unipotential electrostatic lens [4] (figure 1). The mesh was chosen such that all vertical and horizontal mesh lines were equidistant with mesh step $5 \mu\text{m}$; the mesh contains 1601 vertical and 501 horizontal mesh lines. The field was calculated in program EOD [6]. The voltage ratio between the outer and central electrode was 6. The lens is symmetric with respect to the plane $z = 0$, the border of the mesh was put at 8 mm, sufficiently far from the center of the lens. As a criterion for the quality of expansion we show in figure 2 the relative difference of

potential from the analytical expansion and from the numerically computed values in the distance $r = 0.1$ mm from the optical axis.

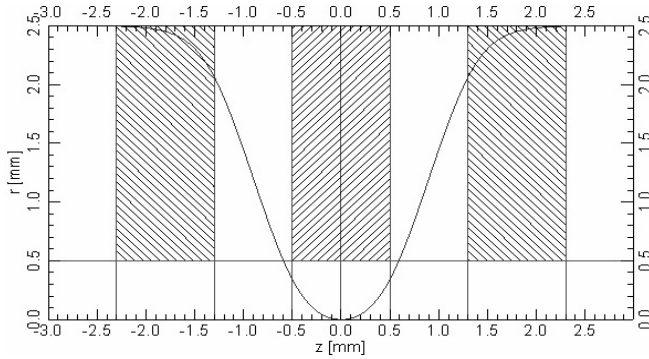


Fig. 1 The design of unipotential electrostatic lens with computed axial potential $V_{\min} = 1.198$ V, $V_{\max} = 6$ V.

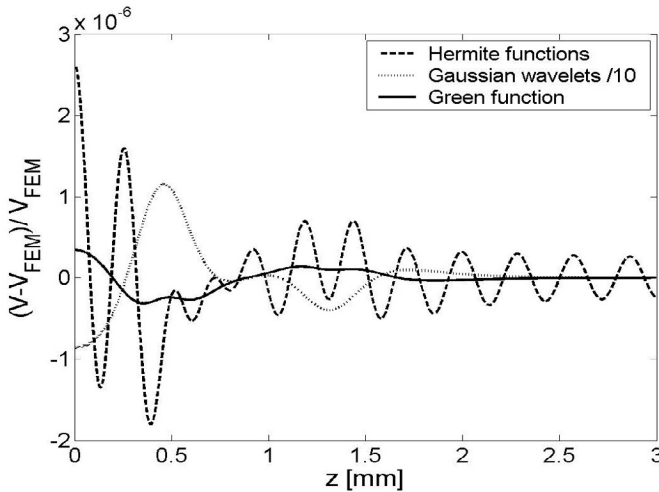


Fig. 2 The relative error of the potential from of the analytical expansion and from the numerically computed values in $r = 0.1$ mm.

References:

- [1] P.W. Hawkes, E.Kasper: Principles of Electron Optics. *Academic Press, London* (1989)
- [2] L.Wang,J.Rouse,H.Liu,E.Munro,X.Zhu, *Microelectron. Eng.* **90**, 73 – 74, (2004)
- [3] M. Berz, *Adv. Imaging Electron Phys. Suppl* **108**, (1999)
- [4] Z. X. Liu, *Ultramicroscopy* **106**, 220 – 232, (2006)
- [5] M. Venturini, A.J. Dragt, *Nucl. Inst. and Methods in Phys. Res. A* **427**, 387 – 392, (1999)
- [6] B. Lencová and J. Zlámál, *Microsc. Microanal.* **13**, Suppl. 3, 2–3, (2007)

A MINIATURIZED ELECTRON OPTICAL COLUMN WITH AN ELECTROSTATIC-PERMANENT MAGNETIC OBJECTIVE LENS

C. Rochow, T. Ohnweiler and E. Plies

Institute of Applied Physics, University of Tübingen, Auf der Morgenstelle 10,
D-72076 Tübingen, Germany
e-mail: christoph.rochow@uni-tuebingen.de

We present simulation results of a miniaturized electron optical column applying an electrostatic-permanent magnetic objective lens, thus reducing the chromatic aberration. The system consists of an electron emitter, two electrostatic three electrode lenses, a scintillator-photomultiplier detector, an electrostatic scanning and double-deflection unit and a permanent magnetic snorkel lens.

The system (Fig. 1) currently being built is about 85 mm in height. Condenser (Fig. 2) and objective lens (Fig. 3) are manufactured from conventional platinum apertures [1]. In the

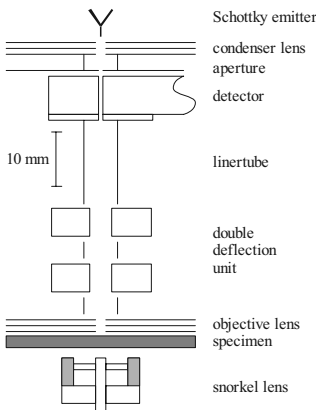


Figure 1: Schematic system overview

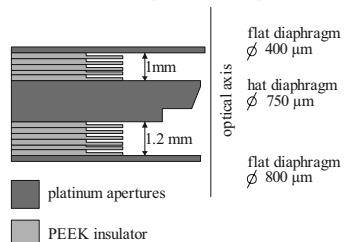


Figure 2: Schematic of the condenser lens

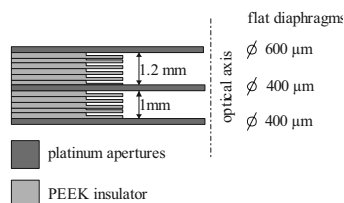


Figure 3: Schematic of the objective lens

intermediate region between the two lenses, the detection system and the double-deflection unit have been placed. In this intermediate region the primary electron beam can be varied between converging and diverging mode. The secondary electrons (SE) are accelerated through the objective lens towards the in-column detector, which is set to a potential of up to 10 kV relative to the sample. This high potential makes the SE detectable by a scintillator and increases the immersion ratio of the condenser and objective lens thus decreasing the aberrations. The adjustable permanent magnetic snorkel-lens (Fig. 4) is similar to the add-on lens described in [2]. In conjunction with the electrostatic objective lens it

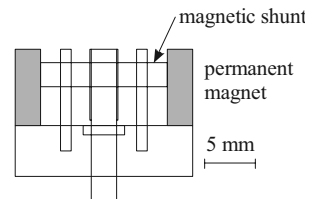


Figure 4: Schematic of the snorkel lens

further decreases the chromatic aberration coefficient. This is most important for low energy systems. Because of the magnetic field at the sample, high care must be taken during simulation of the SE-trajectories.

The system has been optimised for landing energies of less than 1 keV, a working distance of 1 mm and no electric field at the sample. Increasing the electric field strength at the sample further decreases the aberrations and increases SE-detection-efficiency but also restricts possible applications.

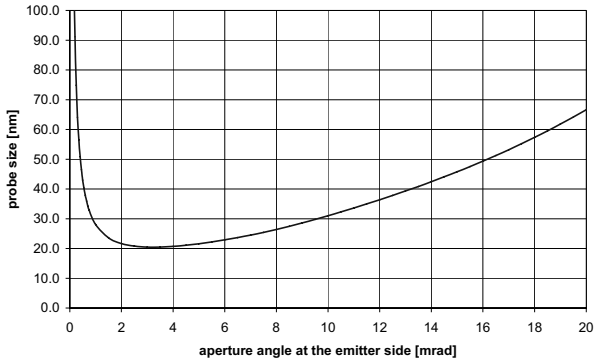


Figure 5: Achievable probe size for a final beam energy of 1 keV

Simulations are presented for beam energies of 1 keV and below. The condenser and objective lens are assumed to be operated in internal deceleration mode. Because of the high electric field strength the internal acceleration mode cannot be realized even if it yields better theoretical results. Assuming a virtual source size of 20 nm, an energy width (FWHM) of 1.2 eV and no electric field at the sample, a probe size of less than 30 nm is achievable (Fig. 5).

The SE leaving the sample are accelerated to an energy of up to 10 keV through the objective lens towards the scintillation detector. Placing the scintillator with a 1 mm bore 30 mm above the sample and assuming a cosine distribution for the starting angles as well as a Maxwellian energy distribution with a maximum at 2 eV, calculations show a collection efficiency of 30% up to 70% for starting energies between 0.5 eV and 10 eV depending on the electric field strength at the sample.

All field calculations and simulations of trajectories were carried out with the program Electron Optical Systems (EOS) of E. Kasper.

The presented simulations for a miniaturised low-energy electron optical column show that a resolution of 30 nm is achievable. The possibility of in-column detection of the secondary electrons has been confirmed by simulation of their trajectories as well as by calculating the collection efficiency.

[1] C.-D. Bubeck et al., Nucl. Instrum. Meth. Phys. Res. **A 427** (1999) 104.

[2] A. Khursheed, N. Karupiah and S. H. Koh, Scanning **23** (2001) 204.

THE ROUTE TOWARDS SUB-Å LOW-VOLTAGE ELECTRON MICROSCOPY

H. Rose

Institute of Applied Physics, TU Darmstadt, Hochschulstrasse 6, 64289 Darmstadt, Germany
E-mail: harald.rose@physik.tu-darmstadt.de

The optimum electron microscope depends strongly on the material of the object and on the properties to be investigated. Radiation damage is the fundamental limitation for the attainable specimen resolution. Solid objects, such as metals, are primarily damaged by atom displacement resulting from knock-on collisions of the electrons with the atomic nuclei. Damage resulting from ionization and/or electronic excitations is generally negligibly small for these objects. Because the closely packed atoms in solid materials form electronic band structures, an ejected electron is immediately replaced by another electron.

The situation differs for biological material. The specimen resolution of these objects is limited by the maximum tolerable dose because the inelastic scattering events destroy chemical bonds by ionization. The missing electron may be replaced within a sufficiently short time by another valence electron, as it is the case for the π -electrons of aromatic molecules and of carbon nanotubes. If the binding electron is not replaced within a period of about 10 femto-seconds, the bond will very likely break and destroy the structure because the strong electric forces rearrange the positions of the atoms [1]. This damage is especially large for aliphatic molecules whose binding electrons do not form a band structure.

In order to displace an atom from its position of rest by a knock-on collision, the transferred energy must be larger than the displacement energy E_d of the atom. This energy depends strongly on the direction of the impact and on the position of the atom within the object because the neighbor atoms will take some fraction of the transferred energy. The maximum transferred energy for an elastic head-on collision of an electron with an atom is $E_m \approx 2(1 + \gamma)eUm / M$. Here U , m , M and γ denote the accelerating voltage, the rest mass of the electron, the mass of the atom and the relativistic factor, respectively. For carbon and non-relativistic electrons we obtain $E_m \approx 1.6 \times 10^{-4} eU$. The binding energy E_d of carbonaceous material, such as graphite or carbon nanotubes, is about 10eV. To avoid atom displacement for these materials, the accelerating voltage must be lower than about 60kV.

In order to achieve sub-Å resolution for solid objects at such low acceleration voltages, we must correct the chromatic and the spherical aberration of the imaging system and reduce the information limit below 1Å. This mandatory reduction poses very demanding requirements on the electric and mechanical stabilities in the case of low accelerating voltages. Electron spectroscopic imaging with an energy resolution below 0.2 eV requires the incorporation of a monochromator and a high-performance imaging energy filter into the electron microscope.

The proposed Sub-Angstrom Low-Voltage Electron microscope (SALVE) project utilizes a novel achromatic aplanat consisting of a coma-free magnetic round lens and a corrector compensating for the spherical and the chromatic aberration. To enable the correction of these aberrations, each of the two hexapoles of the standard hexapole corrector is replaced by a symmetric telescopic multipole quintuplet. Within these elements electric and magnetic quadrupole fields are excited, which produce an appropriate astigmatic path of rays and compensate for the chromatic aberration of the round lenses. Additional octopole fields eliminate their spherical aberration without introducing off-axial coma.

The requirements imposed on the microscope differ for solid specimens and biological objects. The maximum tolerable dose D of the incident electrons determines the achievable specimen resolution limit of organic objects

$$d_s = \sqrt{d_i^2 + \frac{(S/N)^2}{C^2 D}}.$$

This limit depends primarily on the image contrast C and on the signal to noise ratio S/N , which is necessary to discriminate in the image an object detail from the noise. The specimen resolution approaches the instrumental resolution $1/d_i = \sin \theta_0 / (0.61\lambda)$ in the limit $D \rightarrow \infty$. The minimum value for S/N is about 5. Since the tolerable dose is also fixed, we can only decrease the specimen resolution limit by increasing the contrast. For objects consisting of light atoms the phase contrast is dominant. We obtain highest contrast and maximum S/N at the Gaussian image plane if we eliminate the axial aberrations and shift the phase of the non-scattered wave by $\pi/2$. In this negative contrast mode, the phase contrast and the amplitude contrast produced by the elastically and inelastic scattered electrons add up with the same sign. In the ideal case, atoms or atom clusters appear as bright spots superposed on the uniform background intensity. To realize this optimum case, we must (a) introduce a micro-phase plate at the diffraction plane or at an image of this plane [2] and (b) incorporate a corrector compensating for the chromatic and spherical aberrations of all lenses of the microscope because the chromatic aberration of magnification of the individual lenses add up independently of the magnification of the intermediate image in front of each lens. The maximum achievable phase contrast in the image of a single atom with atomic radius $a \approx 0.05Z^{-1/3}$ nm is $C_p \approx Za^2 / 8\beta d_i^2$, where Z denotes the atomic number and $\beta = v/c$ the ratio of the velocity of the electron to that of light. Hence, we achieve maximum phase contrast in the case of atomic instrumental resolution and low accelerating voltages.

The use of the inelastic scattered electrons will greatly enhance the contrast if the object is appreciably thicker than the inelastic mean free path length, as it usually happens for biological objects embedded in ice. In this case, many electrons are scattered more than once. These electrons may undergo two or more inelastic scattering events or one inelastic and one elastic scattering process. Inelastic scattering lowers the elastic scattering amplitude reducing the phase contrast. Fortunately, if an inelastic scattered electron undergoes an additional elastic scattering process, the scattered part of the wave is coherent with its non-scattered part. However, the resulting image will be blurred by chromatic aberration. In order to enhance contrast and specimen resolution, we must compensate for the chromatic aberration as well.

Our considerations show that low voltage and the correction of chromatic and spherical aberration are mandatory to achieve optimum conditions for the imaging of organic objects, nanoparticles, and ceramics. In order to achieve highest contrast a micro-phase plate is necessary which shifts the phase of the non-scattered wave by $\pi/2$

References

- [1] Scherzer O., 1970, *Berichte der Bunsen Gesellschaft Phys. Chem.* **74**, 1154-1167
- [2] Schultheiss K., Perez-Fillard F., Barton B., Gerthsen D. and Schroeder R., 2006, *Rev. Scient. Instr.*, **77**, 033701

AN ADVANCED ION GUIDE FOR A DEDICATED SIMS

B. Schröppel^{1,*}, A. Brekenfeld² and E. Plies¹

¹Institute of Applied Physics, University of Tübingen, Auf der Morgenstelle 10,
D-72076 Tübingen, Germany

²R & D, Ion Trap Mass Spectrometry, Bruker Daltonik, GmbH, Fahrenheitstrasse 4,
D-28359 Bremen, Germany

*e-mail: birgit.schroepfel@uni-tuebingen.de

For the study of cellular structures of biological cells in thick samples, scanning electron microscopy is a well established method. Until now, however, a technique for these biological systems to simultaneously detect the chemical composition as well as the distribution of certain molecules beyond the detection and mapping of elements is still missing. To meet these requirements for analysis of biological samples, the development of an imaging cryo-secondary ion mass spectrometer (SIMS) based on a CrossBeam® electron-ion probe, an ESI (electrospray ionization) ion trap mass spectrometer and an “in situ” freeze fracture facility was object of a BMBF Verbundprojekt [1].

Part of this project was the development of an ion optical system connecting the electron-ion probe and the ion trap mass spectrometer and hence transferring the secondary ions from the sample to the mass spectrometer. Main focus for this optical transfer unit is to achieve high acceptance and, in addition, precise injection of the secondary ions into the ion trap. Therefore, the ion optical transfer system is composed of two parts. Within the first part, secondary ions are extracted from the sample by the electric field of an electrostatic multi-tubular lens and focused on the entrance aperture of the second part. The second part of the ion optical transfer system consists of two radio frequency octupoles that have been taken over from the original configuration of the ion trap mass spectrometer. By confining the ions radially by the pseudo potential [2] resulting from the radio frequency electrical field, the octupoles act as an ion guide. First ion optical and experimental results were already published [3].

Going on from these first results, further simulations are carried out to further enhance the performance of the ion optical transfer system. Within this contribution, new ion optical results regarding both parts of the optical transfer unit obtained from these ion optical simulations with the software package SIMION 8 [4] will be presented.

Regarding the radio frequency octupoles, the transmission characteristic has to be determined. For this purpose, simulations are carried out using direct ray tracing for common starting parameters of the ions averaged over a half cycle of the radio frequency field. Thus the transmission (defined as fraction of ions transferred through the device) of one radio frequency octupole as a function of the starting energy perpendicular to the optical axis can be obtained for different masses and different amplitudes of the radio frequency voltage (Fig. 1).

Additionally, the corresponding transmission curves were calculated by applying the adiabatic approximation according to [5]. Thereby, the pseudo potential of an ideal radio frequency octupole is examined taking into account the adiabatic parameter (Fig. 1).

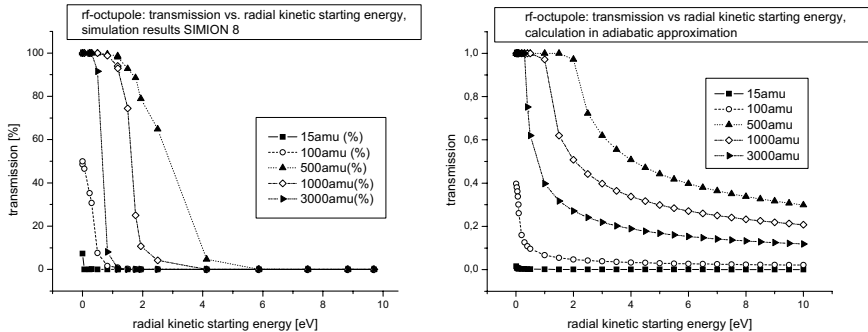


Figure 1: Transmission versus radial kinetic starting energy for a radio frequency octupole with frequency and amplitude of the rf-voltage given, on the left by direct ray tracing with SIMION, on the right by calculating the transmission within the adiabatic approximation; deviations are obvious particularly for higher energies.

With respect to the results obtained by these two methods the electrostatic multi-tubular lens (Fig. 2) is analysed again with respect to its optical properties and to phase space considerations. The intention is to find an ideal set of parameters for extraction of the secondary ions from the sample and the injection of the secondary ions by the electrostatic lens in the radio frequency octupoles and so to further enhance the transmitted current and hence the sensitivity of the SIMS. Therefore, the disc of least confusion of the electrostatic multi-tubular lens is determined and the corresponding phase space diagram is evaluated with respect to the following radio frequency octupoles taking into account the spatial and angular distribution of the secondary ions on the sample.

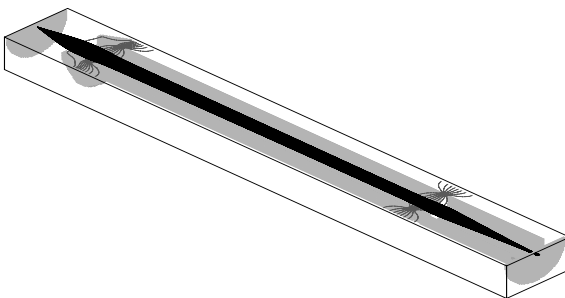


Figure 2: Simulation of the electrostatic multi-tubular lens with SIMION; trajectories in black, equipotential lines in dark grey, electrodes in light grey.

- [1] Support by the BMBF (project 13N8652-55) is gratefully acknowledged.
- [2] H.G. Dehmelt, Radiofrequency spectroscopy of stored ions I: Storage, in D.R.Bates (Ed.), *Advances in Atomic and Molecular Physics*, Vol.3, Academic Press, NY, 1967, 53-72.
- [3] B. Schröppel, E. Plies, C. Burkhardt, A. Brekenfeld, U. Zeile, P. Gnauck, *Proc. of MC 2007, Saarbrücken, 2007*, p.16.
- [4] SIMIONTM, Scientific Instrument Services, Inc. Ringoes, NJ 08551, USA.
- [5] D. Gerlich, *Inhomogeneous rf-fields: a versatile tool for the study of processes with slow ions*, *Advances in chemical physics LXXXII*, John Wiley and sons, NY, 1992, 1-176.

SIMULATIONS OF SPACE-CHARGE PHENOMENA IN ION TRAPS AND TOF MASS SPECTROMETERS WITH THE USE OF FMM

M.Sudakov

Ryazan Radio-Engineering Academy, Gagarina, 59/1, Ryazan, Russia, 390005

Space charge (SC) phenomena in ion traps (IT) and time-of-flight (TOF) mass spectrometers are very different and significant. At the same time they are poorly investigated and reported. Main problem of SC simulations in charged particle optics (CPO) is an enormous computation time required for realistic simulations. In order to compute Coulomb interaction for N particles using direct method one requires $N*(N-1)/2$ computations of field vector. Hence computation effort grows proportional to the square of number of particles. To solve this problem an approximate method of Coulomb force computation were developed by Barns and Hutt [1]. This method is similar to Fast Multipole Methods (FMM) of Greengart [2], but much simpler. The time required for Coulomb force computation by FMM scales as $N*\text{Log}(N)$. As a result simulations with several thousand charged particles become feasible with modern desk-top computers.

The method of Barns&Hutt was recently implemented in a CPO code SIMAX. New simulation tool was used to address problems of space-charge interactions in radio-frequency (RF) ion traps and in TOF mass spectrometers of different configuration. Results of those simulations together with comparison of simulation speed and accuracy for conventional Coulomb method and FMM will be given in present report.

For RF ion traps a simple theory of equilibrium ion cloud at low temperature is developed. According to this theory cloud of ions of similar mass-to-charge ratio (m/z) creates an ion crystal of constant charge density in the centre of trap. Size and shape of the cloud is investigated using theory and simulations. It is shown that size of the cloud scales as $1/3$ power of the total cloud charge. Sometimes in simulation a method of charge factor (CF) is used. Such simulations are not realistic and may lead to unphysical phenomena. Effect of CF on cloud size is also investigated. When ions of different m/z are collected within the trap at the same time heavy ions are pushed out of the trap centre where small ions reside. Collisions with buffer gas may destroy such segmentation at sufficiently high temperatures. Simulations of this kind together with measurements of critical temperatures will be presented.

In practical mass spectrometry ion traps are used for selection of ions with specific m/z by rejection of other ions towards electrodes (precursor ion isolation). A complicated excitation signals SWIFT are used for this purpose. Those signals are a mixture of harmonics at resonance frequencies of all ions except ions of wanted m/z . SC interactions introduce limitations of isolation accuracy due to interactions of precursor ions with ions of close m/z . SC limitations of such isolation method are investigated in present report.

Requirements for modern TOF mass spectrometers are very high. Resolving power is over 20.000 together with mass accuracy of few parts per million (ppm) are typical. SC

interactions lead to unwanted peak shifts and peak widening, which results in the loss of mass accuracy and resolution. Those effects become even more significant for a multi-turn TOF mass spectrometers where requirements of mass accuracy and resolution are even higher. Theory and simulations of peak shifts due to space charge interactions in TOF will be presented in the report.

Literature

[1] Josh Barnes and Piet Hut, A hierarchical $O(N \log N)$ force-calculation algorithm, Nature vol.324, 4 December 1986, pp.446-449

[2] L. Greengard, V. Rokhlin, J. Comput. Phys. 73 (1987) 325.; L. Greengard, Science 265 (1994) 909

RESULTS FROM A NEW HIGH SPATIAL RESOLUTION SAM/SEM ELECTROSTATIC COLUMN

A.R. Walker and M. Rignall

Shimadzu Research Laboratory (Europe) LTD.
Wharfside, Trafford Wharf Road, Manchester M17 1GP. UK.
e-mail: Andrewr.walker@srl.co.uk

We have developed a high spatial resolution all electrostatic ultra high vacuum column with Schottky source for Auger electron spectroscopy (AES) and other analytical applications, shown in Fig.1. The specified beam energy range of the column is from 5 to 10keV and operates with an accelerating conical objective lens with a nominal working distance of 10mm. The electron optical column was designed to operate mainly in a scanning Auger microscope (SAM) or a scanning electro microscope (SEM) mode but other modes of operation are available. These other modes include a high spatial resolution (<10nm) objective lens only mode, a low spatial resolution (<1 μ m) survey mode and an intermediate spatial resolution (<100nm) high current mode.

High voltage (50kV) long term operation of the objective lens is totally reliable from UHV ($\leq 3 \times 10^{-10}$ Torr) to HV ($\leq 10^{-6}$ Torr) with no micro discharges detected in the image recordings. In general voltage conditioning (up to 70kV) of the lens is only necessary if any of its components are changed. The electron optical design of the conical Einzel objective lens is asymmetrical and operates with a positive potential on the inner electrode. Lens aberrations were calculated for the object at infinity and a 10mm working distance, using software provided by Lencova [1] and the CPO2D program [2]. Low values of spherical aberration (75mm) and chromatic aberration (19mm) were obtained, which are comparable with a magnetic lens of similar external dimensions and working distance.

The column is electrically a high impedance device and unwanted perturbations of an electric origin superimposed on the image detail have been hard to eliminate. To simplify the operation of the column we use the objective lens only mode as a diagnostic means. With progress we have achieved less than 5nm spatial resolution in an Objective lens only mode at beam energies of 7keV, as shown in Fig. 2. For the given probe defining aperture, this result equates closely to a theoretical value derived from using the calculated lens aberrations (probe containing 50% of the current [3]).

The field of view of the survey mode is limited by the 2mm diameter exit aperture of the objective lens and has a maximum in excess of 5mm diameter. In a high current mode, probe currents in excess of 200nA are available with spatial resolutions better than 100nm.

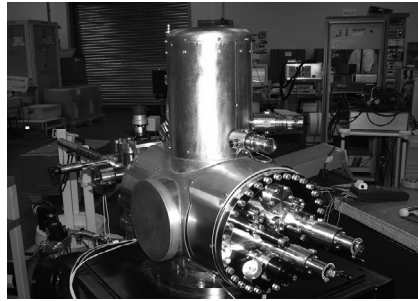
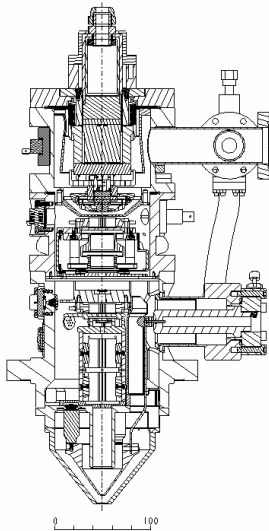


Figure 1 A schematic drawing of the all electrostatic column and the fabricated system in a Mu-metal sheath shown mounted on an evaluation specimen chamber.

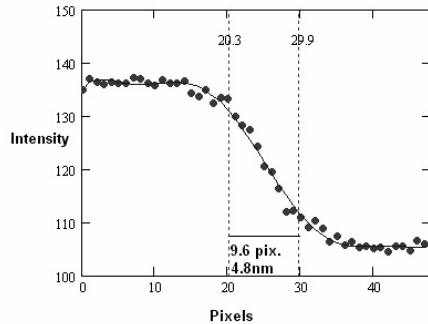
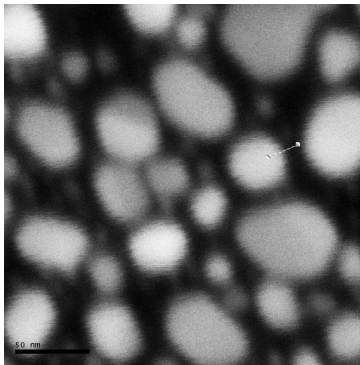


Figure 2. Objective lens only mode with a beam energy of 7keV. The specimen is gold islands on carbon and the image field of view of the raw image shown is 240nm. The line profile is a fit to the measured edge data from the image (defined by the white line scan). The remaining 50Hz image perturbation is magnetic in origin.

[1] B. Lencova, Nucl. Instr. Meth. In Phys. Res. A363(1995), 190-197.

[2] CPO Programs, available on the Web site <http://www.electronoptics.com/>

[3] J.E. Barth, P. Kruit, Optik 101 (1996), 101-109

PEEM WITH TWO COMPLEMENTARY ELECTRON ENERGY FILTERS: TOF AND RETARDING FIELD ANALYSER

N.B. Weber^{1*}, M. Escher¹, M. Merkel¹, J. Lin², U. Kleineberg²

¹FOCUS-GmbH, Neukirchner Str. 2, 65510 Hünstetten-Kesselbach, Germany

²Faculty of Physics, Ludwig Maximilian University, 85748 München, Germany

*n.weber@focus-gmbh.com

The strength of conventional PEEM is the flexibility in the photon source. In the classical approach the work with threshold emission reveals mostly work function contrast. With tuneable soft x-rays (so called XPEEM) one can gain element specific information by absorption spectroscopy. Even light sources with photon energies below the work function are in use, exploiting a two photon photoemission (2PPE) process. In order to gain more quantitative information about the sample, electron energy filtering became popular in the past. There are different approaches, namely band pass filters [1-3], high pass filters [4,5] and time of flight spectroscopy [5,6]. Each of the filter type covers a different range of application.

We combined a high pass filter, also called Imaging Energy Filter (IEF), and a time of flight (ToF) detector in one PEEM, that enables one to gather electron energy filtered information of the same sample with different filter methods (see Fig. 1). Both the high pass filter and the ToF detection are integrated in a straight column and are easy to handle. The design is kept strictly electrostatic. Both filters show an energy resolution better than 100meV. In most cases this is sufficient.

The high pass filter is realised as a retarding field analyser. In order to improve the energy resolution, the mesh size of the retarding grids in use is kept very small and the electrical retardation field is chosen as small as possible in order to reduce the field penetration through the mesh. It can be operated with continuous and pulsed light sources. We have gathered results in threshold emission (mercury arc lamp), where the work function can be determined. Excitation with a helium discharge lamp enables imaging UPS or locally ARUPS by imaging the back focal plane of the objective lens

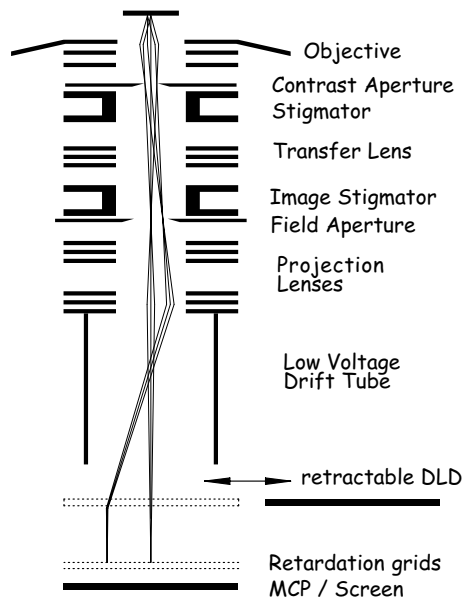


Fig. 1: Sketch of the TOF-IEF-PEEM: Retractable delay line detector combined with an in line Imaging Energy Filter (Retarding Field Analyser).

(k-space imaging, see Fig. 2). The data acquisition is analogue and is realized with an imaging unit and a CCD-camera. So there is no limit to high intensities, since this can be adopted with the gain of the imaging unit. Therefore it is an excellent system for high count rates.

The ToF detection is realized with the drift tube operated at a low column voltage and a delay line detector (DLD). The low column voltage enables a conversion of the energy dispersion into a time dispersion of the electrons. The DLD can detect the time of arrival, and the lateral position of the electron.

Here we show results with a 400nm, 60ps pulsed diode laser. The spectrum of the molybdenum surface shows a Fermi edge with 96meV width (16%-84%), that reveals a detector resolution better than 50meV (see Fig. 3). The strength of the ToF detection is, that each incoming electron is counted. So the advantage in

acquisition time over a band pass is simply the number of data points in the spectrum. The DLD is a counting system and therefore it is limited in the count rate by the dead time of the system. Therefore it is an excellent system for low count rates.

The combination of the two energy filters allow for applications with a wide range of light sources. This makes the use of the instrument more versatile.

References

- [1] M. Escher et al., J. Phys.: Condens. Matter **17** (2005) 1329–1338
- [2] Th. Schmidt et al., Surface Review and Letters, Vol. 9, No. 1 (2002) 223-232
- [3] E. Bauer et al., J. Electron Spectrosc. Relat. Phenom. **84** (1997). 201
- [4] Merkel M et al. Surf. Sci. **480** (2001) 196
- [5] N.B. Weber et al., Journal of Physics: Conference Series **100** (2008) 072031
- [6] Oelsner et al., Rev. Sci. Instrum., **72** (2001) 3968

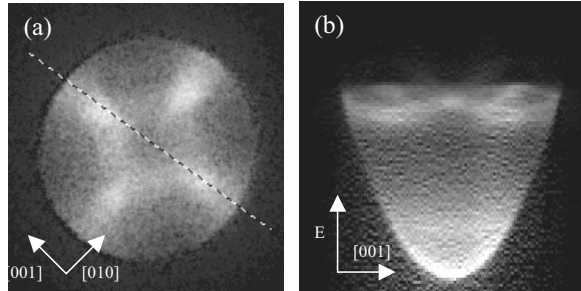


Fig. 2: k_{\parallel} -Measurements on an Ag(100) surface. a) k_{\parallel} -plot at 10.9eV retardation voltage. b) Cut through the k -E plane showing the band-structure and the energy dispersion E - k^2 .

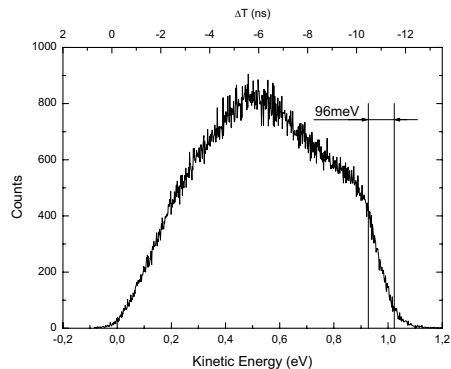


Fig. 3: Spectra of a Mo(110) surface exited with a 400nm pulsed diode laser.

ELECTRON BEAM WELDING IN ISI BRNO: PAST&PRESENT

M. Zobač, I. Vlček

Institute of Scientific Instruments ASCR, v.v.i., Královopolská 147, Brno, 612 64, Czech Republic, zobac@isibrno.cz

The Institute of Scientific Instruments (ISI) was founded in 1957. From the very beginning, analytical electron-beam devices, particularly electron microscopes were designed and produced here. Later technological applications of the e-beam have been developed too. First instrument was a multifunctional vacuum furnace made in 1965 (see Fig. 1, [1]) with a round working chamber evacuated by a rotary and a diffusion pump (designed also in ISI). The furnace had three different heat-sources: an infra-red heating (molybdenum direct-heated basket), a HF induction heating and a low power e-beam gun (50 kV/5 mA). Possible applications were vacuum soldering/brazing, vacuum reflow and e-beam welding.

The last option led to development of the first specialized e-beam welder in ISI (see Fig. 2), that has been later produced in cooperation with other companies (e.g. former Tesla Opočno – see. Fig. 3) in years 1969-70. Beam power was up to 1.5 kW, beam energy was 50 keV. The electronics, developed mainly in ISI, had progressive features including e-beam viewing system (scanning-electron-microscope mode) and oscillating beam mode. This welder was used for variety of tasks, including welding of vacuum components: pipes, valves, membrane bellows, feed-throughs etc., cryogenic devices like helium cryostat components and many others.

In 1990s the welder was redesigned, especially its e-gun [2], electronics, manipulator and vacuum system. The modified welder with medium-size chamber works in ISI so far.



Fig. 2: E-beam welder ES-2 installed in ISI, Brno

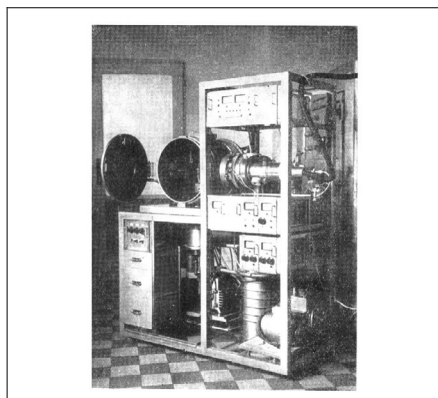


Fig. 1: Multifunctional vacuum furnace [1]

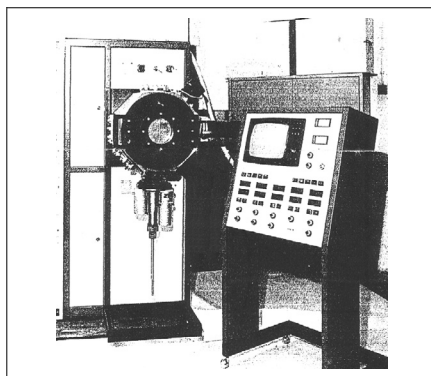


Fig. 3: E-beam welder ES-2 clone made in Tesla Opočno

A desktop electron beam welder SES-1 shares the same e-gun and electronics (see Fig. 4). This instrument, which has small chamber volume about 7 litres, is intended for piece production especially for instrumentation and vacuum technologies.

The recent e-beam welder MEBW-60/2 (see Fig. 5, [3]) is SES-1 descendant. The e-gun, working chamber, stage and workbench were considerably improved and allow reliable operation up to 60 kV/2 kW. New electronics, including high voltage power supply, is completely digitized now. Remote control by common personal computer is possible (see. Fig. 6). The control software allows image acquisition, arbitrary shaped welding (“Draw-a-weld” mode), micro-engraving techniques and other functions.

The MEBW is now produced by Focus GmbH Company under licence [4], with custom working chambers and manipulators.



Fig. 4: E-beam welder SES-1 installed in ISI together with its designer, Dipl. Eng. Jan Dupák



Fig. 5: Recent e-beam welder MEBW-60/2

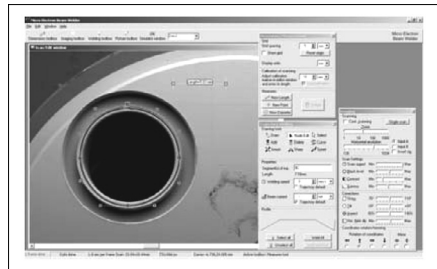


Fig. 6: MEBW-60/2 PC control software screenshot

REFERENCES

- [1] Zobač, L. et al.: Multi-functional vacuum furnace with HF, IR and electron-beam heating (Czech); *Slaboproudý obzor*, **28** (1967), **3**, 146
- [2] Dupák, J. et al.: Electron gun for computer controlled welding of small components; *Vacuum* **62** (2001), 159-164
- [3] Vlček, I. et al.: Desktop electron beam welder MEBW-60/2 (Czech); *JMO*, **53** (2008), 27-30
- [4] Focus GmbH: Micro Electron Beam Welder MEBW-60/2 (web pages-German), <http://www.focus-e-welding.de>

